

# Integrated Modeling of Offshore Wind Turbines

Spyridoula Nata



# Integrated Modeling of Offshore Wind Turbines

## Offshore and Dredging Engineering

Spyridoula Nata

16<sup>th</sup> of January 2018

Student number: 4522443  
Project duration: April, 2017 – January, 2018  
Thesis committee: Prof. Dr. A.V. Metrikine, TU Delft, Chairman of the Graduation Committee  
Ir. P. van der Male, TU Delft, Daily supervisor  
Dr. Ir. H. Hendrikse, TU Delft, Daily supervisor  
Dr. Ir. K.N. van Dalen, TU Delft, Committee member

An electronic version of this thesis is available at <http://repository.tudelft.nl/>.



# Abstract

In order for the offshore wind industry to be competitive, the cost has to be driven down. One of the major factors that contribute to the overall cost is the over-dimensioning of the substructure. The response of the structure under various loading conditions can provide valuable insight in the design phase so as to provide a structural design that is cost effective yet reliable, and can withstand the loads that are considered to act on the structure.

The objective of the present thesis is the development of a 1D finite element model, that allows for a dynamic analysis of an offshore wind turbine under the combined actions of wind and wave or wind and ice. For this purpose, different models have been combined and improved or extended. Through this model the importance of accounting for non-linear and breaking waves, the effect of the kinematic stretching on the response and the manner in which the misalignment of the load affects the response can be investigated.

A detailed design of the NREL-5MW offshore wind turbine supported by a monopile is subjected to wind, wave and ice action. The aerodynamic action is evaluated through a model valid for the above rated regime when pitch control is active, using a turbulent wind signal resulting from the Kaimal spectrum. The hydrodynamic action is calculated either with the Morison equation or the MacCamy and Fuchs equation with the use of either linear or non-linear water particle kinematics. An approach towards the calculation of the load from a breaking wave is considered accounting for the wave skewness and asymmetry during such an event. The ice action is calculated through a model that evaluates the force while in the crushing regime. The soil is represented with linear soil springs.

The structure's response is investigated for all the loads separately at first. The next step is the combined analysis. Aligned and misaligned cases are considered. Results show that wind load is dominating the response in the aligned and misaligned wind and wave case regardless of the method used to calculate the hydrodynamic load in the case of a small wave height. In the case of a larger wave height, using Stokes theory and the Morison equation, the hydrodynamic load is contributing to the resulting response. Concerning the ice loading, the intermittent crushing and the continuous brittle crushing regimes occur for the turbine. The response to the combined wind and ice action appears to be affected by both loads in all examined cases.



# Acknowledgements

First of all, I would like to express my appreciation to Professor Metrikine for his guidance along the way. Next, I would like to thank Pim van der Male, for his patience and understanding during this project as well as the many interesting conversations during our meetings. Additionally, I would like to thank Hayo Hendrikse for his guidance and insightful comments on the challenging subject of ice-induced vibrations and the patience he showed to my silly questions. Furthermore, I would like to thank my friends and family for their continuous support during the course of my studies at TU Delft and especially during the last year.



# Contents

<b>List of Figures</b>	<b>ix</b>
<b>List of Tables</b>	<b>xiii</b>
<b>1 Introduction</b>	<b>1</b>
1.1 Integrated modeling of offshore wind turbines . . . . .	1
1.2 Thesis outline . . . . .	2
<b>2 The reference wind turbine</b>	<b>3</b>
2.1 Turbine properties . . . . .	3
2.2 Rotor nacelle assembly properties . . . . .	3
2.3 Tower and monopile properties . . . . .	4
<b>3 Structural model</b>	<b>7</b>
3.1 Introduction . . . . .	7
3.2 Mass matrix . . . . .	7
3.3 Stiffness matrix . . . . .	8
3.4 Damping matrix . . . . .	8
<b>4 Hydrodynamic loading</b>	<b>11</b>
4.1 Introduction . . . . .	11
4.2 Water particle kinematics . . . . .	12
4.2.1 Airy wave theory for small wave heights . . . . .	12
4.2.2 Stokes finite amplitude wave theory for larger wave heights . . . . .	14
4.2.3 Non-linear orbital velocity for breaking waves . . . . .	15
4.3 Kinematic stretching . . . . .	17
4.4 Hydrodynamic force . . . . .	17
4.4.1 Morison equation . . . . .	18
4.4.2 Diffraction theory . . . . .	19
4.4.3 Breaking wave theory . . . . .	20
<b>5 Soil structure interaction</b>	<b>23</b>
5.1 Introduction . . . . .	23
5.2 P-Y curves . . . . .	23
5.3 Translation of 3D modeling to simplified springs . . . . .	24
<b>6 Ice structure interaction</b>	<b>27</b>
6.1 Introduction . . . . .	27
6.2 Intermittent crushing . . . . .	28
6.3 Frequency lock-in . . . . .	28
6.4 Continuous brittle crushing . . . . .	28
6.5 Formulation of ice elements and ice load around the monopile . . . . .	29
<b>7 Aerodynamic loading</b>	<b>31</b>
7.1 Introduction . . . . .	31
7.2 Rotor model . . . . .	31
7.3 Aerodynamic load on the blades . . . . .	32
7.4 Aerodynamic load on the tower . . . . .	32

---

<b>8</b>	<b>Results</b>	<b>35</b>
8.1	Modal analysis . . . . .	35
8.2	Aerodynamic load . . . . .	36
8.3	Hydrodynamic load . . . . .	39
8.4	Ice load . . . . .	44
8.5	Aerodynamic and hydrodynamic load . . . . .	47
8.5.1	Aligned . . . . .	47
8.5.2	Misaligned . . . . .	50
8.6	Aerodynamic and ice load . . . . .	54
8.6.1	Aligned . . . . .	54
8.6.2	Misaligned . . . . .	57
<b>9</b>	<b>Conclusion and recommendations</b>	<b>61</b>
9.1	Concluding remarks . . . . .	61
9.2	Recommendations for further work . . . . .	62
<b>A</b>	<b>Appendix A: Modeling</b>	<b>63</b>
A.1	Parameters . . . . .	63
A.2	Discretization . . . . .	63
A.3	Varying surface elevation . . . . .	64
A.4	Modal damping ratios . . . . .	65
	<b>Bibliography</b>	<b>67</b>

# List of Figures

2.1	Foundation types installed in 2016 (in units) [10]. . . . .	5
3.1	Deformation of a Timoshenko beam element [11]. . . . .	7
4.1	Water wave theories [15]. . . . .	11
4.2	PM spectrum for $H_S=0.5$ , $T_p=15.96m$ , $d=25m$ and 50 harmonic components. . .	13
4.3	PM spectrum for $H_S=0.5$ , $T_p=15.96s$ , $d=25m$ and 200 harmonic components. . .	13
4.4	Surface elevation for $H_S=0.5$ , $T_p=15.96s$ and $d=25m$ . . . . .	13
4.5	Surface elevation for $H_S=0.5$ , $T_p=15.96m$ , $d=25m$ using the PM spectrum and 200 harmonic components. . . . .	14
4.6	Surface elevation for $H_S=2.5m$ , $T_p=22.58s$ and $d=25m$ . . . . .	14
4.7	Velocity profile for $H_S=2.5m$ , $T_p=22.58s$ and $d=25m$ . . . . .	15
4.8	Velocity profile for a breaking wave with $H=20m$ , $T=32s$ and $d=25m$ , for 21 different sets of parameters . . . . .	16
4.9	Velocity profile for a breaking wave with $H=20m$ , $T=32s$ and $d=25m$ . . . . .	16
4.10	Stretching of the surface profile [19]. . . . .	17
4.11	Regions of applicability [20]. . . . .	18
4.12	Keulegan-Carpenter's drag coefficient as functions of $K_C$ for 12 values of $\beta = \frac{Re}{K_C}$ [31]. . . . .	19
4.13	Keulegan-Carpenter's inertia coefficient as functions of $K_C$ for 12 values of $\beta = \frac{Re}{K_C}$ [31]. . . . .	19
5.1	Simplified offshore wind turbine model with translational and rotational spring supports [44]. . . . .	25
6.1	Factors influencing interaction scenarios [45]. . . . .	27
6.2	Ice action (top) and structural response (bottom) for (a) intermittent crushing (b) frequency lock-in and (c) continuous brittle crushing [45]. . . . .	28
6.3	Illustration of the contact zones around the monopile [47]. . . . .	29
6.4	Ice element [47]. . . . .	29
7.1	Definition of the rigid rotor model indicating the azimuths $\Psi_1$ , $\Psi_2$ , $\Psi_3$ , of the blades and the rotational velocity $\Omega$ [48]. . . . .	31
8.1	From left to right the first, second and third mode in the XZ plane (Side-Side motion). . . . .	35
8.2	From left to right the first, second and third mode in the YZ plane (Fore-Aft motion). . . . .	36
8.3	Turbulent wind signal at the hub height. . . . .	36
8.4	Displacement of the RNA in the YZ plane (Fore-Aft motion). . . . .	37
8.5	Displacement of the RNA in the XZ plane (Side-Side motion), resulting from the aerodynamic load on the blades. . . . .	37
8.6	Displacement of the RNA in the YZ plane (Fore-Aft motion), resulting from both the aerodynamic load on the blades and the drag force on the exposed elements. . . . .	38
8.7	Displacement of the RNA in the XZ plane (Side-Side motion), resulting from both the aerodynamic load on the blades and the drag force on the exposed elements. . . . .	38
8.8	Single sided amplitude spectrum of the response of Figure 8.6. . . . .	38
8.9	Single sided amplitude spectrum of the response of Figure 8.7. . . . .	39

8.10 Displacement of the RNA in the YZ plane (Fore-Aft motion), resulting from the Airy wave theory and the Morison equation, for a wave height of $H_S=0.5m$ and $T_p=15.96s$ . . . . .	39
8.11 Single sided amplitude spectrum of the response for the same conditions as in Figure 8.10. . . . .	40
8.12 Displacement of the RNA in the YZ plane (Fore-Aft motion), resulting from the diffraction theory and the MacCamy and Fuchs equation, for a wave height of $H_S=0.5m$ and $T_p=15.96s$ . . . . .	40
8.13 Single sided amplitude spectrum of the response for the same conditions as in Figure 8.12. . . . .	40
8.14 Displacement of the RNA in the YZ plane (Fore-Aft motion), resulting from the Stokes theory and the Morison equation, for a wave height of $H_S=2.5m$ and $T_p=22.58s$ . . . . .	41
8.15 Single sided amplitude spectrum of the response for the same conditions as in Figure 8.14. . . . .	41
8.16 Displacement of the RNA in the YZ plane (Fore-Aft motion), resulting from the diffraction theory and the MacCamy and Fuchs equation, for a wave height of $H_S=2.5m$ and $T_p=22.58s$ . . . . .	42
8.17 Single sided amplitude spectrum of the response for the same conditions as in Figure 8.16. . . . .	42
8.18 Displacement of the RNA in the YZ plane (Fore-Aft motion), resulting from the Stokes vs the Airy theory and the Morison equation, for a wave height of $H_S=2.5m$ and $T_p=22.58s$ . . . . .	42
8.19 Displacement of the RNA in the YZ plane (Fore-Aft motion), resulting from the Airy theory and the Morison equation, for a wave height of $H_S=2.5m$ and $T_p=22.58s$ . . . . .	43
8.20 Displacement of the RNA in the YZ plane (Fore-Aft motion), for a wave height of $H_S=20m$ and $T_p=32s$ . . . . .	43
8.21 Single sided amplitude spectrum of the response for the same conditions as in Figure 8.20. . . . .	44
8.22 Displacement of the RNA in the XZ plane (Side-Side motion), for the cases with an incoming angle of $0^\circ$ . . . . .	44
8.23 Displacement at the ice action point in the YZ plane (Fore-Aft motion), for an indentation velocity of $v_{ice}=0.005m/s$ and thickness $h_{ice}=0.4m$ . . . . .	45
8.24 Displacement at the ice action point in the XZ plane (Side-Side motion), for an indentation velocity of $v_{ice}=0.005m/s$ and thickness $h_{ice}=0.4m$ . . . . .	45
8.25 Single sided amplitude spectrum of the response for the same conditions as in Figure 8.23. . . . .	45
8.26 Single sided amplitude spectrum of the response for the same conditions as in Figure 8.24. . . . .	46
8.27 Displacement at the ice action point in the YZ plane (Fore-Aft motion), for an indentation velocity of $v_{ice}=0.15m/s$ and thickness $h_{ice}=0.4m$ . . . . .	46
8.28 Displacement at the ice action point in the XZ plane (Side-Side motion), for an indentation velocity of $v_{ice}=0.15m/s$ and thickness $h_{ice}=0.4m$ . . . . .	46
8.29 Single sided amplitude spectrum of the response for the same conditions as in Figure 8.28. . . . .	47
8.30 Single sided amplitude spectrum of the response for the same conditions as in Figure 8.28. . . . .	47
8.31 Displacement of the RNA in the YZ plane (Fore-Aft motion), resulting from the Airy theory and the Morison equation, for a wave height of $H_S=0.5m$ and $T_p=15.96s$ . . . . .	48
8.32 Displacement of the RNA in the XZ plane (Side-Side motion), resulting from the Airy theory and the Morison equation, for a wave height of $H_S=0.5m$ and $T_p=15.96s$ . . . . .	48
8.33 Displacement of the RNA in the YZ plane (Fore-Aft motion), resulting from the diffraction theory and the MacCamy and Fuchs equation, for a wave height of $H_S=0.5m$ and $T_p=15.96s$ . . . . .	48

8.34 Displacement of the RNA in the XZ plane (Side-Side motion), resulting from the diffraction theory and the MacCamy and Fuchs equation, for a wave height of $H_S=0.5m$ and $T_p=15.96s$ . . . . .	49
8.35 Displacement of the RNA in the YZ plane (Fore-Aft motion), resulting from the Airy theory and the Morison equation, for a wave height of $H_S=2.5m$ and $T_p=22.58s$ . . . . .	49
8.36 Displacement of the RNA in the XZ plane (Side-Side motion), resulting from the Airy theory and the Morison equation, for a wave height of $H_S=2.5m$ and $T_p=22.58s$ . . . . .	49
8.37 Displacement of the RNA in the YZ plane (Fore-Aft motion), resulting from the diffraction theory and the MacCamy and Fuchs equation, for a wave height of $H_S=2.5m$ and $T_p=22.58s$ . . . . .	50
8.38 Displacement of the RNA in the XZ plane (Side-Side motion), resulting from the diffraction theory and the MacCamy and Fuchs equation, for a wave height of $H_S=2.5m$ and $T_p=22.58s$ . . . . .	50
8.39 Displacement of the RNA in the YZ plane (Fore-Aft motion), resulting from the Airy theory and the Morison equation, for a wave height of $H_S=0.5m$ and $T_p=15.96s$ and a $30^\circ$ angle of attack. . . . .	51
8.40 Displacement of the RNA in the XZ plane (Side-Side motion), resulting from the Airy theory and the Morison equation, for a wave height of $H_S=0.5m$ and $T_p=15.96s$ and a $30^\circ$ angle of attack. . . . .	51
8.41 Displacement of the RNA in the YZ plane (Fore-Aft motion), resulting from the diffraction theory and the MacCamy and Fuchs equation, for a wave height of $H_S=0.5m$ and $T_p=15.96s$ and a $30^\circ$ angle of attack. . . . .	51
8.42 Displacement of the RNA in the XZ plane (Side-Side motion), resulting from the diffraction theory and the MacCamy and Fuchs equation, for a wave height of $H_S=0.5m$ and $T_p=15.96s$ and a $30^\circ$ angle of attack. . . . .	52
8.43 Displacement of the RNA in the YZ plane (Fore-Aft motion), resulting from the Stokes theory and the Morison equation, for a wave height of $H_S=2.5m$ and $T_p=22.58s$ and a $30^\circ$ angle of attack. . . . .	52
8.44 Displacement of the RNA in the XZ plane (Side-Side motion), resulting from the Stokes theory and the Morison equation, for a wave height of $H_S=2.5m$ and $T_p=22.58s$ and a $30^\circ$ angle of attack. . . . .	53
8.45 Single sided amplitude spectrum of the response of Figure 8.43. . . . .	53
8.46 Single sided amplitude spectrum of the response of Figure 8.44. . . . .	53
8.47 Displacement of the RNA in the YZ plane (Fore-Aft motion), resulting from the diffraction theory and the MacCamy and Fuchs equation, for a wave height of $H_S=2.5m$ and $T_p=22.58s$ and a $30^\circ$ angle of attack. . . . .	54
8.48 Displacement of the RNA in the XZ plane (Side-Side motion), resulting from the diffraction theory and the MacCamy and Fuchs equation, for a wave height of $H_S=2.5m$ and $T_p=22.58s$ and a $30^\circ$ angle of attack. . . . .	54
8.49 Displacement at the ice action point in the YZ plane (Fore-Aft motion), for an indentation velocity of $v_{ice}=0.005m/s$ . . . . .	55
8.50 Displacement at the ice action point in the XZ plane (Side-Side motion), for an indentation velocity of $v_{ice}=0.005m/s$ . . . . .	55
8.51 Single sided amplitude spectrum of the response of Figure 8.57. . . . .	55
8.52 Single sided amplitude spectrum of the response of Figure 8.58. . . . .	56
8.53 Displacement at the ice action point in the YZ plane (Fore-Aft motion), for an indentation velocity of $v_{ice}=0.15m/s$ . . . . .	56
8.54 Displacement at the ice action point in the XZ plane (Side-Side motion), for an indentation velocity of $v_{ice}=0.15m/s$ . . . . .	56
8.55 Single sided amplitude spectrum of the response of Figure 8.53. . . . .	57
8.56 Single sided amplitude spectrum of the response of Figure 8.54. . . . .	57
8.57 Displacement at the ice action point in the YZ plane (Fore-Aft motion), for an indentation velocity of $v_{ice}=0.005m/s$ . . . . .	58
8.58 Displacement at the ice action point in the XZ plane (Side-Side motion), for an indentation velocity of $v_{ice}=0.005m/s$ . . . . .	58
8.59 Single sided amplitude spectrum of the response of Figure 8.57. . . . .	58

---

8.60	Single sided amplitude spectrum of the response of Figure 8.58. . . . .	59
8.61	Displacement at the ice action point in the YZ plane (Fore-Aft motion), for an indentation velocity of $v_{ice}=0.15m/s$ . . . . .	59
8.62	Displacement at the ice action point in the XZ plane (Side-Side motion), for an indentation velocity of $v_{ice}=0.15m/s$ . . . . .	59
8.63	Single sided amplitude spectrum of the response of Figure 8.61. . . . .	60
8.64	Single sided amplitude spectrum of the response of Figure 8.62. . . . .	60
A.1	Effect of discretization in the response of the RNA in the YZ plane. . . . .	64

# List of Tables

2.1	Properties for the upwind 3-bladed NREL 5-MW wind turbine [8]. . . . .	3
2.2	Undistributed blade structural properties [8]. . . . .	4
2.3	Nacelle and hub properties [8]. . . . .	4
2.4	Tower properties [8], [9]. . . . .	4
2.5	Transition piece and monopile properties [8], [9]. . . . .	5
5.1	Sand parameters [44]. . . . .	24
5.2	Calibrated springs for the NREL 5MW offshore wind turbine [44]. . . . .	24
7.1	Indicative coefficients for cylindrical members according to API and SNAME. . . . .	33
8.1	The first thirty natural frequencies of the structure in <i>Hz</i> . . . . .	36
A.1	Steel properties used for the finite element model. . . . .	63
A.2	Explanation of the examined discretization options. . . . .	64
A.3	Convergence of the response of the RNA based on the discretization. . . . .	64
A.4	Modal damping ratios for the lowest modes with $\alpha_0=0.0048$ and $\alpha_1=0.0841$ . . . . .	65
A.5	Modal damping ratios for the lowest modes with $\alpha_0=0.0012$ and $\alpha_1=0.0207$ . . . . .	65



# Nomenclature

$\alpha$	Wave amplitude
$\alpha_0$	Mass proportional Rayleigh damping coefficient
$\alpha_1$	Stiffness proportional Rayleigh damping coefficient
$\alpha_{air}$	Exponent used in power law
$\alpha_{diff}$	Phase lag for diffraction theory
$\beta_i$	Global reference angle
$\Phi$	Shear slenderness
$\Phi_W$	Velocity potential
$\epsilon$	Small ordering parameter
$\eta$	Surface profile
$\eta_b$	Maximum elevation of the free water surface
$\gamma$	Peak enhancement factor
$\gamma_{max}$	Domain size
$\gamma_{Smax}$	Domain size
$\kappa$	Shear coefficient
$\lambda$	Wave length
$\lambda_0$	Wave length in deep waters
$\lambda_c$	Curling factor
$\nu$	Poisson ratio
$\omega$	Wave frequency
$\omega_i$	Natural frequency of the $i^{th}$ mode
$\omega_n$	Natural frequency
$\phi$	Wave phase
$\phi'$	Sand internal angle of friction
$\phi_{PT}$	Sand phase transformation angle
$\psi$	Phase
$\rho$	Density
$\rho_W$	Density of water
$\rho_{air}$	Density of air
$\theta$	Asymmetry parameter

---

$\xi$	Damping ratio
$\xi_i$	Damping ratio of the $i^{th}$ mode
$A$	Cross sectional area
$a_x$	Horizontal water particle acceleration
$A_{diff}$	Function of the pile diameter over length ratio for diffraction theory
$A_{PM}$	Pierson-Moskowitz spectrum constant
$B$	Non-linearity parameter
$B_{PM}$	Pierson-Moskowitz spectrum constant
$C$	Damping matrix
$C$	Wave celerity
$c_1$	Sand contraction parameter
$c_2$	Sand contraction parameter
$c_3$	Sand contraction parameter
$C_\alpha$	Added mass coefficient
$C_c$	Critical damping
$C_D$	Drag coefficient
$C_M$	Inertia coefficient
$C_R$	Rotor damping matrix
$C_{S,D}$	Viscous damping attributed to soil
$d$	Distance of the center of rotation of the rotor from the origin of the reference frame
$d$	Water depth
$d_1$	Sand dilation parameter
$d_2$	Sand dilation parameter
$d_3$	Sand dilation parameter
$E$	Elastic modulus
$F$	Horizontal hydrodynamic force
$F_{D_{wind}}$	Wind drag force
$F_{mean}$	Generated mean lift force for the static deflection
$F_{x,i}$	Ice force in x direction in the $i^{th}$ zone
$F_{y,i}$	Ice force in y direction in the $i^{th}$ zone
$G$	Shear modulus
$g$	Gravity acceleration
$G_r$	Sand shear modulus
$H$	Wave height

---

$h$	Water depth
$H_0$	Wave height in deep waters
$H_B$	Breaking wave height
$H_S$	Significant wave height
$J_1$	Bessel function of first kind
$K$	Stiffness matrix
$k$	Wave number
$K_2$	Ice stiffness
$K_b$	Bending stiffness matrix of element
$K_C$	Keulegan-Carpenter number
$K_g$	Geometric matrix of element
$K_R$	Rotor stiffness matrix
$K_{S,L}$	Translational stiffness attributed to soil
$K_{S,R}$	Rotational stiffness attributed to soil
$L$	Wave length
$l$	Length of element
$M$	Mass matrix
$m$	Mass
$m_j$	Mass of blade $j$
$M_R$	Rotor mass matrix
$M_r$	Rotational mass matrix of element
$M_t$	Translational mass matrix of element
$P$	Compressive axial load
$p_1$	Non-linear orbital velocity parameter
$p_2$	Non-linear orbital velocity parameter
$p_3$	Non-linear orbital velocity parameter
$p_4$	Non-linear orbital velocity parameter
$p_5$	Non-linear orbital velocity parameter
$p_6$	Non-linear orbital velocity parameter
$p'_r$	Confinement pressure
$p'_y$	Confinement
$Q_x$	Horizontal momentum averaged over time per unit surface area
$q_x$	Horizontal momentum
$R$	Ending point of integration along the blade

---

$r$	Skewness parameter
$r_0$	Starting point of integration along the blade
$r_g$	Radius of gyration
$r_j$	Blade axes
$r_{in}$	Inner radius of element
$r_{out}$	Outer radius of element
$Re$	Reynolds number
$S_{PM}$	Wave spectral density
$T$	Period
$t$	Time instance
$T_P$	Peak spectral period
$U$	Ursell number
$u_m$	Amplitude of the horizontal water particle velocity
$u_S$	Structure's displacement in y direction
$U_W$	Horizontal water particle velocity from linear theory
$u_x$	Horizontal water particle velocity
$u_{i,1}$	Ice element displacement in y direction
$u_{static}$	Static deflection of the structure
$u_{wind}$	Velocity of air
$v_S$	Structure's displacement in x direction
$v_{i,1}$	Ice element displacement in x direction
$v_{ice}$	Ice velocity
$w_{zone}$	Zone width
$x$	Coordinate in x-direction (horizontal)
$Y_1$	Bessel function of second kind
$z$	Coordinate in z-direction (vertical)
$z_{ref}$	Reference height for power law

# Introduction

Currently each of the forces acting on an offshore wind turbine can be addressed separately with the models that have been developed by the Offshore and Dredging Engineering section of TU Delft. The response to each environmental load can be evaluated separately and then by means of superposition the response to the combined loads can be calculated. This can lead to an underestimation of the loads that are actually exerted on the structure. This underestimation can prove to be very important, especially in the case of fatigue analysis, when the accumulated damage will be under-predicted in every step leading to serious miscalculations over the lifetime of the project. For this reason there is a need for a model that integrates the actions and allows a combined analysis. This combined analysis will allow for the investigation of cases such as the misalignment of wind and wave action, as well as wind and ice action.

The thesis aims to create a user friendly, modular, numerical model that can be used to monitor the response of the structure under various loading cases. In order to produce realistic results all of the loading components are represented accurately, but making the necessary assumptions. The hydrodynamics model considers three main areas of application based on the wave height. Linear theory, Stokes second order theory, and an approach to describe a breaking wave are used along with kinematic stretching to evaluate the hydrodynamic force using the Morison or MacCamy and Fuchs equations. A simplified aero-servo elastic model is employed to evaluate the aerodynamic load. Furthermore, a phenomenological model is used to predict the ice-induced vibrations. Every component is combined into a finite element model in MATLAB, using Timoshenko beam elements to describe the structure.

## 1.1. Integrated modeling of offshore wind turbines

The energy industry has been conducting a lot of research into the offshore wind sector, as the vast resource of the offshore wind climate makes it an attractive form of renewable energy. Currently a lot of integrated models used to analyze offshore wind turbines exist. Universities, research institutions, and the industry have been working towards the creation of models capable of predicting the coupled dynamic loads and response of the system. ADAMS2AD was developed by NREL and MSC Software and links the aerodynamics module AeroDyn to MSC.ADAMS dynamics software, the hydrodynamic loading is evaluated with the Morison equation using linear theory or a user defined routine [1]. ADCoS-Offshore, developed by ADC and IWES, evaluates the hydrodynamic load as ADAMS2AD and allows for different types of foundation types [1]. BLADED is a simulation software from DNV-GL, hydrodynamic calculations are done using Airy theory or stream function and the Morison equation along with a MacCamy and Fuchs correction. Additionally, it allows to import advanced hydrodynamics from other software packages such as WAMIT or AQWA, contains a seismic module and allows for various foundation types as well [2]. FAST, developed by NREL

couples aerodynamic, hydrodynamic, control and electrical system and structural dynamics to perform time domain simulations of a turbine [3]. SIMPACK has interfaces that can link the Rotorblade Generator, which simulates flexible rotor blades, with the AeroDyn and HydroDyn (only linear hydrodynamics and Morison equation) from NREL [4]. HAWC2, developed by DTU, allows for various foundation types, hydrodynamic load is based on Morison equation, WAMIT or MacCamy and Fuchs equation. HAWC2 is for horizontal axis turbines but has been extended for vertical axis as well (VAWT) [5], [1]. These models were compared against each other when they were newly developed through the Offshore Code Comparison Collaboration OC3 for IEA in 2010. The compared models performed quite well, however this was attributed to the continuous adjustment and modification of the codes while the task was ongoing [1]. These software packages are very sophisticated and complex, their capabilities include aerodynamic loading, hydrodynamic loading, control system and structural analysis, DNV-GL developed the IceFloe routine for NREL, that allows for ice load calculations and can be used with FAST, HAWC2, ADAMS and Bladed [6]. Another set of routines, the IceDyn was developed the University of Michigan for NREL and the FAST framework and can be used with other wind turbine aeroelastic simulation codes as well [7].

## 1.2. Thesis outline

- Chapter 2: The reference wind turbine: Key information on the used wind turbine and substructure
- Chapter 3: Structural model: Basic formulas to construct the structural model: the mass, damping and stiffness matrices
- Chapter 4: Hydrodynamic loading: Theories that were used to predict the water particle kinematics
- Chapter 5: Soil structure interaction: Applied method and alternative advanced methods towards soil structure interaction
- Chapter 6: Ice structure interaction: Ice induced vibrations in a flexible offshore structure and the approach used to calculate the forces from the incoming ice sheet
- Chapter 7: Aerodynamic loading: Aerodynamic load types and the used model
- Chapter 8: Results
- Chapter 9: Concluding remarks and recommendations for further work

# 2

## The reference wind turbine

The NREL 5-MW reference turbine was created by the National Renewable Energy Laboratory (NREL) of the U.S. Department of Energy, as part of the research for offshore wind technology. It is a realistic detailed design for a reasonably large MW turbine that can be deployed in deep waters. The information on which the design is based on, is gathered from the Multibrid M5000 and the REPower 5M wind turbines, as well as the WindPACT, RECOFF and DOWEC projects.

Furthermore, as part of the UpWind project, support structure concepts have been proposed for this turbine. The concepts include a monopile, a jacket and a floating alternative.

### 2.1. Turbine properties

An overview of the turbine properties of the NREL 5-MW, are listed in Table 2.1.

<b>Property</b>	<b>Value</b>
Rotor, Hub diameter	126m, 3m
Hub height	90m
Cut-in, Rated, Cut-out wind speed	3m/s, 11.4m/s, 25m/s
Cut-in, Rated rotor speed	6.9rpm, 12.1rpm
Rated tip speed	80m/s
Overhang, Shaft tilt, Precone	5m, 5°, 2.5°
Rotor mass	110000kg
Nacelle mass	240000kg
Tower mass	347460kg
Coordinate location of overall CM	-0.2m, 0.0m, 64.0m

Table 2.1: Properties for the upwind 3-bladed NREL 5-MW wind turbine [8].

### 2.2. Rotor nacelle assembly properties

The NREL-5MW offshore wind turbine is a three bladed turbine. The properties of the blades are based on the 62.6m long LM Glasfiber blade. The structural properties are listed in Table 2.2.

<b>Property</b>	<b>Value</b>
Length (w.r.t. root along preconed axis)	61.5m
Mass scaling factor	4.536%
Overall (integrated) mass	17740kg
Second mass moment of inertia (w.r.t. root)	11776047kgm <sup>2</sup>
First mass moment of inertia (w.r.t. root)	363231kgm
CM location (w.r.t. root along preconed axis)	20.475m
Structural damping ratio (all modes)	0.477465%

Table 2.2: Undistributed blade structural properties [8].

The hub is located 5m upwind of the tower centerline, at 90m above the seabed. A summary of the hub and nacelle properties is listed in Table 2.3.

<b>Property</b>	<b>Value</b>
Elevation of yaw bearing above ground	87.6m
Vertical distance along yaw axis from yaw bearing to shaft	1.96256m
Distance along shaft from hub center to yaw axis	5.01910m
Distance along shaft from hub center to main bearing	1.912 m
Hub mass	56780kg
Hub inertia about low-speed shaft	115926kgm <sup>2</sup>
Nacelle mass	240000kg
Nacelle inertia about yaw axis	2607890kgm <sup>2</sup>
Nacelle CM location downwind of yaw axis	1.9m
Nacelle CM location above yaw bearing	1.75m %
Equivalent nacelle-yaw-actuator linear spring constant	9028320000Nm/rad
Equivalent nacelle-yaw-actuator linear damping constant	19160000Nms/rad
Nominal nacelle-yaw rate	0.3°/s

Table 2.3: Nacelle and hub properties [8].

Additional information can be found in [8].

### 2.3. Tower and monopile properties

A summary of the tower and monopile properties can be found in Tables 2.4 and 2.5.

<b>Property</b>	<b>Value</b>
Height above ground	87.6m
Diameter top	4.0m
Diameter bottom	5.6m
Wall thickness top	20mm
Wall thickness bottom	32mm
Overall (integrated) mass	347460kg
CM location (w.r.t. ground along tower centerline)	38.234m
Structural damping ratio (all modes)	1.0 %

Table 2.4: Tower properties [8], [9].

One of the work packages of the UpWind project included the design of substructure concepts for the NREL 5-MW. These were a monopile, a jacket and a floating option. According to [10] the vast majority of the installed offshore wind turbines are supported by a monopile (approximately 81%). Additionally, monopiles appear to still be the most favorable option with a total of 493 monopiles being installed in 2016 in Europe compared to 67 jacket installations as it is shown in Figure 2.1. For this reason the monopile proposed in [9] is selected as the foundation type.

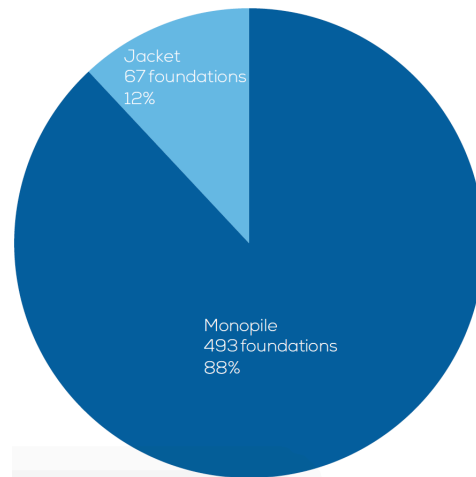


Figure 2.1: Foundation types installed in 2016 (in units) [10].

<b>Property</b>	<b>Value</b>
Interface level	14.76m above MSL
Pile top elevation	5.0m above MSL
Diameter monopile	5.5m
Diameter transition piece bottom	5.9m
Overlap length of transition piece and monopile	8.75m
CM location (w.r.t. ground along tower centerline)	38.234m
Structural damping ratio (all modes)	1.0 %

Table 2.5: Transition piece and monopile properties [8], [9].



# 3

## Structural model

### 3.1. Introduction

The structure is mainly loaded laterally by the aerodynamic, hydrodynamic loading, ice action and soil action. The beam is a structural element that is loaded mainly laterally with respect to its axis. Consequently, the substructure of the offshore wind turbine is modeled as a beam.

The Timoshenko beam theory is considered, accounting for shear deformations and rotational bending stiffness, to obtain the mass and stiffness matrices and eventually solve the equation of motion. The deformed Timoshenko beam element is illustrated in Figure 3.1, showing the stretching, rotation and shear strain of a typical point.

In order to solve the equation of motion and extract the response of the structure over time, when subjected to environmental loading, a numerical model in MATLAB is used. In this model the structure is discretized using finite elements and a cubic shape function. The set of differential equations are solved in the time domain based on an explicit Runge-Kutta formula.

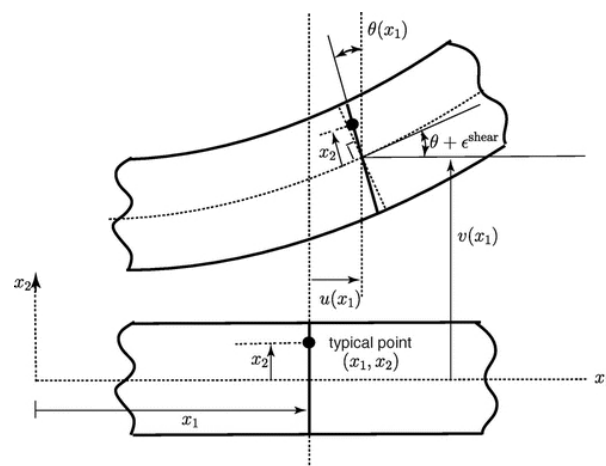


Figure 3.1: Deformation of a Timoshenko beam element [11].

### 3.2. Mass matrix

The derivation of the mass and stiffness matrices is provided in [12]. The translational mass

matrix of an element is a 4x4 matrix, for each element, given by the following expression:

$$M_t = \frac{\rho Al}{(1 + \Phi)^2} \begin{bmatrix} \frac{13}{35} + \frac{7\Phi}{10} + \frac{\Phi^2}{3} & \frac{11l}{210} + \frac{11\Phi l}{120} + \frac{\Phi^2 l}{24} & \frac{9}{70} + \frac{3\Phi}{10} + \frac{\Phi^2}{6} & -\frac{13l}{420} - \frac{3\Phi l}{40} - \frac{\Phi^2 l}{24} \\ \frac{11l}{210} + \frac{11\Phi l}{120} + \frac{\Phi^2 l}{24} & \frac{105}{l^2} + \frac{60}{\Phi l^2} + \frac{120}{\Phi^2 l^2} & \frac{420}{13l} + \frac{3\Phi l}{40} + \frac{24}{\Phi^2 l} & -\frac{140}{l^2} - \frac{60}{\Phi l^2} - \frac{120}{\Phi^2 l^2} \\ \frac{9}{70} + \frac{3\Phi}{10} + \frac{\Phi^2}{6} & \frac{13l}{420} + \frac{3\Phi l}{40} + \frac{\Phi^2 l}{24} & \frac{35}{13} + \frac{7\Phi}{10} + \frac{\Phi^2}{3} & -\frac{11l}{210} - \frac{11\Phi l}{120} - \frac{\Phi^2 l}{24} \\ -\frac{13l}{420} - \frac{3\Phi l}{40} - \frac{\Phi^2 l}{24} & -\frac{l^2}{140} - \frac{\Phi l^2}{60} - \frac{\Phi^2 l^2}{120} & -\frac{11l}{210} - \frac{11\Phi l}{120} - \frac{\Phi^2 l}{24} & \frac{l^2}{105} + \frac{\Phi l^2}{60} + \frac{\Phi^2 l^2}{120} \end{bmatrix} \quad (3.1)$$

The rotary inertia mass matrix of an element is also a 4x4 matrix, for each element, given by the following expression:

$$M_r = \frac{\rho Al}{(1 + \Phi)^2} \left( \frac{r_g}{l} \right)^2 \begin{bmatrix} \frac{6}{5} & \frac{l}{10} - \frac{\Phi l}{2} & -\frac{6}{5} & \frac{l}{10} - \frac{\Phi l}{2} \\ \frac{l}{10} - \frac{\Phi l}{2} & \frac{2l^2}{15} + \frac{\Phi l^2}{6} + \frac{\Phi^2 l^2}{3} & -\frac{l}{10} + \frac{\Phi l}{2} & -\frac{l^2}{30} - \frac{\Phi l^2}{6} + \frac{\Phi^2 l^2}{6} \\ -\frac{6}{5} & -\frac{l}{10} + \frac{\Phi l}{2} & \frac{6}{5} & -\frac{l}{10} + \frac{\Phi l}{2} \\ \frac{l}{10} - \frac{\Phi l}{2} & -\frac{l^2}{30} - \frac{\Phi l^2}{6} + \frac{\Phi^2 l^2}{6} & -\frac{l}{10} + \frac{\Phi l}{2} & \frac{2l^2}{15} + \frac{\Phi l^2}{6} + \frac{\Phi^2 l^2}{3} \end{bmatrix} \quad (3.2)$$

The radius of gyration of the cross section given by:

$$r_g = \sqrt{\frac{I}{A}} \quad (3.3)$$

$\Phi$  is a dimensionless parameter, as it approaches zero the Timoshenko model reduces to the Euler-Bernoulli model, it is given by:

$$\Phi = \frac{12EI\kappa}{GA l^2} = 24\kappa(1 + \nu) \left( \frac{r_g}{l} \right)^2 \quad (3.4)$$

In the case of a hollow circular cross section  $\kappa$  is given by:

$$\kappa = \frac{6(r_{in}^2 + r_{out}^2)(1 + \nu)^2}{7r_{in}^4 + 34r_{in}^2 r_{out}^2 + 7r_{out}^4 + \nu(12r_{in}^4 + 48r_{in}^2 r_{out}^2 + 12r_{out}^4) + \nu^2(4r_{in}^4 + 16r_{in}^2 r_{out}^2 + 4r_{out}^4)} \quad (3.5)$$

The total mass matrix of each element results from the summation of Equations 3.1 and 3.2.

### 3.3. Stiffness matrix

The bending stiffness matrix of an element is given as follows:

$$K_b = \frac{EI}{l^3(1 + \Phi)^2} \begin{bmatrix} 12 & 6l & -12 & 6l \\ 6l & 4l^2 + 2\Phi l^2 + \Phi^2 l^2 & -6l & 2l^2 - 2\Phi l^2 - \Phi^2 l^2 \\ -12 & -6l & 12 & -6l \\ 6l & 2l^2 - 2\Phi l^2 - \Phi^2 l^2 & -6l & 4l^2 + 2\Phi l^2 + \Phi^2 l^2 \end{bmatrix} \quad (3.6)$$

The RNA assembly introduces a significant compressive load on the substructure, to account for this effect on the stiffness as well the compressive load introduced in each element by the weight of the previous one, the geometric matrix of each element has to be taken into account:

$$K_g = \frac{P}{l(1 + \Phi)^2} \begin{bmatrix} \frac{6}{5} + 2\Phi + \Phi^2 & \frac{l}{15} + \frac{\Phi l}{6} + \frac{\Phi^2 l}{12} & -\frac{6}{5} - 2\Phi - \Phi^2 & \frac{l}{30} - \frac{\Phi l}{6} - \frac{\Phi^2 l}{12} \\ -\frac{6}{5} - 2\Phi - \Phi^2 & -\frac{l}{15} - \frac{\Phi l}{6} - \frac{\Phi^2 l}{12} & \frac{6}{5} + 2\Phi + \Phi^2 & -\frac{l}{30} + \frac{\Phi l}{6} + \frac{\Phi^2 l}{12} \\ \frac{l}{10} & -\frac{l^2}{30} - \frac{\Phi l^2}{6} - \frac{\Phi^2 l^2}{12} & -\frac{l}{10} & \frac{2l^2}{15} + \frac{\Phi l^2}{6} + \frac{\Phi^2 l^2}{3} \end{bmatrix} \quad (3.7)$$

### 3.4. Damping matrix

The damping, represents the means by which the system loses energy which consequently results in the reduction of the structure's response. Unlike the mass and stiffness of the system, the damping is difficult to define. Knowledge on the assessment of damping is generally

limited. A decision can be made between applying the same modal damping to all adopted modes, or proportional damping that increases with increasing mode number. In this study proportional damping is used.

Mass participation decreases as the mode index number increases [13]. The natural frequency is given as:

$$\omega_n = \sqrt{\frac{K}{M}} \quad (3.8)$$

thus, with the mass decreasing, the frequency increases, and this is generally observed. The modal damping ratio is:

$$\xi = \frac{C}{C_c} \quad (3.9)$$

Based on the above this ratio increases with increasing modes. Rayleigh damping, is proportional to a linear combination of mass and stiffness.

$$C = \alpha_0 M + \alpha_1 K \quad (3.10)$$

where,  $\alpha_0$  and  $\alpha_1$  are unknown constants. These constants are defined based on two values of the damping ratio, that are presumed known, as follows:

$$a_0 = \frac{2\omega_1\omega_2(\xi_1\omega_2 - \xi_2\omega_1)}{\omega_2^2 - \omega_1^2} \quad (3.11)$$

$$a_1 = \frac{(\xi_2\omega_2 - \xi_1\omega_1)}{\omega_2^2 - \omega_1^2} \quad (3.12)$$

The indexes 1 and 2 denote the two modes where the damping ratio is known. The modal damping ratio then, takes the form:

$$\xi_i = \frac{a_0}{2\omega_i} + \frac{a_1\omega_i}{2} \quad (3.13)$$

which is increasing with increasing frequency.

It should be noted that the presented matrices correspond to one plane, the derivation of the shape functions, that are necessary for the finite element discretization of the beam, for the second plane is presented in [14].



# 4

## Hydrodynamic loading

### 4.1. Introduction

Bottom founded offshore structures are subjected to significant hydrodynamic loading. In the context of the present thesis three different areas are examined with respect to the hydrodynamic loading. The distinction is made based on the wave height. In each area a different theory is used to calculate the water particle hydrodynamics:

1. Linear theory (Airy wave theory), for small wave heights
2. Higher order theory (Stokes 2<sup>nd</sup> order theory), for larger wave heights
3. Linear theory with skewness and asymmetry, for breaking waves

In order to determine the loads exerted on the turbine in the two first areas the Morison equation or the MacCamy & Fuchs equation can be used, while in the last the force is calculated using the Morison equation, according to DNV provisions. In Figure 4.1 the areas where each theory can be applied can be seen. A combination of the water depth, wave height and period define the limits.

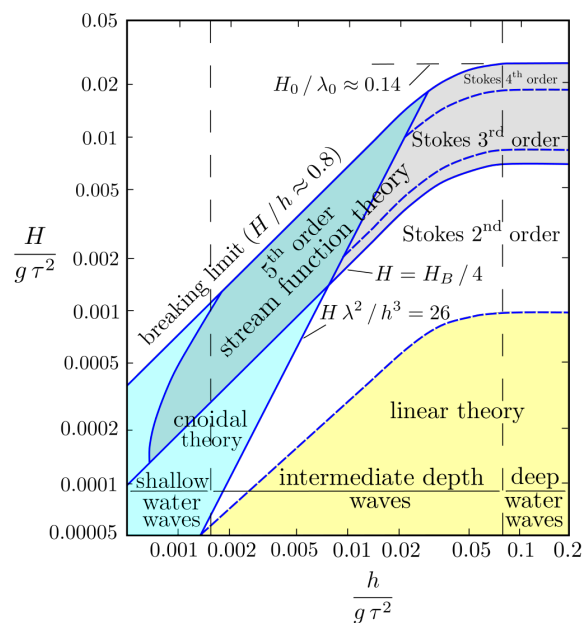


Figure 4.1: Water wave theories [15].

## 4.2. Water particle kinematics

In the following subsections descriptions for the theories that are used to evaluate the hydrodynamic loading can be found.

### 4.2.1. Airy wave theory for small wave heights

In the linear wave theory the kinematics are derived from the velocity potential. More specifically, the horizontal water particle velocity is the derivative of the velocity potential function in the horizontal direction and by definition the acceleration is the time derivative of the velocity. Assuming a sinusoidal wave, the surface elevation profile is given by:

$$\eta(x, t) = \alpha \sin(kx - \omega t + \phi) \quad (4.1)$$

The water particle velocity and acceleration follow from:

$$u_x(x, t) = -\alpha \omega \frac{\cosh(kz)}{\sinh(kd)} \sin(kx - \omega t + \phi) \quad (4.2)$$

$$a_x(x, t) = -\alpha \omega^2 \frac{\cosh(kz)}{\sinh(kd)} \cos(kx - \omega t + \phi) \quad (4.3)$$

In the linear theory the superposition principle can be used. According to this the spectrum can be seen as the superposition of many propagating harmonic waves, each with its own amplitude, frequency, wave length, direction and phase (the random-phase/amplitude model) [16]. This will result in an irregular surface elevation.

For example, for the case of a wave height of 0.5m with a period of 22s, according to Figure 4.1 linear theory can be used. Using linear theory the resulting surface elevation will be a regular, sinusoidal profile, as it is shown in Figure 4.4. However, if one makes use of the superposition principle the result will be irregular and closer to an actual sea state.

The first step to this end, is to create the spectrum. The spectrum, when multiplied with the density and the gravitational acceleration results in the energy that is contained in the signal. Different spectra can be found in literature, most commonly in engineering applications either the JONSWAP or the two parameter Pierson-Moskowitz (PM) spectra are used. Both require a wave height and a period, however for the definition of the JONSWAP spectrum the peakedness of the spectrum is required, which is defined based on three parameters. This peakedness causes the difference in the distribution of energy between the different frequency components. The JONSWAP spectrum is a modification of the PM spectrum, if the peak enhancement factor,  $\gamma$ , is equal to 1 then both spectra are the same. In this thesis the PM spectrum is used.

$$S_{PM}(\omega) = \frac{A_{PM}}{\omega^5} e^{-\frac{B_{PM}}{\omega^4}} \quad (4.4)$$

with,

$$A_{PM} = 487 \frac{H_s^2}{T_p^4} \quad \text{and} \quad B_{PM} = \frac{1949}{T_p^4} \quad (4.5)$$

In order to create the spectrum a choice has to be made regarding the frequency components. With increasing number of harmonic components there is a better distribution of the energy between them, while a few frequency components will result in a more rough representation this effect is seen in Figures 4.2 and 4.3. The choice of 200 harmonic components produces a smoother curve and the difference between the successive frequencies is smaller. With 200 components and the same wave height, an irregular surface profile is created (Figure 4.5), the graph is noisy and completely different than the regular profile. Using the same principle both velocities and accelerations can be produced based on a number of harmonic components. Since different phases are used for the components, the elevation is not zero at  $t=0s$ .

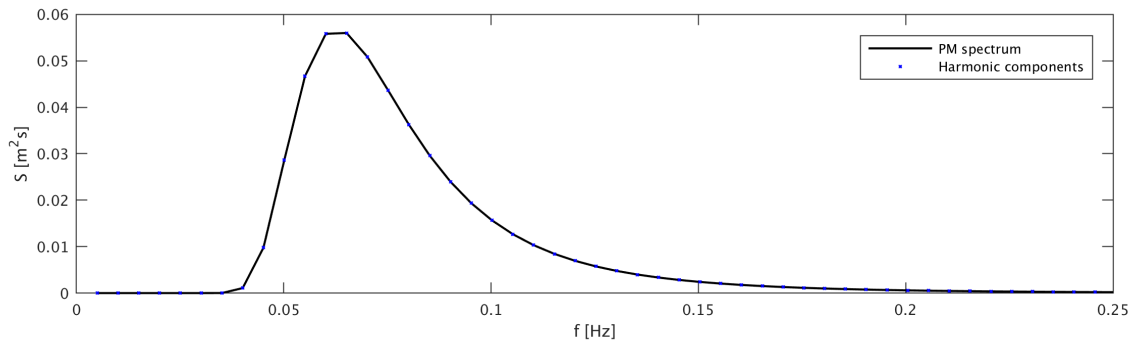


Figure 4.2: PM spectrum for  $H_S=0.5$ ,  $T_P=15.96m$ ,  $d=25m$  and 50 harmonic components.

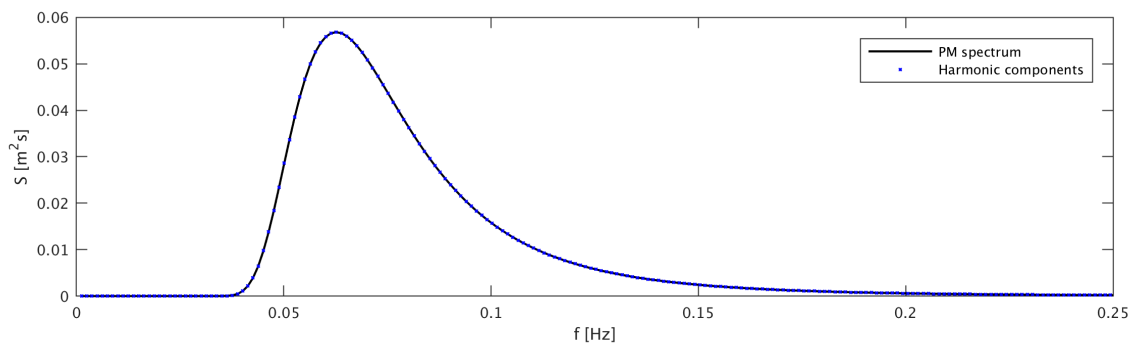


Figure 4.3: PM spectrum for  $H_S=0.5$ ,  $T_P=15.96s$ ,  $d=25m$  and 200 harmonic components.

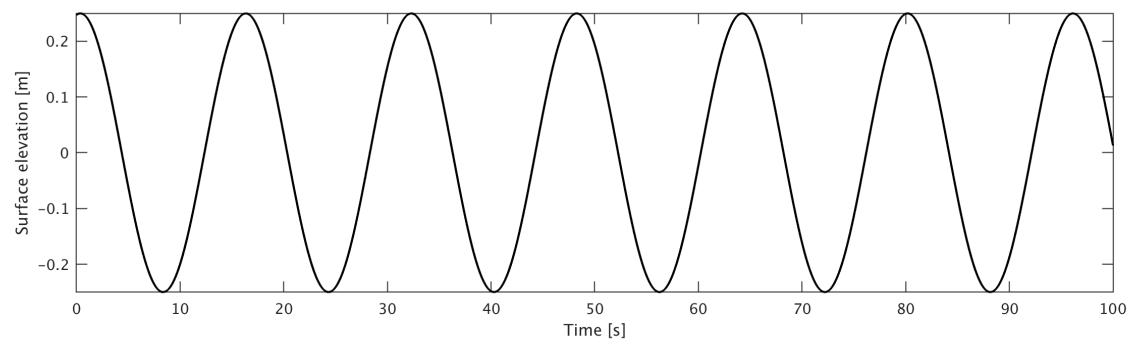


Figure 4.4: Surface elevation for  $H_S=0.5$ ,  $T_P=15.96s$  and  $d=25m$ .

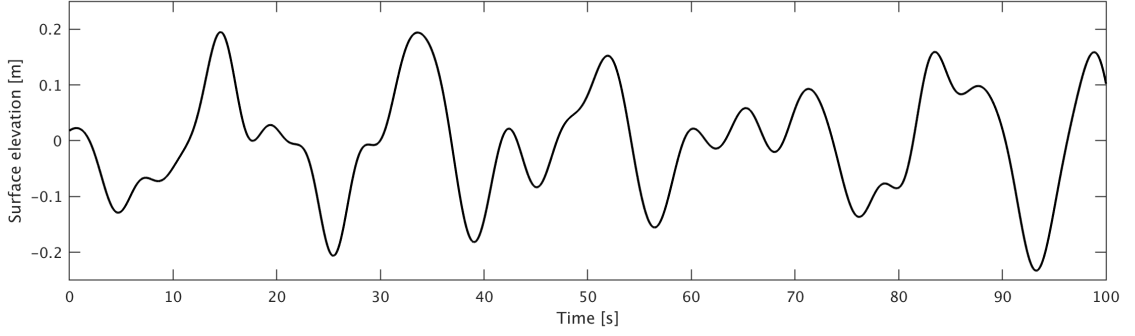


Figure 4.5: Surface elevation for  $H_S=0.5$ ,  $T_p=15.96m$ ,  $d=25m$  using the PM spectrum and 200 harmonic components.

#### 4.2.2. Stokes finite amplitude wave theory for larger wave heights

This theory is valid for  $\frac{H}{d} \ll (kd)^2$ , for  $kd < 1$  and  $\frac{H}{L} \ll 1$ . It is generally not applicable in shallow water due to these conditions [17]. In this theory the velocity potential considers a second order term as well:

$$\Phi_W = \epsilon \Phi_{W1} + \epsilon^2 \Phi_{W2} \quad (4.6)$$

The surface elevation profile is given by:

$$\eta(x, t) = a \cos(kx - \omega t + \phi) + \alpha \frac{k \cosh(kd)}{4 \sinh^3(kd)} (2 + \cosh(2kd)) \cos(2(kx - \omega t + \phi)) \quad (4.7)$$

The horizontal water particle kinematics are given by:

$$u_x(x, t) = \alpha \omega \frac{\cosh(kz)}{\sinh(kd)} \cos(kx - \omega t + \phi) + 3k\alpha^2 \omega \frac{\cosh(2kz)}{4 \sinh^4(kd)} \cos(2(kx - \omega t + \phi)) \quad (4.8)$$

$$a_x(x, t) = \alpha \omega^2 \frac{\cosh(kz)}{\sinh(kd)} \sin(kx - \omega t + \phi) + 3k\alpha^2 \omega^2 \frac{\cosh(2kz)}{2 \sinh^4(kd)} \sin(2(kx - \omega t + \phi)) \quad (4.9)$$

The superposition principle cannot be applied in this case due to the non-linear nature of the equations. The surface profile is illustrated in Figure 4.6 for the a wave height  $H_S=2.5m$  and period  $T_p=22.58s$  using both, the linear theory and the Stokes  $2^{nd}$  order theory. According to Figure 4.1 this set is suitable for the use of the Stokes  $2^{nd}$  order theory:

$$\frac{H}{gT^2} = 0.0005 \quad \text{and} \quad \frac{d}{gT^2} = 0.005 \quad (4.10)$$

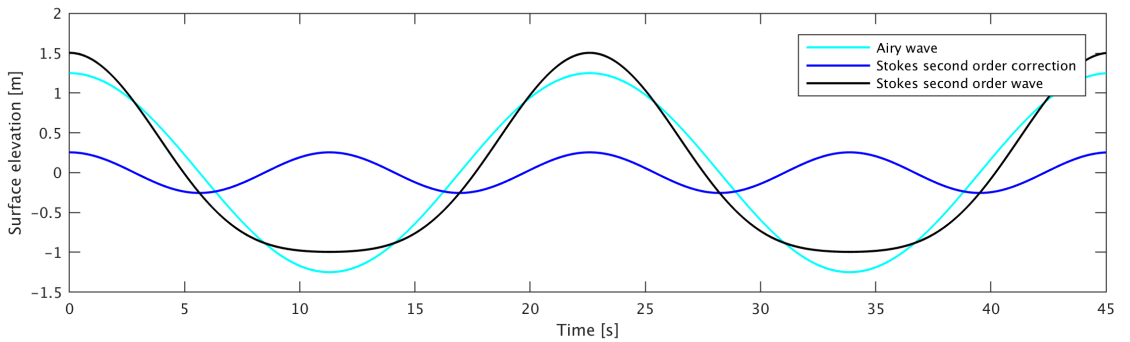


Figure 4.6: Surface elevation for  $H_S=2.5m$ ,  $T_p=22.58s$  and  $d=25m$ .

The Stokes wave has a sharper wave crest and a flatter trough compared to those of the linear wave as a result of the addition of the second order correction term to the linear wave. As both harmonics travel at the same speed and the wave height remains the same, there is no evolution of the surface profile, it remains the same. Furthermore, the crests are located higher than the wave amplitude.

These differences in the surface profile, cause a difference in the underlying water column and the depth that is used to calculate the velocities and accelerations and later on the hydrodynamic forces exerted on the structure. As expected the profile of the velocity follows that of the surface elevation, flatter troughs and sharper crests, this is shown in Figure 4.7.

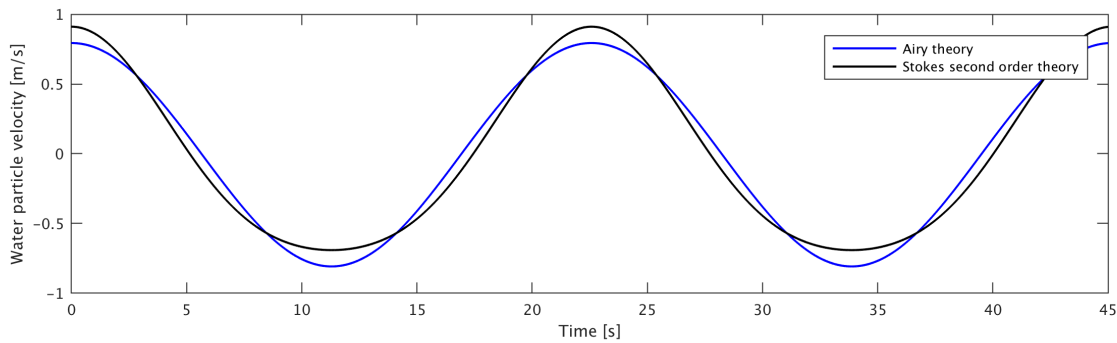


Figure 4.7: Velocity profile for  $H_s=2.5m$ ,  $T_p=22.58s$  and  $d=25m$ .

### 4.2.3. Non-linear orbital velocity for breaking waves

The depth-induced breaking of the waves is a highly non-linear phenomenon and it is not well understood yet. The above theories are not applicable to a breaking wave. An assumption is made in this case to account for the skewness and asymmetry that characterizes the wave shape. The following expression proposed in [18] is used to calculate the horizontal water particle velocity:

$$u_x(x, t) = U_w \sqrt{1-r^2} \frac{\sin(\omega t) + \frac{r \sin \theta}{1+\sqrt{1-r^2}}}{1-r \cos(\omega t + \theta)} \quad (4.11)$$

with  $U_w$  being the water particle velocity as described in the linear theory. The values of  $r$  and  $\theta$  determine the wave shape, accounting for skewness and asymmetry. These can be found through a parametrization as a function of the Ursell number [18]. The Ursell number is a dimensionless number that describes the non-linearity of a wave and is given by [16]:

$$U = \frac{HL^2}{d^3} \quad (4.12)$$

The values of  $r$  and  $\theta$  are found through the total non-linearity  $B$  and phase  $\psi$ .

$$B = p_1 + \frac{p_2 - p_1}{1 + e^{\frac{p_3 - \log U}{p_4}}} \quad (4.13)$$

$$\psi = -90^\circ + 90^\circ \tanh\left(\frac{p_5}{U^{p_6}}\right) \quad (4.14)$$

Using the values, as suggested in [18] with  $p_1=0$ :

$p_2=0.857 \pm 0.016$ ,  $p_3=-0.471 \pm 0.025$ ,  $p_4=0.297 \pm 0.021$ ,  $p_5=0.815 \pm 0.055$ ,  $p_6=0.672 \pm 0.073$ .

Once the values of  $B$  and  $\psi$  are defined, the non linearity parameter  $r$  and the phase  $\theta$  are found through the following equations.

$$B = \frac{3b}{2(1-b^2)} \quad (4.15)$$

$$b = \frac{r}{1 + \sqrt{1 - r^2}} \quad (4.16)$$

$$\theta = -\psi - \frac{\pi}{2} \quad (4.17)$$

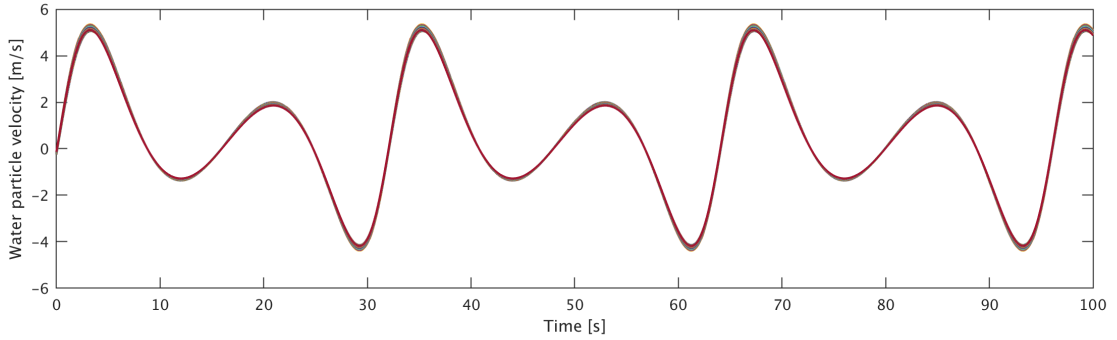


Figure 4.8: Velocity profile for a breaking wave with  $H=20m$ ,  $T=32s$  and  $d=25m$ , for 21 different sets of parameters

The velocity is plotted for 21 values in Figure 4.8 from the minimum until the maximum that each of the parameters can have, with a step of the corresponding deviation divided by ten. The difference in the values of parameters appears to have little influence in the velocity profile. More specifically, the term that is multiplied with the linear velocity was evaluated over this range of parameters separately, the skewness parameter varies only by 2% between minimum and maximum values. The multiplying term is time dependent, over the first 8 seconds the difference in the term drops from 9% to 1%. The velocity profile is more influenced in the case of a smaller wave height, yet not significantly. However, this formula will be used only in the case of the breaking waves, which means in general large wave heights. As there is little influence the mean values of the parameters will be used. The water particle velocity, for a wave that is on the breaking limit, is calculated using the three aforementioned theories, the result is illustrated in Figure 4.9.

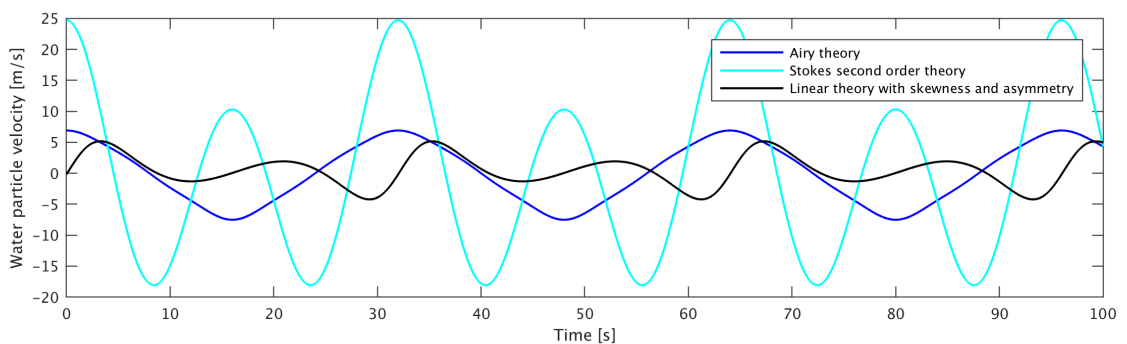


Figure 4.9: Velocity profile for a breaking wave with  $H=20m$ ,  $T=32s$  and  $d=25m$ .

As mentioned in Subsection 4.2.2 the Stokes theory is strictly limited. In this case these conditions are not met and the profile deviates a lot from the previously flatter troughs and sharper crests. Within one wave period the profile reaches 3 maximum values and 2 minimum values instead of 2 and 1 respectively. The velocity profile given by [18], considers, through  $r$  and  $\theta$  the changes in the wave shape. This is assumed to account for the breaking

of the wave in an indirect manner. The surface is also assumed to follow this skewed and asymmetric profile.

### 4.3. Kinematic stretching

The equations for linear waves satisfy the non-linear boundary condition on the mean water level and not at the free surface, making the theory valid for very small wave heights. As a result the water particle kinematics can be predicted from the seabed up to the mean water level, kinematics at the crests and troughs cannot be predicted. In order to predict the kinematics above and below the mean sea level, a wave profile stretching method has to be used. Wheeler stretching is widely used to evaluate the velocities and accelerations. It is a linear stretching (in crests) and compression (in troughs) of the water column. It is done using this formula:

$$z_{new} = d \frac{d+z}{d+\eta} - d \quad (4.18)$$

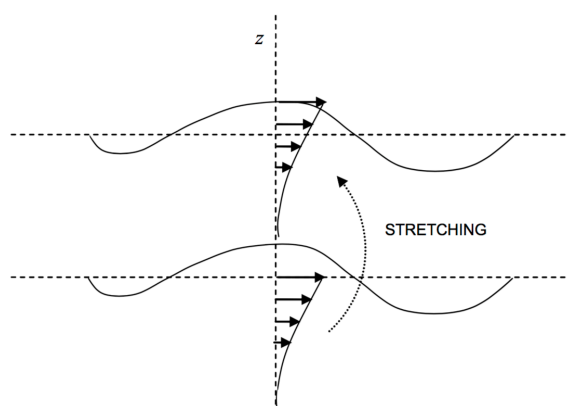


Figure 4.10: Stretching of the surface profile [19].

The Wheeler stretching method was developed for the case of linear waves (Airy). In the case of a non-linear surface profile the Wheeler method can be used and the non-linear kinematics components are added as if they are independent, then the horizontal velocities and accelerations can be modeled up to the free surface [19].

In the case of the Airy waves this method underestimates the velocity at the free surface. In the case of a second order surface elevation, as the Stokes, the method underestimates the velocity around  $z=0m$  and at lower elevations [19].

### 4.4. Hydrodynamic force

There are different methods to calculate the hydrodynamic force acting on an offshore structure. The application of each method depends on the wave height  $H$ , the cross-sectional dimension  $d$  and the wave length  $L$ . The importance of viscous and diffraction effects is what defines these areas of application. When the value of  $\frac{H}{2d}$  becomes large, there is flow separation and loss of energy due to the vortices that are formed. Additionally, when  $\frac{2\pi d}{L} < 1$  it is considered that the wave field is not influenced by the structure's presence. The suitable methods for these areas are:

1. Morison equation, when diffraction effects can be neglected
2. Diffraction theory, when viscous effects can be neglected
3. Either Morison equation or diffraction theory, for small values of  $\frac{H}{2d}$  and  $\frac{2\pi d}{L}$

4. Navier-Stokes equations, when neither diffraction effects nor viscous effects can be neglected

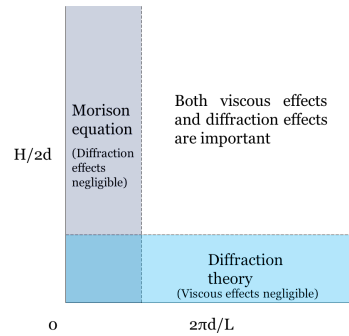


Figure 4.11: Regions of applicability [20].

For the calculation of the hydrodynamic actions acting on slender offshore structures, in most engineering applications the Morison equation is used. If the dimensions of the structure are small with respect to the wave length, the diffraction effects can be neglected and the Morison equation results in a valid engineering solution. However, when the structure's dimensions are larger and in the order of the wave length, then viscous effects are negligible and the most accurate solution is given by the diffraction theory.

In [21] a classification of calculation methods for wave actions is presented. Assuming a real fluid, there is a division on whether the viscous effects on pressures are negligible or not, if they are by following approximate theoretical solutions and assuming potential theory the force is calculated with the diffraction theory. If not, the force is calculated with the Morison equation.

#### 4.4.1. Morison equation

The Morison equation, developed in 1950, provides a solution to the calculation of the hydrodynamic force exerted on a vertical cylinder that is submerged and extends above the free surface. The basic assumption is that the structure's presence does not influence the wave field around it. It consists of two parts, the inertia part and the drag part. The first is proportional to the horizontal acceleration of the water particles and the second is proportional to the square of the horizontal velocity of the water particles, taking into consideration the sign of the velocity. The expression below is for a static structure, if the structure moves the relative velocity and acceleration must be considered. The change in the drag force can lead to hydrodynamic damping. The inertia part is then divided in the Froude-Krylov force and the added mass force, as  $C_M$  can be rewritten as  $C_M=1+C_\alpha$ . The horizontal hydrodynamic force is given as:

$$F(t) = C_M \rho_W \frac{\pi D^2}{4} a_x(t) + \frac{1}{2} C_D \rho_W D u_x(t) |u_x(t)| \quad (4.19)$$

This expression provides the force per meter length of the cylinder. Another limitation of the Morison equation is the uncertainty of the inertia and drag coefficients,  $C_M$  and  $C_D$  respectively. These were initially defined experimentally by Morison by measuring the forces on the structure and the shape of the wave and calculating the velocities and accelerations using linear theory. In this manner, at times of zero velocity and zero acceleration the inertia and drag coefficients were defined respectively. From the limited number of experiments the following range was given [22]:

$$\begin{aligned} C_M &= 1.508 \pm 0.197 \\ C_D &= 1.626 \pm 0.414 \end{aligned}$$

with the Reynolds number  $Re=0.22 \times 10^4 - 1.11 \times 10^4$ . Keulegan and Carpenter studied theoretically and experimentally the forces in an oscillatory flow [23]. In their study the two coefficients appeared to change their value within the wave period, they concluded in relating the mean values of  $C_M$  and  $C_D$  with the Keulegan-Carpenter number:

$$K_C = \frac{u_m T}{D} \tag{4.20}$$

They present the coefficients as a function of the  $K_C$  number, which is related with the flow separation and vortex formation. For a small value there is no separation, for large values ( $K_C \approx 110$ ) Kármán vortices are developed. No influence of the Reynolds number was noticed, which was of the order of  $10^4$ . Several different studies can be found in literature, Trasher and Aagaard [24], Evans [25], Dean and Aagaard [26], Kim and Hibbard [27], Chakrabarti et al [28] have all tried to relate the coefficients with the Reynolds number or the  $K_C$  number. There is however, a lot of scatter in the results and no certain conclusion is drawn. Additionally, there is the issue of the different wave theories used and the limited range of the parameters studied ( $Re, K_C$ ). For this reason the application of these coefficients to a different case, with different environmental data and structural dimensions may be invalid. In the experimental studies of Sarpkaya [29], [30] large ranges in the Reynolds and  $K_C$  numbers were used, additionally the water particle kinematics were measured and not calculated, to eliminate the problem of the different wave theories and possibly steady currents affecting the flow.

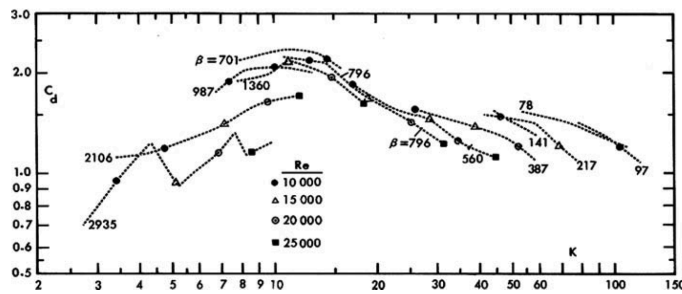


Figure 4.12: Keulegan-Carpenter's drag coefficient as functions of  $K_C$  for 12 values of  $\beta = \frac{Re}{K_C}$  [31].

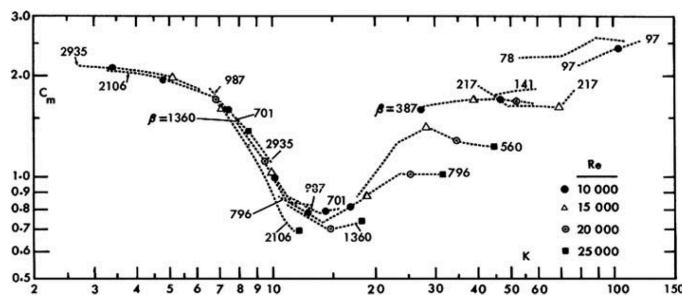


Figure 4.13: Keulegan-Carpenter's inertia coefficient as functions of  $K_C$  for 12 values of  $\beta = \frac{Re}{K_C}$  [31].

The values of  $C_M$  and  $C_D$  to this day, present a lot of uncertainty.

### 4.4.2. Diffraction theory

The Morison equation is considered to be valid for  $\frac{D}{L} < 0.2$ , above this limit diffraction effects

should not be neglected and diffraction theory must be used. The initial analytical solution was given by MacCamy & Fuchs in 1954 with the use of the Bessel functions. The study is for one cylinder. Additional studies have been conducted, Spring and Monkmeyer [32] described an analytical method for an arbitrary number of cylinders and presented results for two cylinders, Chakrabarti [33] used their method for more than two cylinders, for geometries more general than the case of the cylinder, Garrison [34] and Garrison and Stacey [35] presented a linear theory based on the Green functions, Raman et al [36] developed a second order theory for a cylinder, Yue et al [37] presented a hybrid finite element method. The horizontal force exerted on the pile according to MacCamy & Fuchs is given by:

$$F(t) = \frac{2\rho_w g H \cosh(kz)}{k \cosh(kd)} A_{diff} \left(\frac{D}{L}\right) \cos(kx - \omega t + \phi - \alpha_{diff}) \quad (4.21)$$

where

$$\tan \alpha_{diff} = \frac{J'_1\left(\pi \frac{D}{L}\right)}{Y'_1\left(\pi \frac{D}{L}\right)} \quad (4.22)$$

$$A_{diff} \left(\frac{D}{L}\right) = \frac{1}{\sqrt{J_1'^2\left(\pi \frac{D}{L}\right) + Y_1'^2\left(\pi \frac{D}{L}\right)}} \quad (4.23)$$

assuming a wave of the form given in Equation 4.1. This equation was developed using linear theory, assuming a cylindrical shape. If the geometry deviates a lot from the cylindrical shape an example would be the presence of conically shaped pieces in the wave splash zone that are used when ice is present to force the ice sheet to break in bending and not in crushing to reduce the exerted load, then the formula may not produce accurate results. According to [38], for the special case of small pile diameters, the accelerative force of the Morison equation can be identified with the MacCamy & Fuchs force, provided that the  $C_M$  coefficient is taken as 2.

The forces calculated with diffraction theory might exceed those calculated with the Morison equation, for reasons such as:

- the dependence of forces resulting from diffraction theory on the order of the theory used
- the values of  $C_M$  and  $C_D$  present uncertainties

forces and moments resulting from these two methods should not be compared [31].

### 4.4.3. Breaking wave theory

#### Momentum theory

In classical mechanics, momentum is the product of the mass and the velocity of a body. The wave momentum is the product of the mass and the water particle velocity. The rate of change of the momentum, i.e. the momentum flux, is the force contained in the specified volume of water. The horizontal momentum is given by [16]:

$$q_x = \left( \int_{-d}^{\eta} \rho_w u_x dz \right) \Delta x \Delta y \quad (4.24)$$

Which becomes:

$$Q_x = \overline{\int_{-d}^{\eta} \rho_w u_x dz} \quad (4.25)$$

averaged over time and per unit surface area,  $u_x$  is the one described in Equation 4.11. The calculation of the integral is as follows:

$$\overline{\int_{-d}^{\eta} \rho_w u_x dz} = \overline{\int_{-d}^0 \rho_w u_x dz} + \overline{\int_0^{\eta} \rho_w u_x dz} = \frac{\rho_w \alpha^2}{2 \tanh(kd)} \omega \quad (4.26)$$

When assuming linear theory, which is also the case for the velocity of Equation 4.11 as the only depth dependent term is the one contained in  $U_w$ , which is the velocity using linear theory. The integral then takes the following form:

$$Q_x = \frac{\rho_w \alpha^2}{2 \tanh(kd)} \omega \sqrt{1-r^2} \frac{\sin(\omega t) + \frac{r \sin \theta}{1+\sqrt{1-r^2}}}{1-r \cos(\omega t + \theta)} \quad (4.27)$$

For the given water depth and assuming the limit of:

$$\frac{H}{d} = 0.8 \quad (4.28)$$

Any wave with a height larger than  $0.8 \times d$  will break. In order to calculate the forces on the structure when the wave is breaking the momentum flux is utilized.

The main assumption in this case is the description of the water particle hydrodynamics. Neither linear theory, nor Stokes  $2^{nd}$  order theory are applicable to a breaking wave. For this reason the description for the velocity that accounts for asymmetry and skewness is used. To calculate the force based on the momentum flux theory first the momentum has to be calculated. This is done in the following manner:

1. The velocity is integrated over the length of each element that is under water at each time instance
2. Then the time derivative of the result is calculated
3. This is then multiplied with the water density and it is the momentum flux per unit horizontal area

The momentum flux theory as it was presented above was used to investigate the hydrodynamic force. An attempt was made to calculate the force using Newton's second law of motion:

$$\Sigma F = m \alpha \quad (4.29)$$

and compare it with the one resulting from the Morison equation for a non-breaking wave, assuming that since the momentum flux theory could apply to a breaking wave then it should also apply to a non-breaking one. Since the momentum flux essentially produces the acceleration, when taking the time derivative of Equation 4.27, there was a deviation from the Morison equation. The difference was the inertia coefficient. This approach was dismissed and the Morison equation is used instead.

### Impact force

The force from a breaking wave can be alternatively investigated. It can be added as a third component in the Morison equation, an impact force normal to the monopile given as:

$$F(t) = \lambda_c \eta_b \rho_w \frac{D}{2} C^2 (2\pi - 2 \operatorname{artanh}(\sqrt{1 - \frac{C}{4\frac{D}{2}} t}) \sqrt{\frac{C}{\frac{D}{2}} t}) \quad (4.30)$$

that takes place simultaneously along the length of the monopile exposed to the wave, details can be found in [39], [40], [41]. This approach was not examined during this thesis.

### Morison equation

According to the DNV regulations for the design of offshore wind turbines [42], the Morison equation as it is formulated, per unit length, is considered valid to calculate the force exerted from a breaking wave on a vertical element, given that the element is fully submerged. The condition of the elements being fully submerged is taken into in the developed model.



# 5

## Soil structure interaction

### 5.1. Introduction

The foundation of every structure is responsible for the safe transfer of the loads to the soil around it. The main purpose of the design is to limit the soil deformation. The large dimensions of the monopile in combination with the uncertainties and lack of understanding of the behavior of saturated soil under cyclic loading make it difficult to design the substructure.

The monopile is mainly loaded laterally. These lateral loads are the aerodynamic load, the hydrodynamic load, 1P load and 2P/3P loads. Additionally, the structure is subjected to cyclic loading from these. Under cyclic loading the soil is able to dissipate energy through hysteresis. This energy dissipation is described through the damping ratio. The soil structure interaction is crucial when trying to evaluate the longterm behavior of the structure. Soil properties such as:

- shear strain
- saturation
- void ratio
- number of cycles

have an influence on the soil's behavior under cyclic loading.

### 5.2. P-Y curves

As previously mentioned the monopile is subjected to considerable lateral loads due to the combined hydrodynamic and aerodynamic actions. The design regulations (DNV-OS-J101 and API RP 2A-WSD) suggest the use of the so-called p-y curves for laterally loaded piles.

The curves provide the relation between the soil resistance  $p$  when the pile is deflected laterally by a distance  $y$ . The soil is then modeled as a Winkler foundation, the monopile is represented by consecutive beam elements that are supported by uncoupled discrete springs at the nodal points between the elements. The stiffness of the springs results from the p-y curves. It should be noted that the recommended by the code p-y curves have been calibrated for long slender flexible jacket piles, whose diameters can reach up to 1.0m and their bending stiffness is significantly smaller than that of the monopiles. The p-y curves are generally not valid for monopiles [42].

### 5.3. Translation of 3D modeling to simplified springs

With the current practice the first and second natural frequencies, which are close due to symmetry and correspond to bending, of an offshore wind turbine are not accurately predicted. The underestimation of the soil stiffness leads to an underestimation of the natural frequency. A well defined natural frequency is needed to avoid resonance due to hydrodynamic and aerodynamic loading.

In order to accurately define the natural frequency, soil properties are needed. Soil stiffness is dependent on the soil profile, the shape of the embedded structure and the type of the exerted load [43]. For this reason it is troublesome to present a generally applicable method to resolve the issue. Advanced methods as those proposed in [43], suggest seismic measurements as an input. For the investigated structure there are no such measurements available.

An approach to model the soil structure interaction of the NREL-5MW offshore wind turbine with a monopile substructure was recently proposed by [44]. In that study the foundation soil that is considered is a homogeneous deposit of medium dense silica sand. The soil properties considered are presented in the following table.

Property	Value
$G_r$	100MPa
$K_r$	170MPa
$p'_r$	100kPa
$\phi'$	35.5°
$\gamma_{max}$	8.5%
$\phi_{PT}$	31°
$\gamma_{S_{max}}$	0%
$c_1$	0.125 [-]
$c_2$	0.5 [-]
$c_3$	1 [-]
$d_1$	0.25 [-]
$d_2$	3.9 [-]
$d_3$	5.7 [-]
$p'_y$	1.95 [-]

Table 5.1: Sand parameters [44].

A 3D finite element model is created that takes into account the effects of cyclic behavior of the soil. The purpose of the study is to tune spring models for dynamic soil-structure interaction based on the results of a finite element analysis of the soil domain. It is considered to be a simplified but effective manner to consider soil in the dynamic analysis of an offshore wind turbine. In the proposed method, the embedded in the soil part of the monopile is being replaced by soil springs, the model is shown in Figure 5.1. Three different calibrations are performed, based on three wind and wave loading combinations. The proposed properties perform very good when compared to the 3D model, as no significant deviations are observed. The results of the calibrations are summarized below.

Calibration	Translational stiffness $K_{S,L}$	Rotational stiffness $K_{S,R}$	Viscous damping $C_{S,D}$
Simplified model 1	450MNm <sup>-1</sup>	56MNmmrad <sup>-1</sup>	-
Simplified model 2	210MNm <sup>-1</sup>	52MNmmrad <sup>-1</sup>	-
Simplified model 3	90MNm <sup>-1</sup>	40MNmmrad <sup>-1</sup>	20MNm <sup>-1</sup> s

Table 5.2: Calibrated springs for the NREL 5MW offshore wind turbine [44].

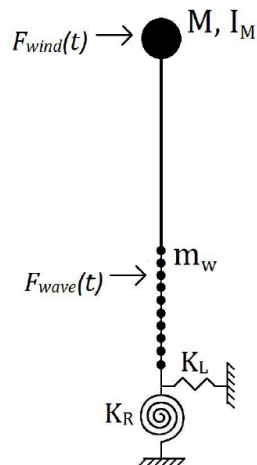


Figure 5.1: Simplified offshore wind turbine model with translational and rotational spring supports [44].

The first case corresponds to a static force and displacement regime, the second to a weak vibration and the last one for a strong vibration with the damper used to represent the energy dissipation due to hysteresis.

There is however, a difference in some of the dimensions that were used to derive this springs with the ones that were used to construct the structural model according to [8] and [9]. Although it is not the best approach, distributed soil springs were used as suggested by the design codes.



# Ice structure interaction

## 6.1. Introduction

The offshore wind industry is expanding to ice infested waters, such as the Baltic Sea. Since this autumn, the world's first offshore wind farm designed to withstand ice loads, the Tahkoluoto offshore wind farm, is producing energy in the Gulf of Bothnia.

According to ISO 19906, various interaction scenarios between ice and structure, failure modes and ice actions can occur. Some of the factors that have a contribution to these are presented below.

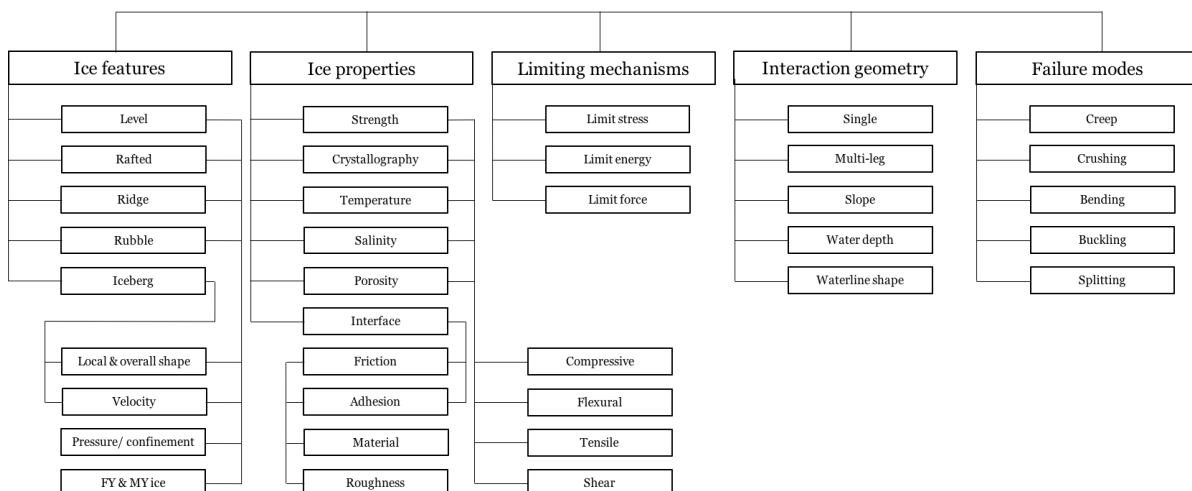


Figure 6.1: Factors influencing interaction scenarios [45].

For vertical cylindrical structures, such as monopiles, dynamic ice structure interaction is of interest. This dynamic interaction is divided into three main types:

1. Intermittent ice crushing
2. Frequency lock-in and
3. Random vibrations due to continuous brittle ice crushing

These vibrations are the result of ice failing in crushing against the structure. The dynamic analysis should be performed so that the structure does not fall into the frequency lock-in type [45]. There is a dependence of the ice sheet velocity and the waterline displacement

of the structure with the regime. In particular, for low velocities intermittent crushing can occur, for intermediate velocities frequency lock-in and for higher velocities continuous brittle crushing. Ice-induced vibrations are not present in rigid structures, additionally some types of vibrations may not occur for each type of flexible structure.

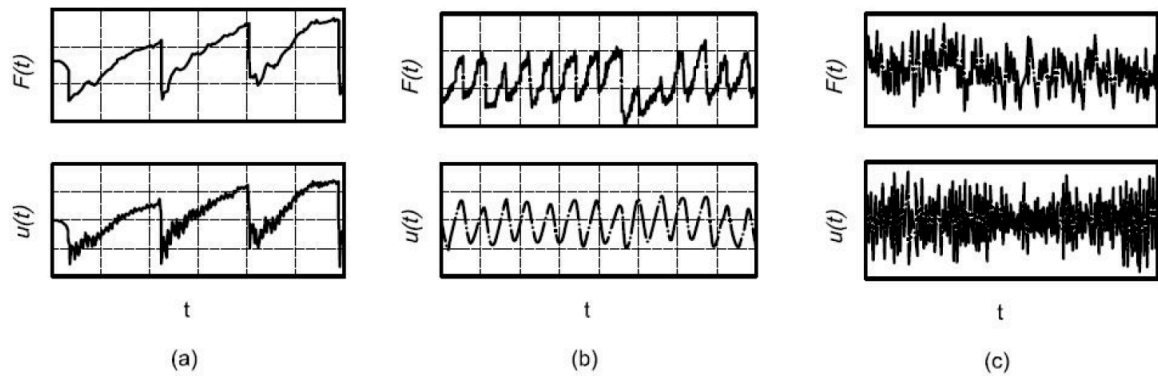


Figure 6.2: Ice action (top) and structural response (bottom) for (a) intermittent crushing (b) frequency lock-in and (c) continuous brittle crushing [45].

## 6.2. Intermittent crushing

As seen in Figure 6.2, ice force and structure displacement are both following a saw-tooth pattern. In the same event an alternating creep and brittle crushing is present [46]. In this regime there is a loading and an unloading phase. When in the loading phase, structure and ice sheet move in the same direction, the ice force increases continuously and the ice edge is deformed in a ductile manner, the ice sheet deflects the structure and undergoes creep deformation. When the ice action reaches its peak, the ice edge deforms in a brittle manner and the unloading phase begins. In the unloading phase, the structural vibrations are decaying, the stored energy in the structure is used to restore the structure in its original position, as the relative speed is high the ice fails in a brittle manner [46]. The total damping in the system is an important factor in the decay of the vibrations. The period of the ice action is much longer than the longest natural period of the structure [45].

## 6.3. Frequency lock-in

The vibrations in this case have a sinusoidal pattern. Similarly to intermittent crushing, there is a loading and an unloading phase. Typically lock-in occurs to some of the lowest natural modes of the structure. Frequency lock-in has been observed for natural frequencies in the range of 0 to 10Hz [47]. As the stiffness and natural frequency increase the frequency lock-in regime moves to lower velocities and the range over which it occurs decreases [47]. As the frequency of the exerted force reaches that of the natural frequency of the structure, the accelerations of the structure are larger when compared to the other regimes.

## 6.4. Continuous brittle crushing

The ice action and the response of the structure do not follow any pattern in this regime but rather they appear to be random, however there is an oscillation around a mean value. This regime is present in all flexible structures for higher indentation velocity [47]. At these high velocity rates the ice is crushing continuously in a brittle manner against narrow and wide structures. During this regime the ice is partially in contact with the structure and a non-uniform pressure is applied to the nominal contact area [46]. The load exerted on the structure is higher in the case of intermittent crushing compared to continuous brittle

crushing.

## 6.5. Formulation of ice elements and ice load around the monopile

In order to calculate the force from the ice sheet the procedure developed by [47], is followed. In order to do so, the ice is represented with a spring-dashpot system. The circumference of the monopile is divided into zones, each with a width of  $w_{zone}$ , where each ice element is acting, as shown in Figure 6.3.

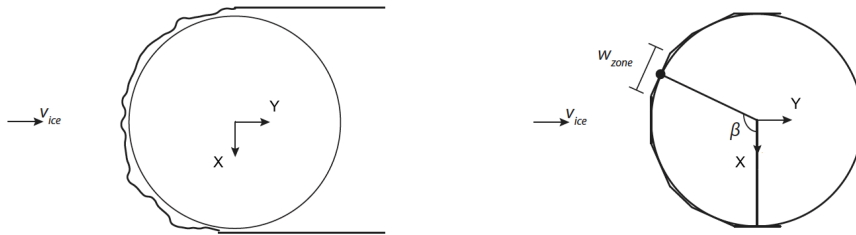


Figure 6.3: Illustration of the contact zones around the monopile [47].

In the case that the load is applied slowly the ice will respond visco-plastically. This means that the ice element will not return to its original state once the load is removed, due to energy dissipation, and the deformation is not recoverable. The elastic response is represented with the spring, the visco-plastic with the dashpots and plasticity with the slider. The configuration of this element is shown below.

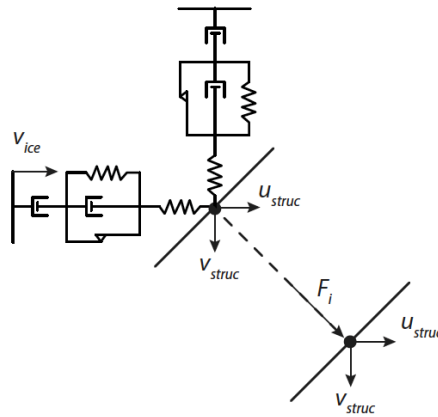


Figure 6.4: Ice element [47].

The force exerted on each of the zones, in the x and y directions, is given by [47]:

$$F_{y,i} = \sin^2(\beta_i)K_2(u_{i,1} - u_s) + \cos(\beta_i)\sin(\beta_i)K_2(v_{i,1} - v_s) \quad (6.1)$$

$$F_{x,i} = -\sin(\beta_i)\cos(\beta_i)K_2(u_{i,1} - u_s) + \cos^2(\beta_i)K_2(v_{i,1} - v_s) \quad (6.2)$$

More details on the equation of motion of the elements can be found in [47]. The model allows for the calculation of the ice load, provided that reference values are known for the ice conditions that are investigated.



# 7

## Aerodynamic loading

### 7.1. Introduction

Wind is one of the most important environmental loads in offshore structures, and even more in offshore wind turbines. Wind is not constant, it can vary both in speed and direction. Due to the relatively flat and smooth water surface the flow is generally horizontal. The importance of the wind load depends on the nature of the structure, in stiff structures the wind load adds up to about 15% of the total environmental load [21]. In the case of the offshore wind turbine wind load must be considered carefully and thoroughly.

The wind generated forces directly exerted on the structure can be divided into two parts, the aerodynamic load acting on the blades and the aerodynamic drag force acting along the length of the tower and the exposed to the wind part of the transition piece. The former is present during operation, parking and idling, braking and start-up.

### 7.2. Rotor model

A three bladed rotor is presented below, where the Y axis coincides with the rotational axis of the rotor. For the specific case of a rotor with identical blades, which is the case of the NREL-5MW turbine, mass, stiffness and damping matrices have been developed by [48] to represent the rotor. Due to the fact that the first natural frequency of the blades is a lot higher than the first natural bending frequency of the complete structure, the blades can be assumed to be rigid.

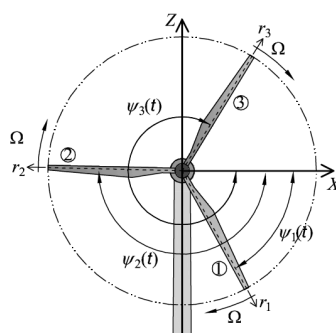


Figure 7.1: Definition of the rigid rotor model indicating the azimuths  $\Psi_1$ ,  $\Psi_2$ ,  $\Psi_3$ , of the blades and the rotational velocity  $\Omega$  [48].

The mass matrix is given as:

$$M_R = \int_{r_0}^R m_j(r_j)r_j \begin{bmatrix} \frac{3}{r_j} & 0 & 0 & 0 & 0 & 3\frac{d}{r_j} \\ 0 & \frac{3}{r_j} & 0 & 0 & 0 & 0 \\ 0 & 0 & \frac{3}{r_j} & -3\frac{d}{r_j} & 0 & 0 \\ 0 & 0 & -3\frac{d}{r_j} & \frac{3}{2}r_j + 3\frac{d^2}{r_j} & 0 & 0 \\ 0 & 0 & 0 & 0 & 3r_j & 0 \\ 3\frac{d}{r_j} & 0 & 0 & 0 & 0 & \frac{3}{2}r_j + 3\frac{d^2}{r_j} \end{bmatrix} dr_j \quad (7.1)$$

The damping matrix is:

$$C_R = \int_{r_0}^R m_j(r_j)r_j\Omega r_j \begin{bmatrix} 0 & 0 & 0 & 0 & 0 & 0 \\ 0 & 0 & 0 & 0 & 0 & 0 \\ 0 & 0 & 0 & 0 & 0 & 0 \\ 0 & 0 & 0 & 0 & 0 & 3r_j \\ 0 & 0 & 0 & 0 & 0 & 0 \\ 0 & 0 & 0 & -3r_j & 0 & 0 \end{bmatrix} dr_j \quad (7.2)$$

And the stiffness:

$$K_R = \mathbf{0}_{6 \times 6} \quad (7.3)$$

The rotor does not contribute to the total stiffness, hence it is a zero matrix. Details on the derivation of these matrices can be found in [48].

### 7.3. Aerodynamic load on the blades

A wind signal is necessary to generate the aerodynamic load acting on the RNA assembly. For this reason a turbulent wind signal is considered. This signal was created with Bladed in [49].

That signal is used to evaluate the aerodynamic force. The aerodynamic force that is proposed in [49] is a result of the combined effect and actions of wind speed, pitch angle, rotational speed of the turbine, induction factor and the structure's acceleration and velocity.

### 7.4. Aerodynamic load on the tower

The aerodynamic drag force is a distributed load over the length of the tower. The formulation is similar to that of the drag term in the Morison equation. The aerodynamic drag force per unit length of the tower and the exposed to the air transition piece is given by:

$$F_{D_{wind}} = \frac{1}{2} C_D \rho_{air} u_{wind}^2 D \quad (7.4)$$

and it is dependent on the diameter  $D$  of the structure at each elevation.

The wind signal can be transferred to each elevation by making use of the power law.

$$u_{wind}(z) = u_{wind}(z_{ref}) \left( \frac{z}{z_{ref}} \right)^{\alpha_{air}} \quad (7.5)$$

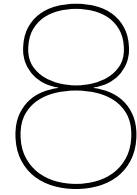
The exponent  $\alpha_{air}$  is derived empirically, for the case of open water a value of  $\alpha_{air} = 0.11$  is assumed. The simplest approach to the selection of the drag coefficients is given by API and SNAME based on the smoothness of the cylinder [50].

	<b>Smooth</b>	<b>cylinder</b>	<b>Rough</b>	<b>cylinder</b>
	$C_D$	$C_M$	$C_D$	$C_M$
API	0.65	1.6	1.05	1.2
SNAME	0.65	2.0	1.0	1.8

Table 7.1: Indicative coefficients for cylindrical members according to API and SNAME.

In the case of the NREL-5MW, with the assumption of a smooth cylinder the value of  $C_D=0.65$  can be used.





# Results

## 8.1. Modal analysis

In the manner that the problem is formulated, each node of the structure has five degrees of freedom (two translational and three rotations), when a sensible number of nodes is selected it will result in large sized mass, damping and stiffness matrices. This will have an impact on the computational time. For this reason modal analysis was employed.

In modal analysis a summation of synchronized motions is assumed. The motion is represented by a superposition of the normal modes of the free undamped vibrations [51]. The coupled equations of motion are then transformed into uncoupled. The matrices are reduced based on the selected number of modes. Every uncoupled equation is analogous to the equation of motion for a single degree of freedom system.

So essentially the multi degree of freedom system is reduced to a number of single degree of freedom systems and the number of equations to be solved is reduced. This reduction has a significant impact on the running time of the model. The physical response of the multi degree of freedom system can be reproduced using the modal responses of the single degree of freedom systems.

The first three modes for both planes are presented below. The mode shapes resemble those of the cantilever beam. It is expected that the mode shapes in the two planes will be similar due to the symmetry of the structure. The mode shapes have not been normalized and are shown in Figures 8.1 and 8.2.

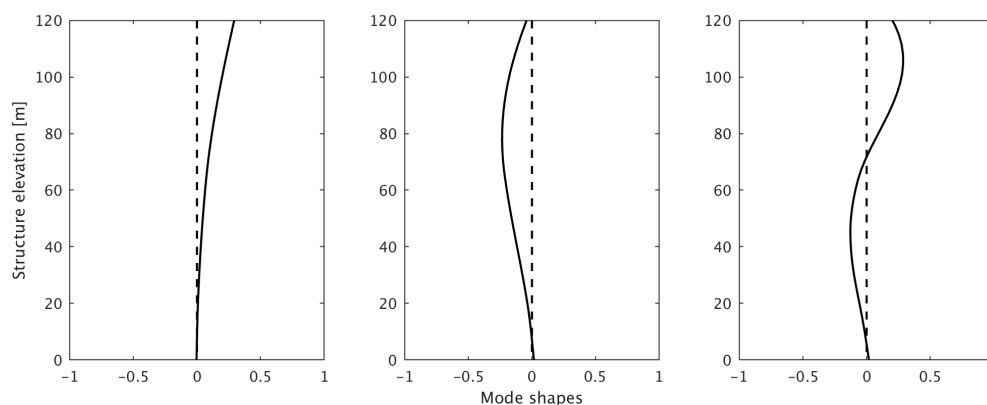


Figure 8.1: From left to right the first, second and third mode in the XZ plane (Side-Side motion).

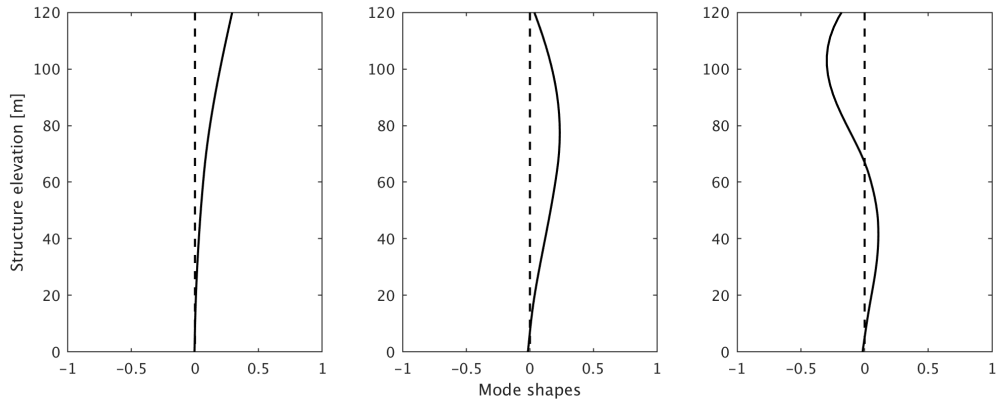


Figure 8.2: From left to right the first, second and third mode in the YZ plane (Fore-Aft motion).

The estimated first natural frequency is deviating from the one calculated in [52] due to the changes in geometry. The used natural frequencies in the modal analysis are presented here.

Number	XZ plane	YZ plane	Yaw axis
1	0.24Hz	0.24Hz	1.68Hz
2	1.21Hz	1.24Hz	13.41Hz
3	2.79Hz	3.10Hz	23.57Hz
4	5.42Hz	5.87Hz	37.51Hz
5	9.24Hz	9.51Hz	48.25Hz
6	14.25Hz	14.38Hz	60.05Hz
7	18.52Hz	18.58Hz	72.31Hz
8	22.68Hz	22.76Hz	87.08Hz
9	31.30Hz	31.35Hz	96.38Hz
10	38.08Hz	38.12Hz	113.49Hz

Table 8.1: The first thirty natural frequencies of the structure in Hz.

## 8.2. Aerodynamic load

For the calculation of the aerodynamic load, a turbulent wind signal was used. The wind speed is at all times above the rated wind speed and has a mean speed of 15m/s. The signal is presented in Figure 8.3.

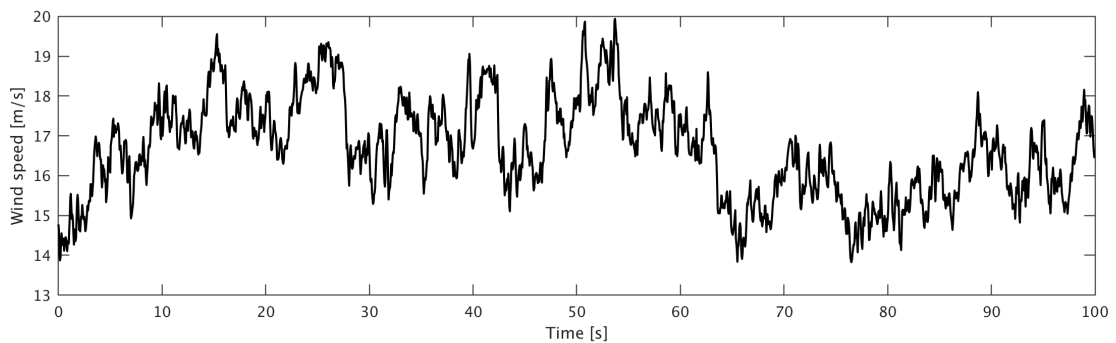


Figure 8.3: Turbulent wind signal at the hub height.

The signal provides the wind speed at the hub height, which is then transferred to the corresponding elevations of the tower and the transition piece using the power law.

The response is calculated first for the aerodynamic load acting on the blades. The Fore-Aft motion in the YZ plane (Figure 8.4), is dominating the response of the structure, as the direction of the wind is parallel to this direction. There is no wind component in the XZ plane, the response is shown in Figure 8.5.

During the analysis a set of static deflection is created and used as initial conditions for the structure. The deflection is calculated by using the following equation:

$$u_{static} = \frac{F_{mean}}{K} \quad (8.1)$$

The mean force is a lift force and a result of the combined contributions of the angle of attack, the camber of the airfoils and drag generated by the rotor. The turbine is oscillating, in both planes, around a mean value that is not zero, indicating this static deflection.

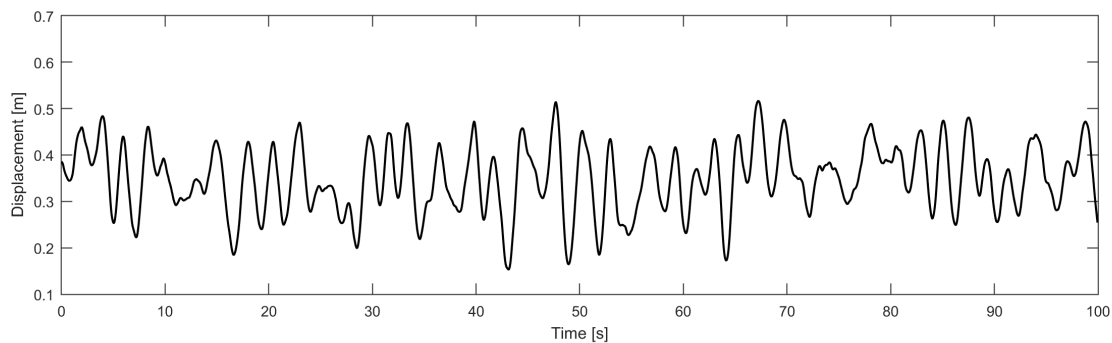


Figure 8.4: Displacement of the RNA in the YZ plane (Fore-Aft motion).

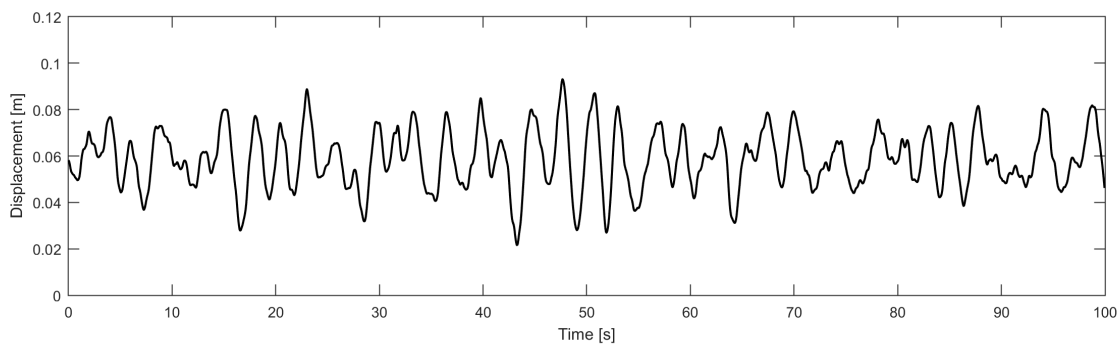


Figure 8.5: Displacement of the RNA in the XZ plane (Side-Side motion), resulting from the aerodynamic load on the blades.

The next step is to include the drag force, as described in Section 7.4. Note that for this stage the response is examined only for the load resulting from the wind, therefore no waves are included and the surface elevation is constant at the mean water level.

The response in the Fore-Aft and Side-Side directions are presented in Figures 8.6 and 8.7. The RNA is oscillating in a random pattern without a clear frequency.

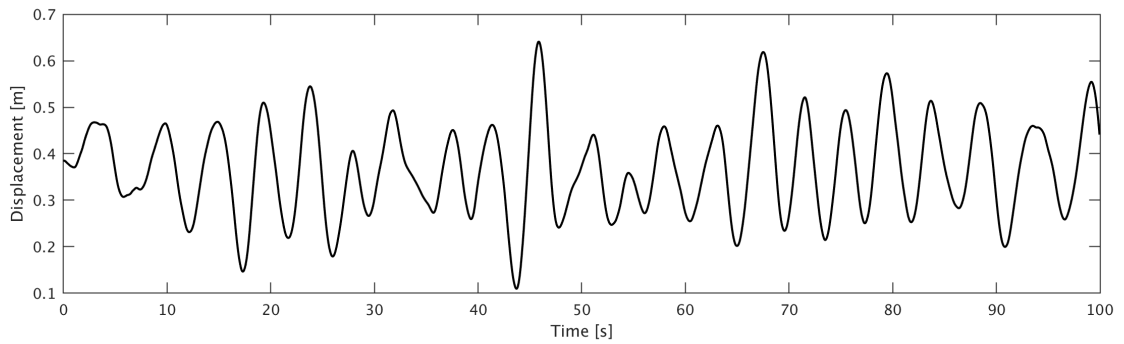


Figure 8.6: Displacement of the RNA in the YZ plane (Fore-Aft motion), resulting from both the aerodynamic load on the blades and the drag force on the exposed elements.

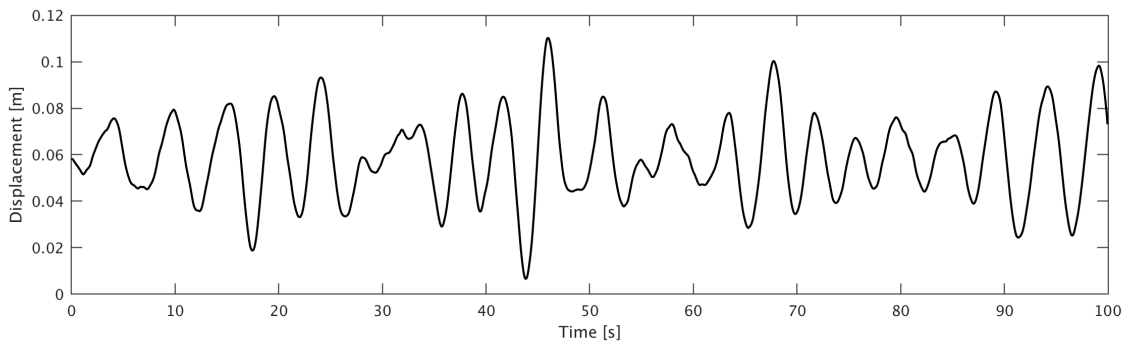


Figure 8.7: Displacement of the RNA in the XZ plane (Side-Side motion), resulting from both the aerodynamic load on the blades and the drag force on the exposed elements.

The response was transferred to the frequency domain by means of Fast Fourier Transform (FFT). Most of the energy is stored in the first natural frequency, this is indicated by the peak near this frequency in both planes, Figures 8.8 and 8.9. The peak before that could be the frequency of the exerted load.

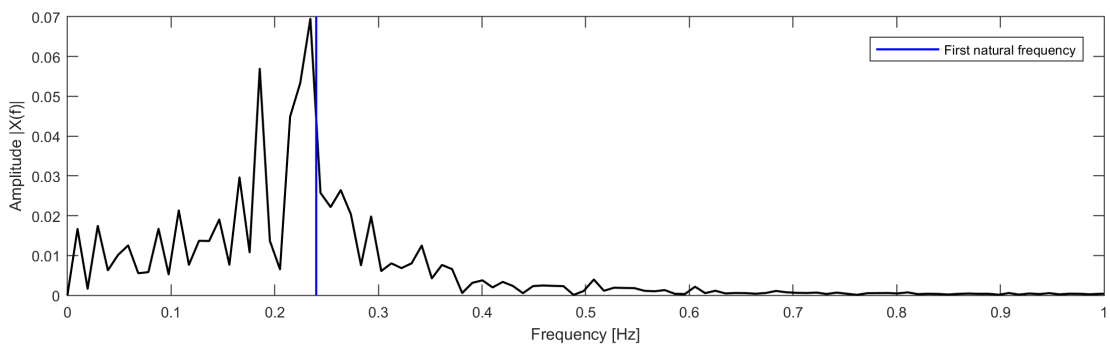


Figure 8.8: Single sided amplitude spectrum of the response of Figure 8.6.

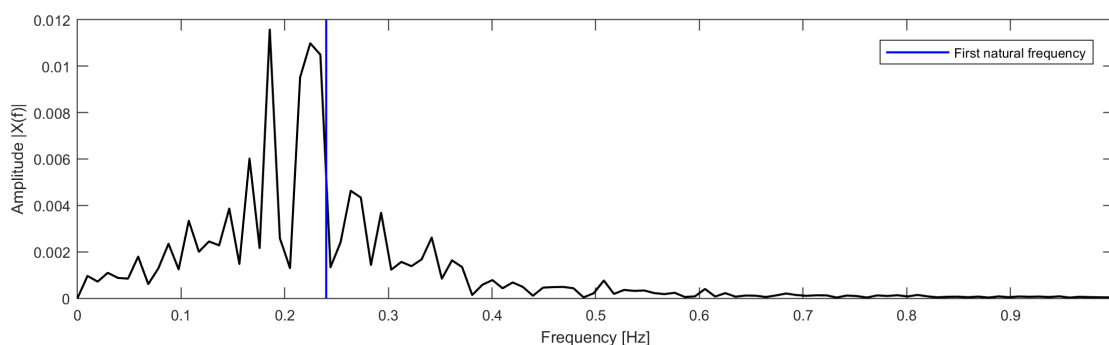


Figure 8.9: Single sided amplitude spectrum of the response of Figure 8.7.

Note that the amplitude in the plots above, as in other frequency plots that follow has been normalized with the sampling number. Frequencies above  $1\text{Hz}$  in both cases are not of significance as the amplitude is zero or very small compared to the smaller frequencies.

### 8.3. Hydrodynamic load

The cases presented in this section correspond to an incoming wave with an angle of  $0^\circ$ , consequently no motion in the XZ plane is expected. Cases are run using both the Morison equation and the MacCamy and Fuchs equation. As previously mentioned a comparison between the results that these methods produce should not be performed.

The displacement of the structure in the Fore-Aft direction is presented in Figures 8.10 and 8.12 and the corresponding amplitude spectra in Figures 8.11 and 8.13. The displacement follows a random pattern and the amplitude is very small regardless of the hydrodynamic force calculation method, there is no static deflection in this case therefore the oscillation is around zero.

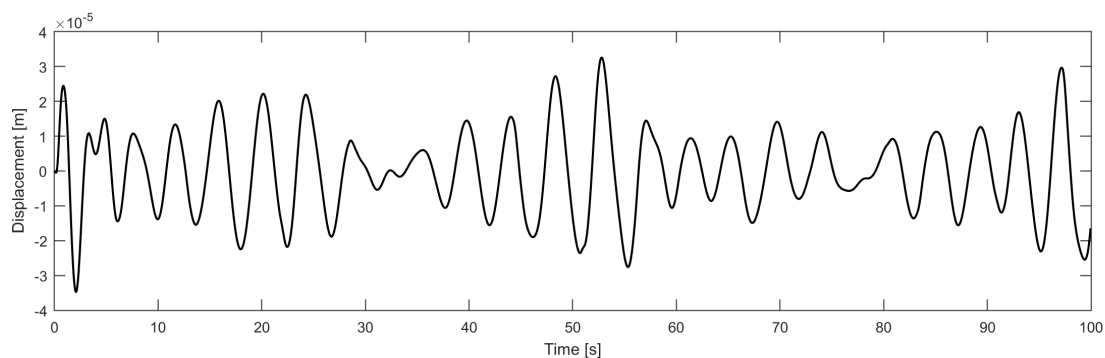


Figure 8.10: Displacement of the RNA in the YZ plane (Fore-Aft motion), resulting from the Airy wave theory and the Morison equation, for a wave height of  $H_S=0.5\text{m}$  and  $T_P=15.96\text{s}$ .

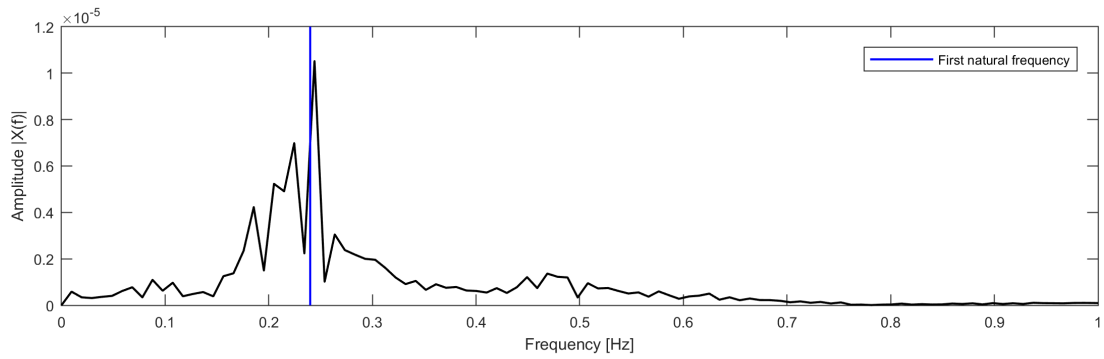


Figure 8.11: Single sided amplitude spectrum of the response for the same conditions as in Figure 8.10.

The plot in the frequency domain indicates that in the examined case the frequency that is of importance is the first natural frequency of the structure. The signal is decaying after that point and no other peak is observed.

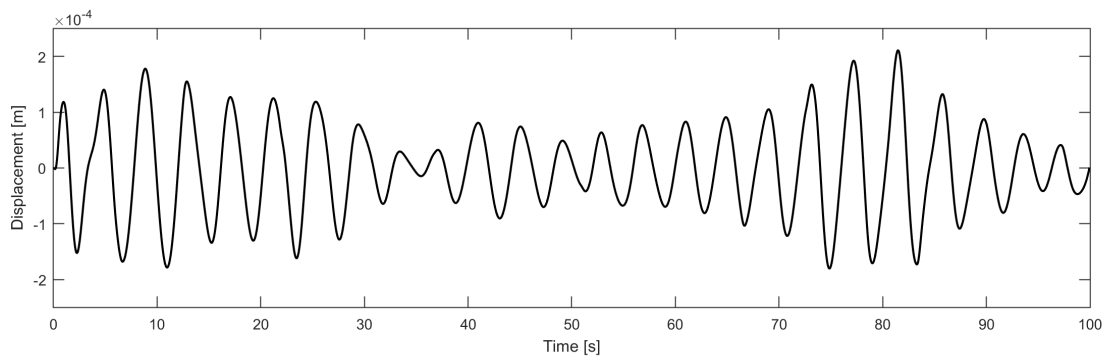


Figure 8.12: Displacement of the RNA in the YZ plane (Fore-Aft motion), resulting from the diffraction theory and the MacCamy and Fuchs equation, for a wave height of  $H_S=0.5m$  and  $T_P=15.96s$ .

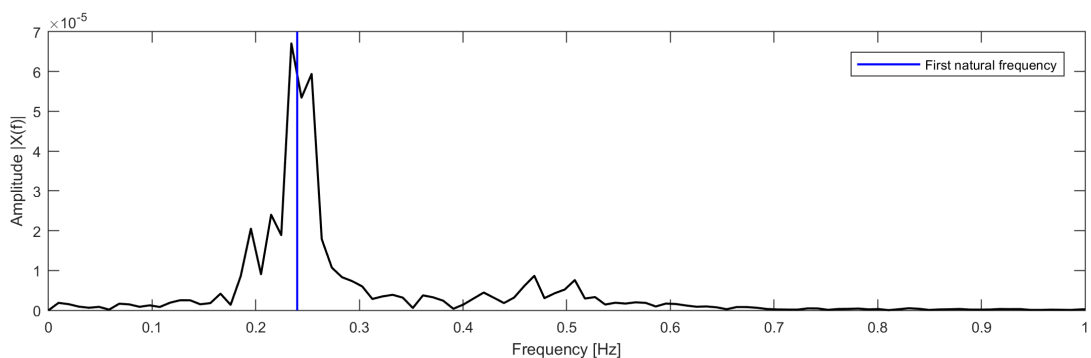


Figure 8.13: Single sided amplitude spectrum of the response for the same conditions as in Figure 8.12.

The plot in the frequency domain has a peak near the first natural frequency of the structure. Since superposition is employed there is no clear frequency in the signal when viewing the

response in the time domain, however both spectra indicate a peak right after  $0.2\text{Hz}$  that could be the main loading frequency.

In Figure 8.14, the displacement in the Fore-Aft direction is shown when the load is calculated with the Morison equation, the signal is sinusoidal as there is one frequency in the load and there is no superposition used, so the structure is vibrating to the frequency of the applied load. The displacement is larger due to the larger wave height, and consequently water particle kinematics. The corresponding amplitude spectrum is presented in Figure 8.15.

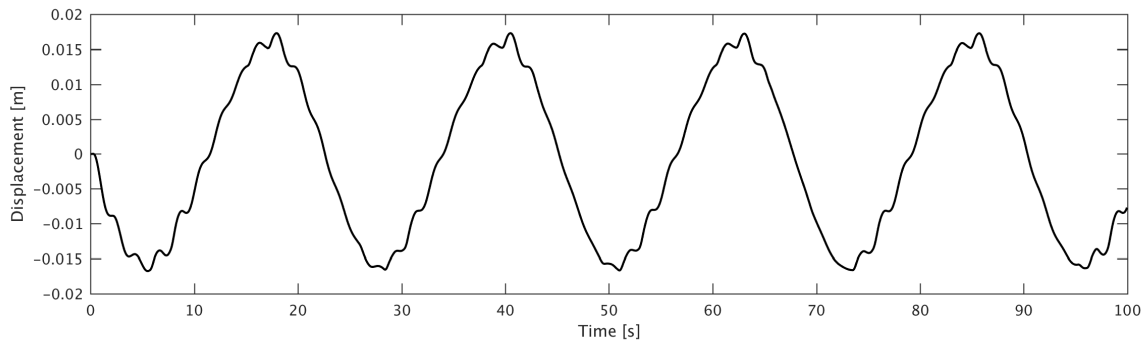


Figure 8.14: Displacement of the RNA in the YZ plane (Fore-Aft motion), resulting from the Stokes theory and the Morison equation, for a wave height of  $H_S=2.5\text{m}$  and  $T_p=22.58\text{s}$ .

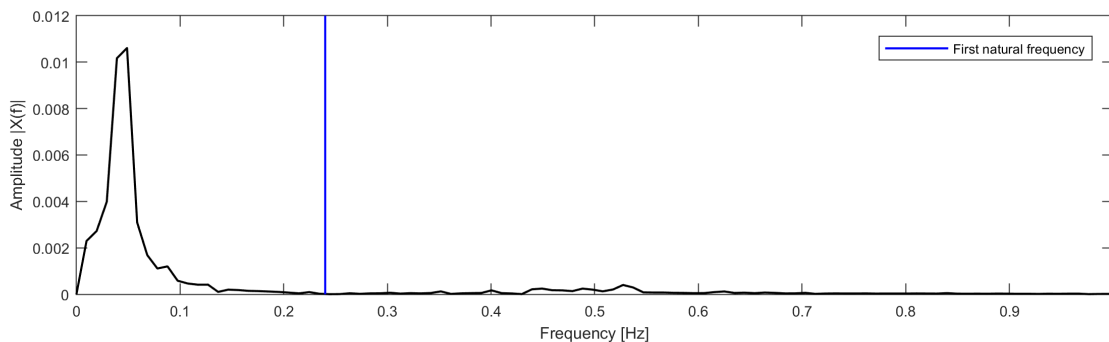


Figure 8.15: Single sided amplitude spectrum of the response for the same conditions as in Figure 8.14.

In the case of the Stokes wave, the signal has a distinct frequency based on the period of the wave, in this particular case that is  $0.044\text{Hz}$ , and is also indicated by the peak in the plot in the frequency domain.

The response in the same direction using the MacCamy & Fuchs equation is shown in Figure 8.16, the signal is again random as the water particle kinematics are calculated using linear theory and the superposition principle. Therefore, the previously distinct frequency of the wave is no longer present in the new signal. The displacement of the structure is larger in the case of the Stokes wave when compared with the Airy, this is due to the fact that the wave height is larger in the case of the Stokes. The amplitude spectrum is shown in Figure 8.17. The amplitude spectrum appears to be odd. There is no peak at the natural frequency, and the two peaks in the range between  $0.1$  and  $0.2\text{Hz}$  cannot be explained.

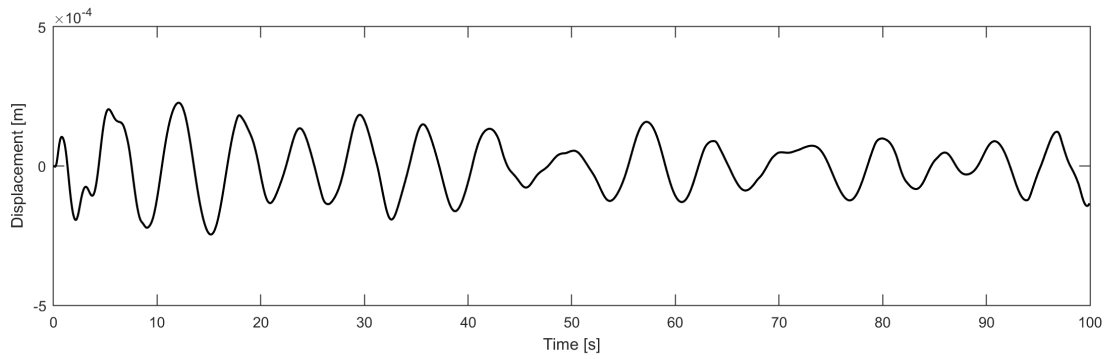


Figure 8.16: Displacement of the RNA in the YZ plane (Fore-Aft motion), resulting from the diffraction theory and the MacCamy and Fuchs equation, for a wave height of  $H_S=2.5m$  and  $T_P=22.58s$ .

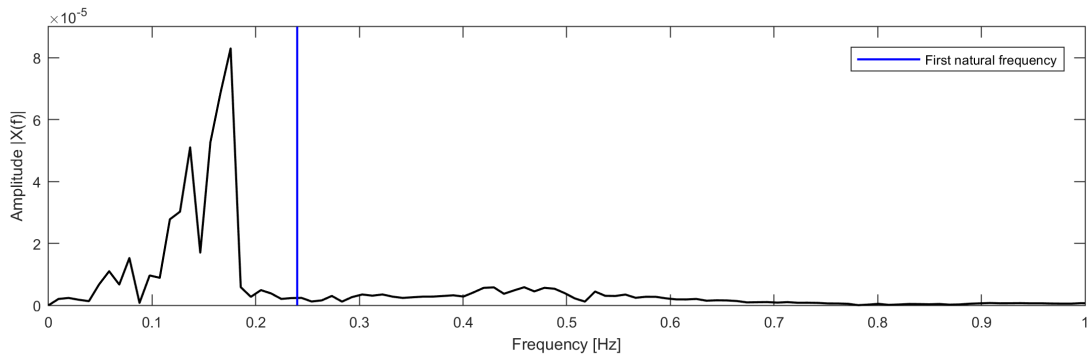


Figure 8.17: Single sided amplitude spectrum of the response for the same conditions as in Figure 8.16.

The strict limitations of the Stokes second order theory render it invalid in the area that the Airy theory is applicable and vice versa. To evaluate the error in the calculations where the linear theory is no longer valid, the response is calculated for the area where the Stokes is applicable using both theories, the result is shown in Figure 8.18.

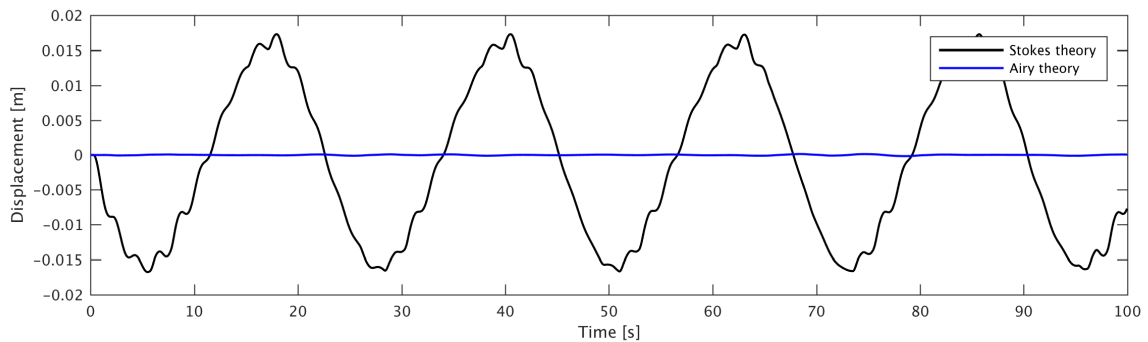


Figure 8.18: Displacement of the RNA in the YZ plane (Fore-Aft motion), resulting from the Stokes vs the Airy theory and the Morison equation, for a wave height of  $H_S=2.5m$  and  $T_P=22.58s$ .

The Airy theory produces a displacement that is very small compared to the one with the Stokes theory, and when plotted together resembles a line of nearly zero. For this reason it was plotted separately as well (Figure 8.19).

When comparing Figures 8.14 and 8.19, the response in the latter is random and from the time domain plot is difficult to extract frequency information. This is a result of the superposition principle and the different frequency components that compose the wave signal. As the superposition cannot be applied in the case of the Stokes 2<sup>nd</sup> order theory, the signal is made of one component and the frequency of the response is the same as that of the wave signal.

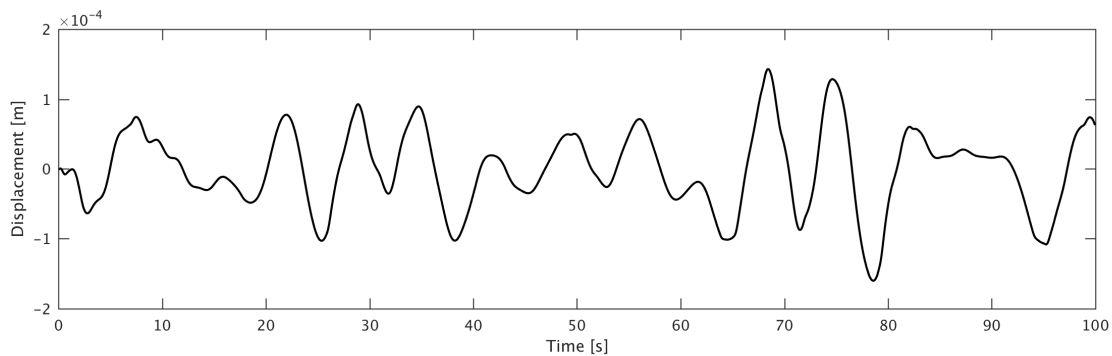


Figure 8.19: Displacement of the RNA in the YZ plane (Fore-Aft motion), resulting from the Airy theory and the Morison equation, for a wave height of  $H_S=2.5m$  and  $T_P=22.58s$ .

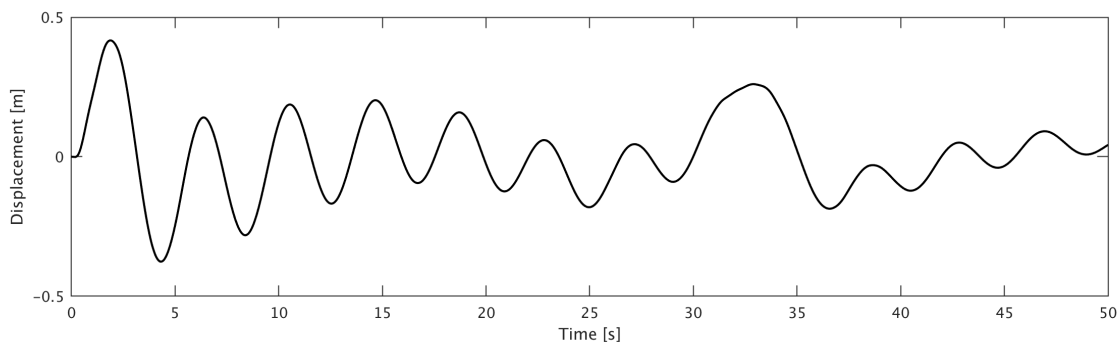


Figure 8.20: Displacement of the RNA in the YZ plane (Fore-Aft motion), for a wave height of  $H_S=20m$  and  $T_P=32s$ .

The response shown in Figure 8.20 is that in the assumed case of a breaking wave. The corresponding amplitude spectrum shown in Figure 8.21 shows a peak near the natural frequency and near the frequency of the applied load which is  $0.03Hz$ .

For the particular depth, such a wave height is rather extreme, for this reason it is just presented here and does not constitute a solid solution to the problem that is the force exerted from a breaking wave.

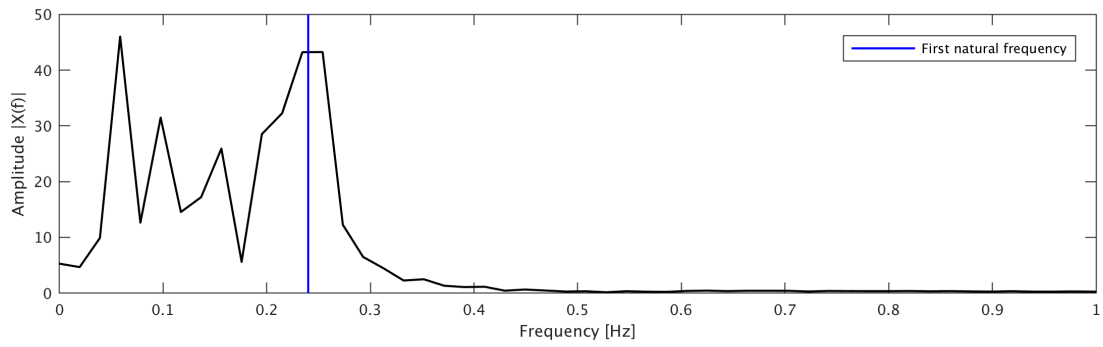


Figure 8.21: Single sided amplitude spectrum of the response for the same conditions as in Figure 8.20.

There is no vibration in the XZ plane for these cases, therefore the response is only plotted once in Figure 8.22.

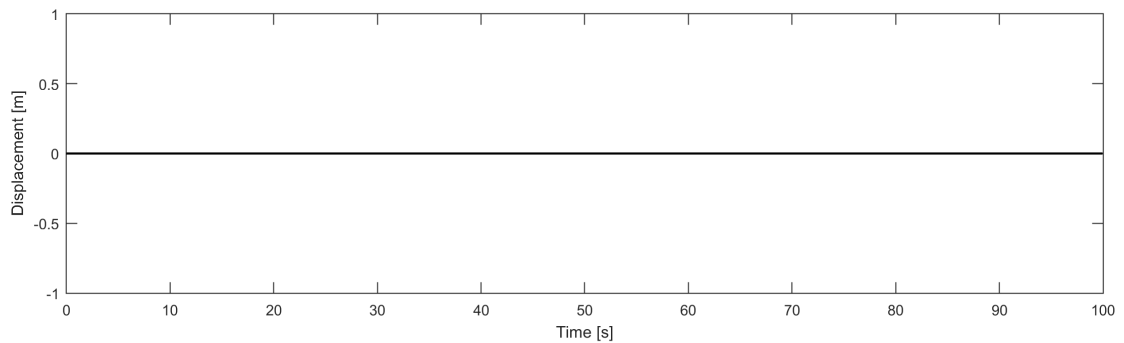


Figure 8.22: Displacement of the RNA in the XZ plane (Side-Side motion), for the cases with an incoming angle of  $0^\circ$ .

## 8.4. Ice load

Various ice sheet velocities were tested, results are shown in this section for velocities where the intermittent crushing and continuous brittle crushing regime were identified. The structure is in the intermittent crushing regime for a  $v_{ice}=0.005\text{m/s}$ , results for the Fore-Aft and Side-Side motion are shown in Figures 8.23 and 8.24.

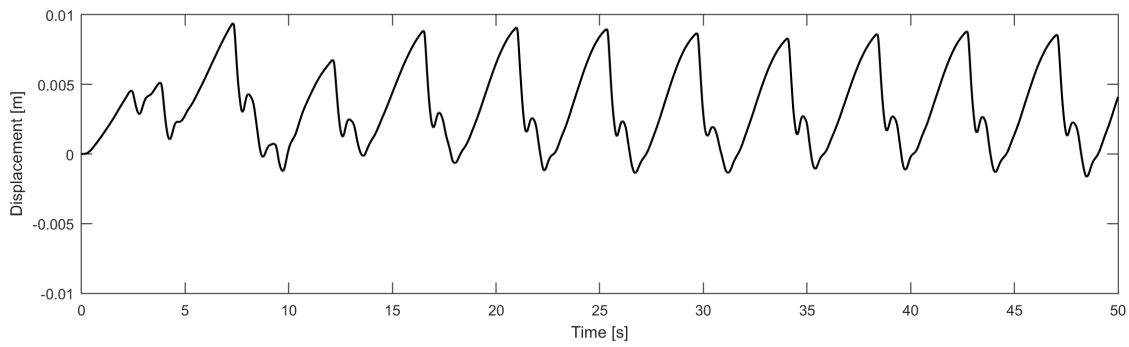


Figure 8.23: Displacement at the ice action point in the YZ plane (Fore-Aft motion), for an indentation velocity of  $v_{ice}=0.005m/s$  and thickness  $h_{ice}=0.4m$ .

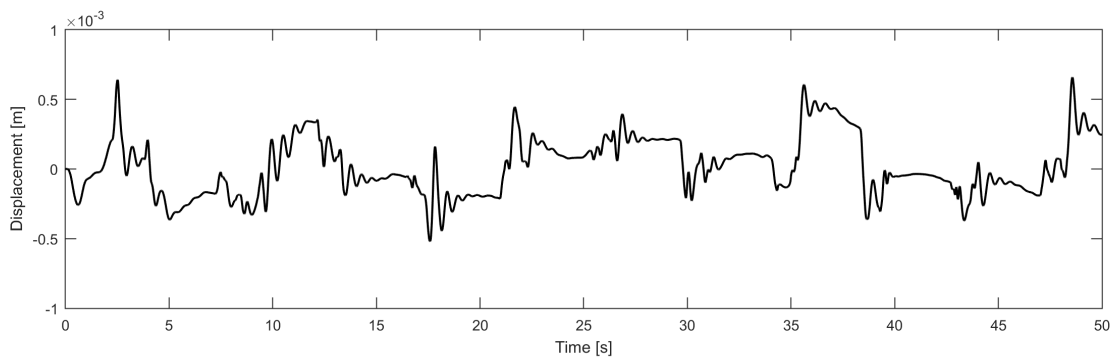


Figure 8.24: Displacement at the ice action point in the XZ plane (Side-Side motion), for an indentation velocity of  $v_{ice}=0.005m/s$  and thickness  $h_{ice}=0.4m$ .

The period of the intermittent crushing is about 5s and it is indeed larger than the longest natural period of the structure which is about 4s, but not much larger as stated in ISO [45]. Peaks appear near the first two natural frequencies of the structure in the Fore-Aft motion and near the first in the Side-Side motion in the spectra (Figures 8.25 and 8.26). The first bending mode is dominating the response of the structure.

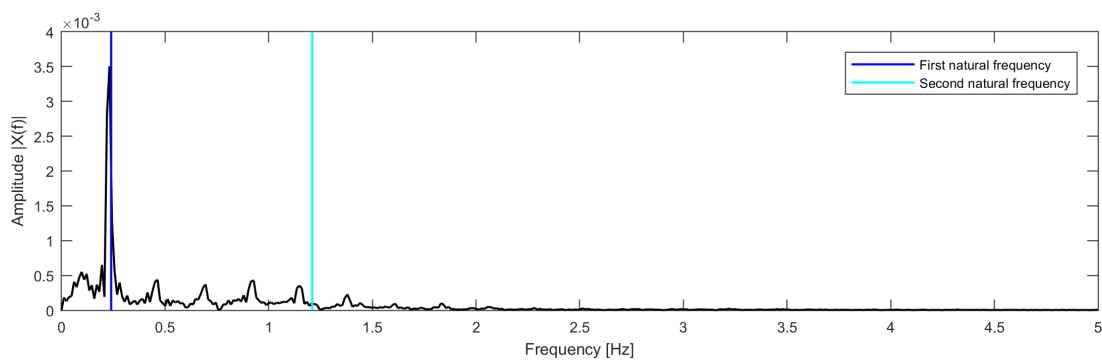


Figure 8.25: Single sided amplitude spectrum of the response for the same conditions as in Figure 8.23.

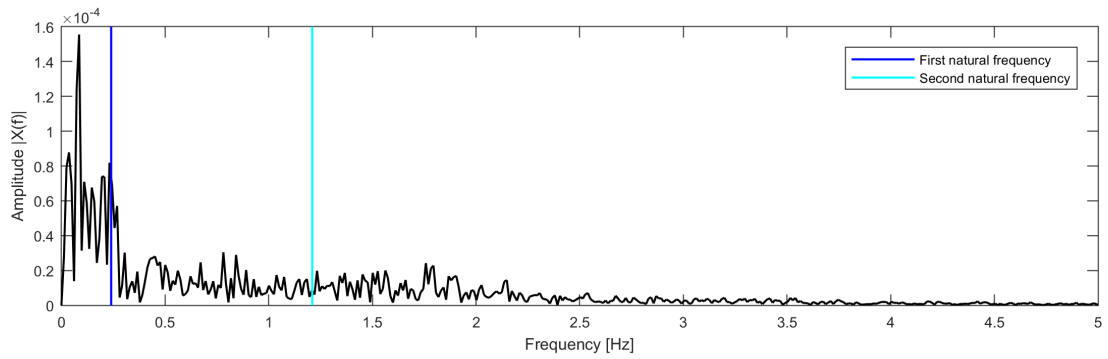


Figure 8.26: Single sided amplitude spectrum of the response for the same conditions as in Figure 8.24.

For an indentation velocity of  $v_{ice}=0.15m/s$ , no pattern is observed and the ice is in the continuous brittle crushing regime. The Fore-Aft motion (Figure 8.27) is again more intense than the Side-Side (Figure 8.28) due to the direction of the incoming ice sheet. The amplitude of the vibrations is very small compared to the one in the intermittent crushing regime in both planes.

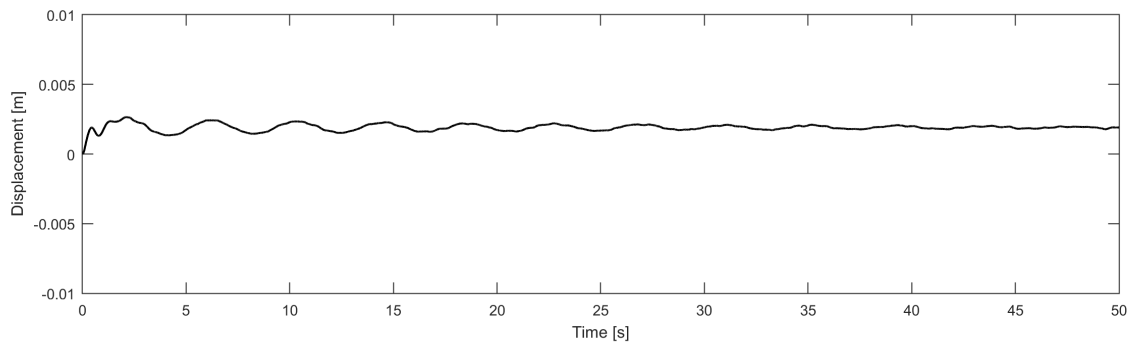


Figure 8.27: Displacement at the ice action point in the YZ plane (Fore-Aft motion), for an indentation velocity of  $v_{ice}=0.15m/s$  and thickness  $h_{ice}=0.4m$ .

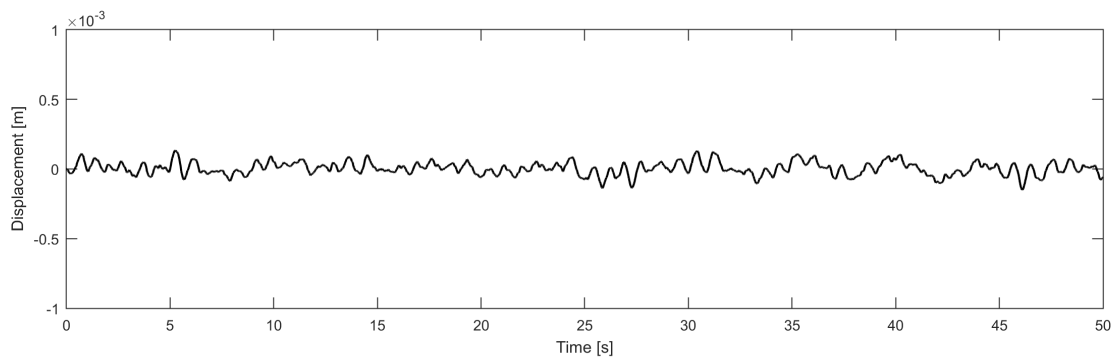


Figure 8.28: Displacement at the ice action point in the XZ plane (Side-Side motion), for an indentation velocity of  $v_{ice}=0.15m/s$  and thickness  $h_{ice}=0.4m$ .

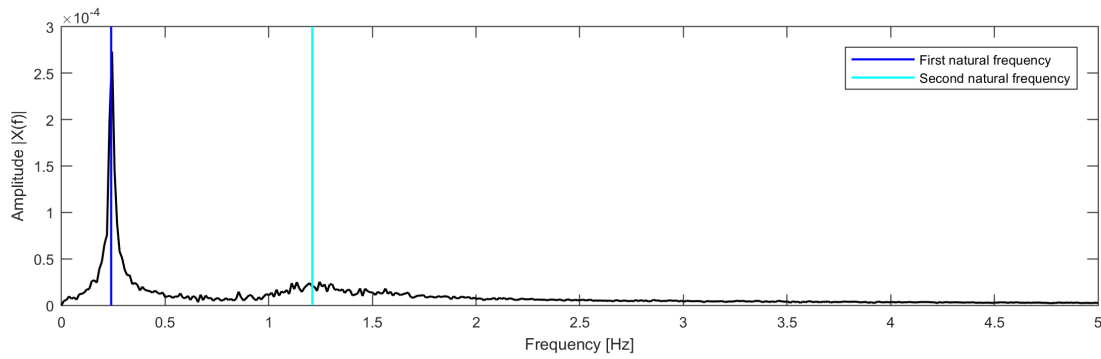


Figure 8.29: Single sided amplitude spectrum of the response for the same conditions as in Figure 8.28.

The amplitude spectra (Figures 8.29 and 8.30) present peaks near the first two natural frequencies of the structure in the Fore-Aft motion and near the first natural frequency in the Side-Side motion. The first bending mode is dominating the response in this case as well.

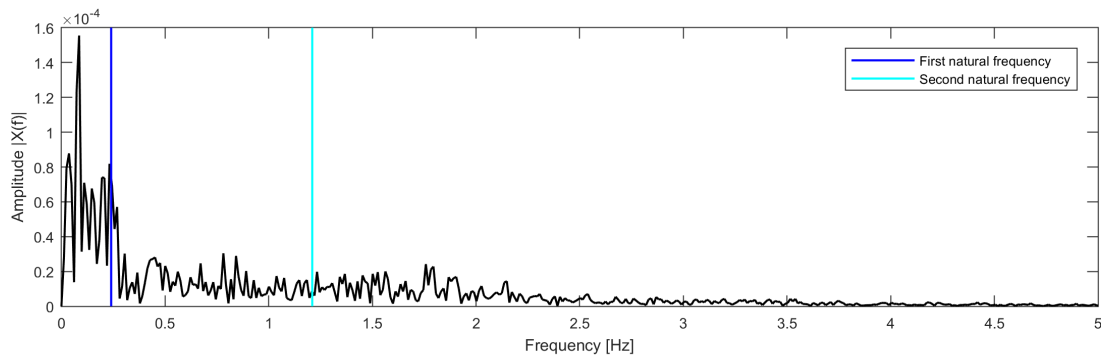


Figure 8.30: Single sided amplitude spectrum of the response for the same conditions as in Figure 8.28.

## 8.5. Aerodynamic and hydrodynamic load

### 8.5.1. Aligned

The hydrodynamic action is combined with the aerodynamic action in this section. For the case of a wave height  $H_S=0.5m$  with a period  $T_p=15.96s$  combined with the turbulent wind signal, the response is dominated by the wind load, the hydrodynamic load is very small and has no or very little influence on the response.

This is the result regardless of the equation that is used to predict the hydrodynamic action. The limitations of the linear theory for the given depth would allow for a maximum wave height of about  $H_S=0.80m$  with a period of  $T_p=36s$ , this is not expected to alter the response significantly in the combined case.

As the response is found to be identical with the one in Section 8.2 frequency plots are omitted. The Fore-Aft motion is shown in Figures 8.31, 8.33, 8.35 and 8.37. The Side-Side in presented in Figures 8.32, 8.34, 8.36 and 8.38.

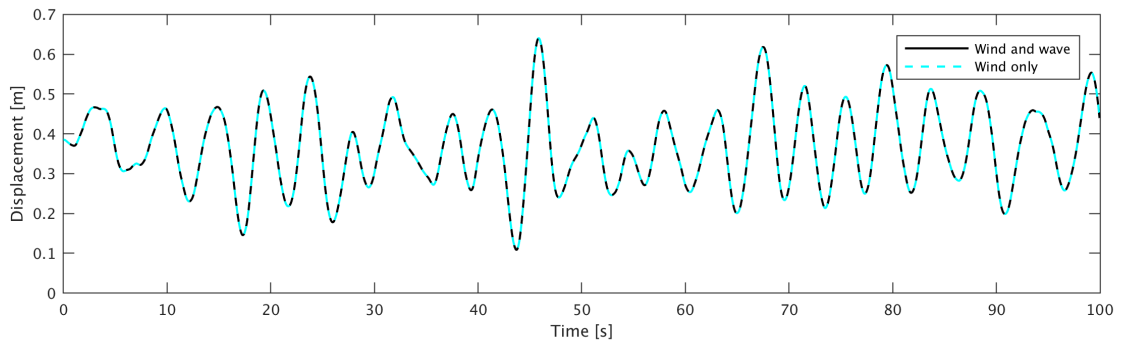


Figure 8.31: Displacement of the RNA in the YZ plane (Fore-Aft motion), resulting from the Airy theory and the Morison equation, for a wave height of  $H_S=0.5m$  and  $T_P=15.96s$ .

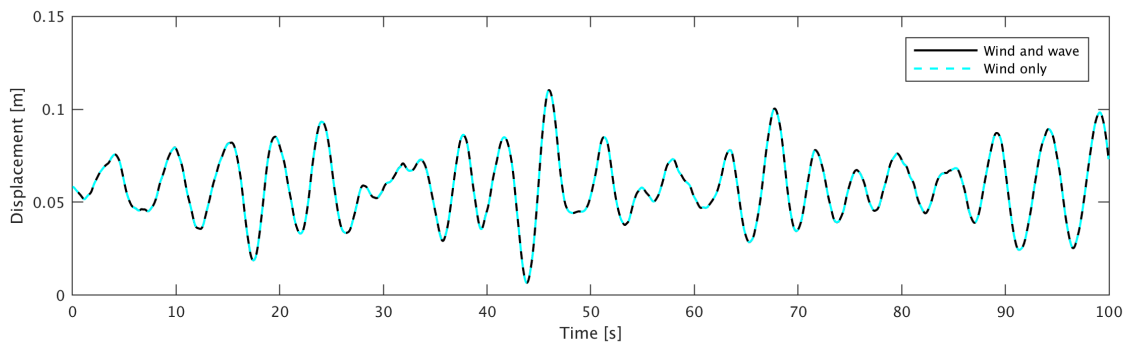


Figure 8.32: Displacement of the RNA in the XZ plane (Side-Side motion), resulting from the Airy theory and the Morison equation, for a wave height of  $H_S=0.5m$  and  $T_P=15.96s$ .

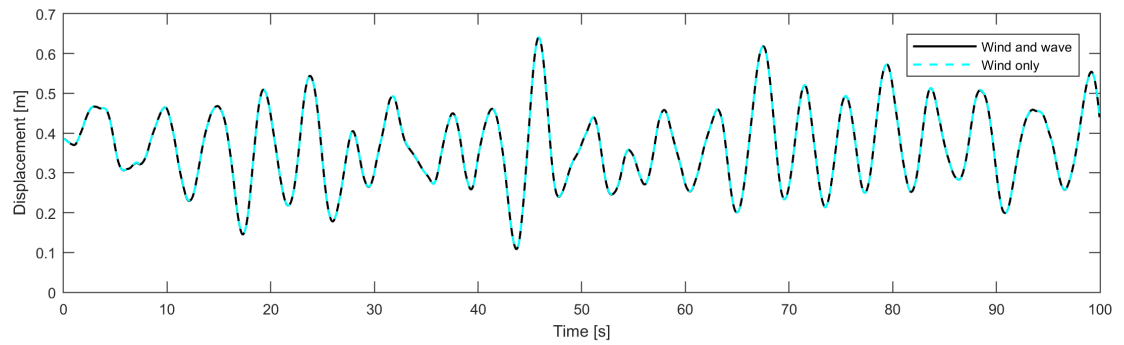


Figure 8.33: Displacement of the RNA in the YZ plane (Fore-Aft motion), resulting from the diffraction theory and the MacCamy and Fuchs equation, for a wave height of  $H_S=0.5m$  and  $T_P=15.96s$ .

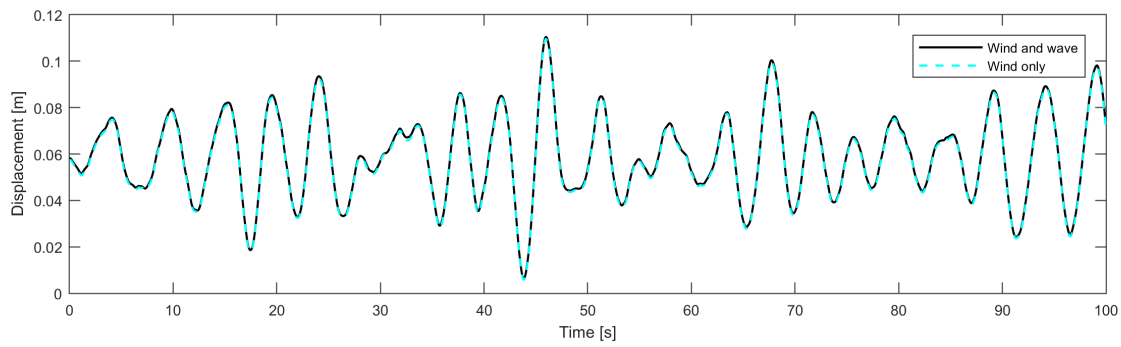


Figure 8.34: Displacement of the RNA in the XZ plane (Side-Side motion), resulting from the diffraction theory and the MacCamy and Fuchs equation, for a wave height of  $H_S=0.5m$  and  $T_P=15.96s$ .

The hydrodynamic action resulting from a wave with  $H_S=2.5m$  and  $T_P=22.58s$  using either the Morison or the MacCamy and Fuchs equation is also combined with the aerodynamic action. The results are presented in the following graphs.

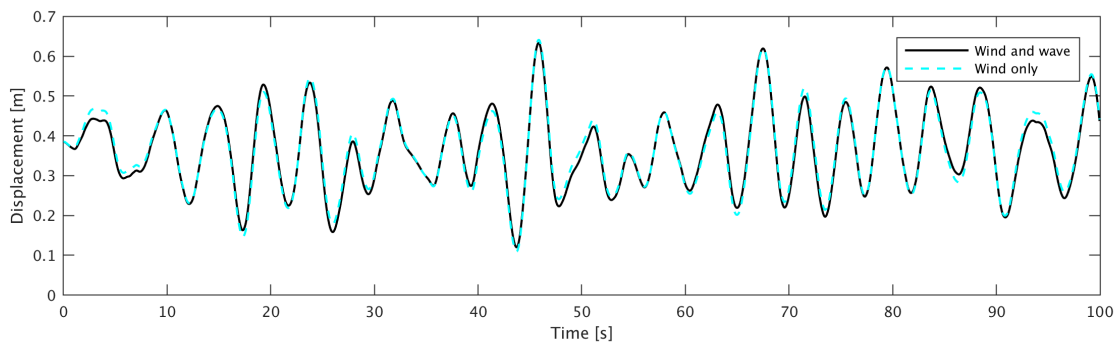


Figure 8.35: Displacement of the RNA in the YZ plane (Fore-Aft motion), resulting from the Airy theory and the Morison equation, for a wave height of  $H_S=2.5m$  and  $T_P=22.58s$ .

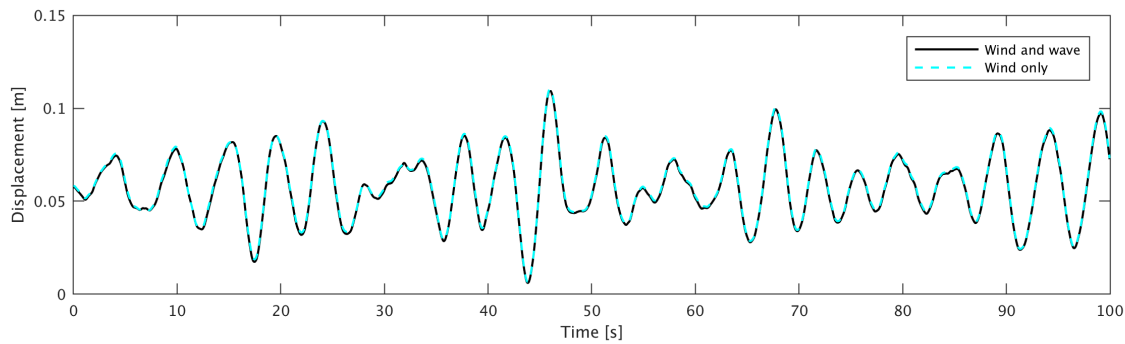


Figure 8.36: Displacement of the RNA in the XZ plane (Side-Side motion), resulting from the Airy theory and the Morison equation, for a wave height of  $H_S=2.5m$  and  $T_P=22.58s$ .

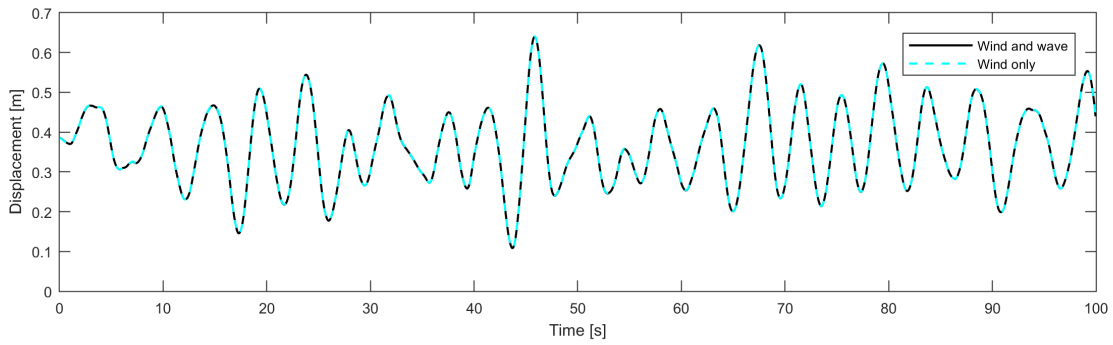


Figure 8.37: Displacement of the RNA in the YZ plane (Fore-Aft motion), resulting from the diffraction theory and the MacCamy and Fuchs equation, for a wave height of  $H_S=2.5m$  and  $T_P=22.58s$ .

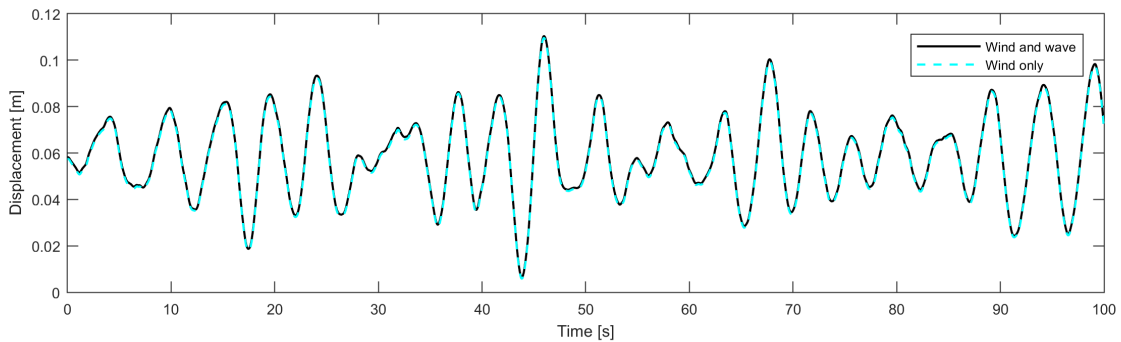


Figure 8.38: Displacement of the RNA in the XZ plane (Side-Side motion), resulting from the diffraction theory and the MacCamy and Fuchs equation, for a wave height of  $H_S=2.5m$  and  $T_P=22.58s$ .

In this case the wind load appears to be dominating the response as well. The response due to the combined loads in the YZ plane is slightly decreased when using the Morison equation, because the displacement only for the wave action is towards the negative while for the wind load towards the positive side as indicated in Sections 8.2 and 8.3, when using the MacCamy equation, water particle kinematics are not calculated in the same manner therefore this decrease is no longer present.

As there is alignment of the loads, there is no significant difference in the response in the XZ plane, a small difference not visible in the plots is present due to the difference in the response in the other plane when using the Morison equation. For the same reasons, frequency plots are omitted.

### 8.5.2. Misaligned

The same cases are examined considering a misalignment of the applied loads. An angle of attack of  $30^\circ$ , is considered for the incoming wave. The resulting hydrodynamic force is analyzed into XZ and YZ components. The Fore-Aft motion is shown in Figures 8.39, 8.41, 8.43 and 8.47 while in the Side-Side motion in Figures 8.40, 8.42, 8.44 and 8.48.

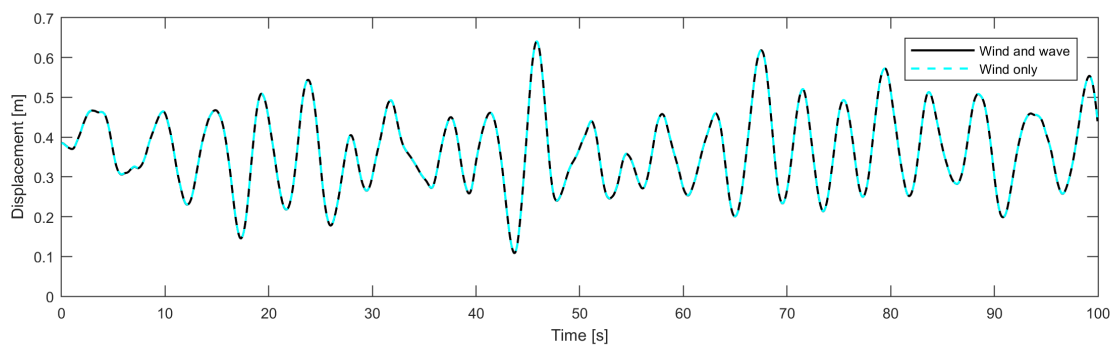


Figure 8.39: Displacement of the RNA in the YZ plane (Fore-Aft motion), resulting from the Airy theory and the Morison equation, for a wave height of  $H_S=0.5m$  and  $T_p=15.96s$  and a  $30^\circ$  angle of attack.

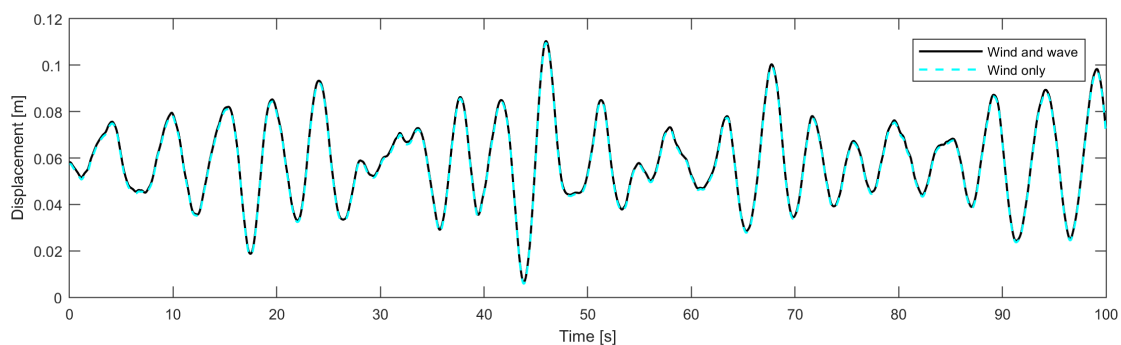


Figure 8.40: Displacement of the RNA in the XZ plane (Side-Side motion), resulting from the Airy theory and the Morison equation, for a wave height of  $H_S=0.5m$  and  $T_p=15.96s$  and a  $30^\circ$  angle of attack.

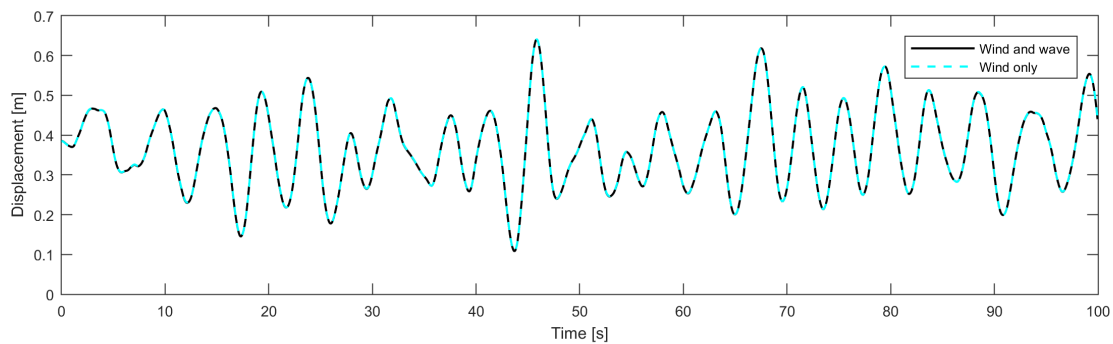


Figure 8.41: Displacement of the RNA in the YZ plane (Fore-Aft motion), resulting from the diffraction theory and the MacCamy and Fuchs equation, for a wave height of  $H_S=0.5m$  and  $T_p=15.96s$  and a  $30^\circ$  angle of attack.

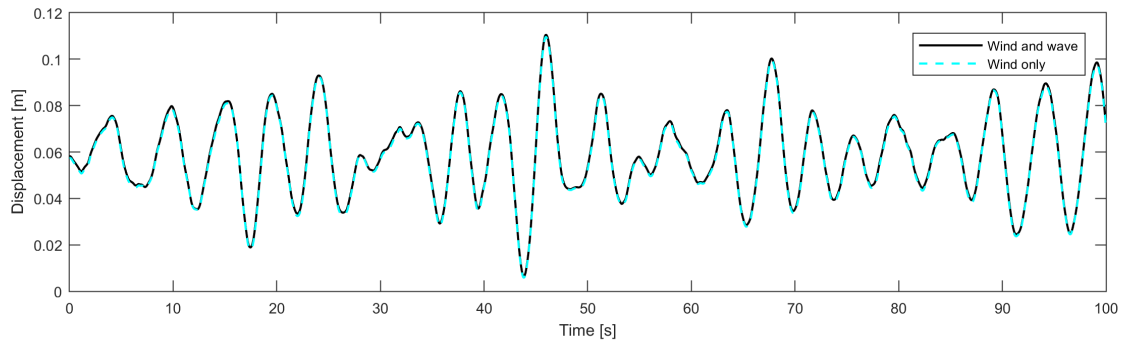


Figure 8.42: Displacement of the RNA in the XZ plane (Side-Side motion), resulting from the diffraction theory and the MacCamy and Fuchs equation, for a wave height of  $H_S=0.5m$  and  $T_P=15.96s$  and a  $30^\circ$  angle of attack.

The response remains unchanged compared to the aligned one. Since no contribution of the hydrodynamic load was present in the aligned case it is logical that also in the misaligned the response will be dominated by the wind load. Frequency plots are omitted.

The wave with  $H_S=2.5m$  and  $T_P=22.58s$  allows for a calculation of the water particle kinematics using the Stokes theory. When the response is calculated with the Morison equation and the Stokes theory, the response is altered from the wind only case however the result is odd.

Since the response in the parallel case did not differ much it is not expected that it will be here, since the hydrodynamic force is split between the two directions. This however is not the outcome of the analysis as it is shown in Figures 8.43 and 8.44. Accompanying amplitude spectra are shown in Figures 8.45 and 8.46. It must be stated however that this is considered a wrong result.

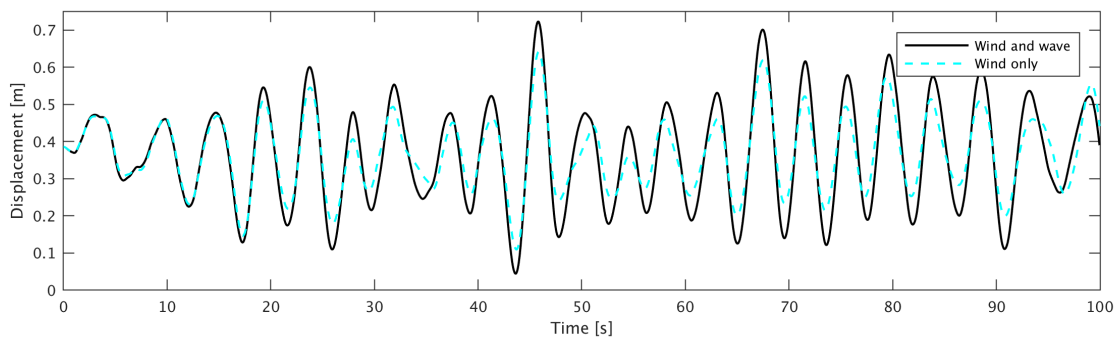


Figure 8.43: Displacement of the RNA in the YZ plane (Fore-Aft motion), resulting from the Stokes theory and the Morison equation, for a wave height of  $H_S=2.5m$  and  $T_P=22.58s$  and a  $30^\circ$  angle of attack.

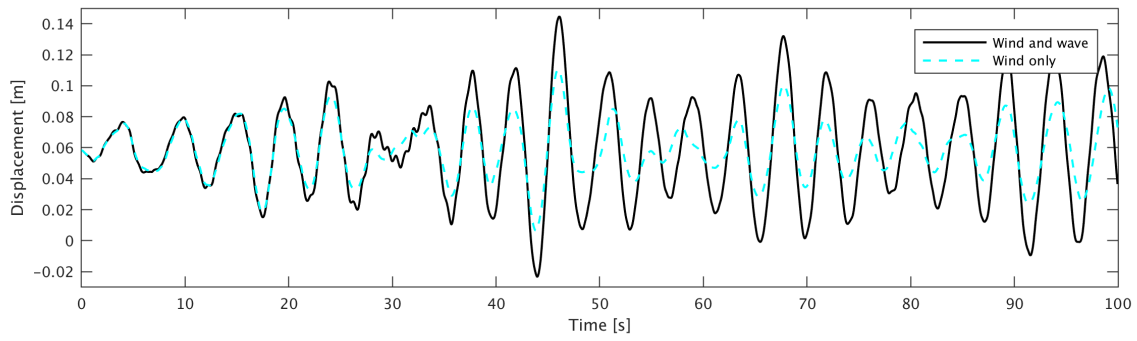


Figure 8.44: Displacement of the RNA in the XZ plane (Side-Side motion), resulting from the Stokes theory and the Morison equation, for a wave height of  $H_S=2.5m$  and  $T_P=22.58s$  and a  $30^\circ$  angle of attack.

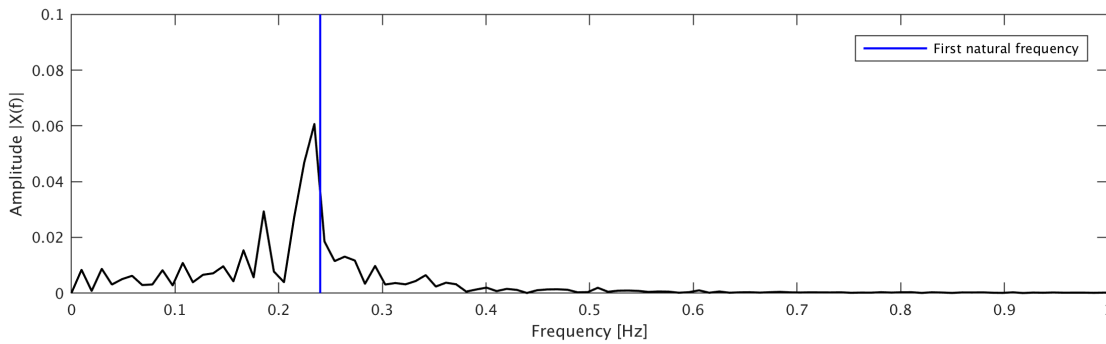


Figure 8.45: Single sided amplitude spectrum of the response of Figure 8.43.

The structure presents a strange behavior in this examined case, the displacement was expected to be less than that caused only by the wind load as in the parallel case the displacement between wind only and wave and wind did not differ significantly. The amplitude spectra of both motions show a peak at the first natural frequency.

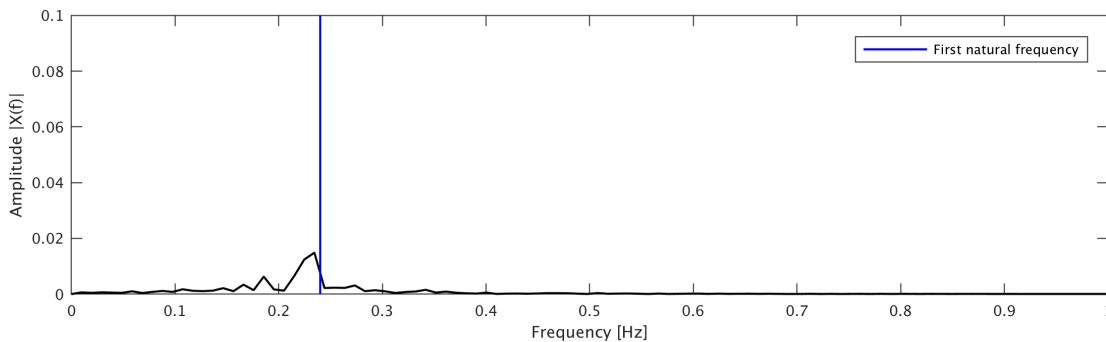


Figure 8.46: Single sided amplitude spectrum of the response of Figure 8.44.

When the force is calculated using the MacCamy and Fuchs equation the response is dom-

inated by the wind load and the response is identical to the previously calculated. For this reason frequency plots are omitted.

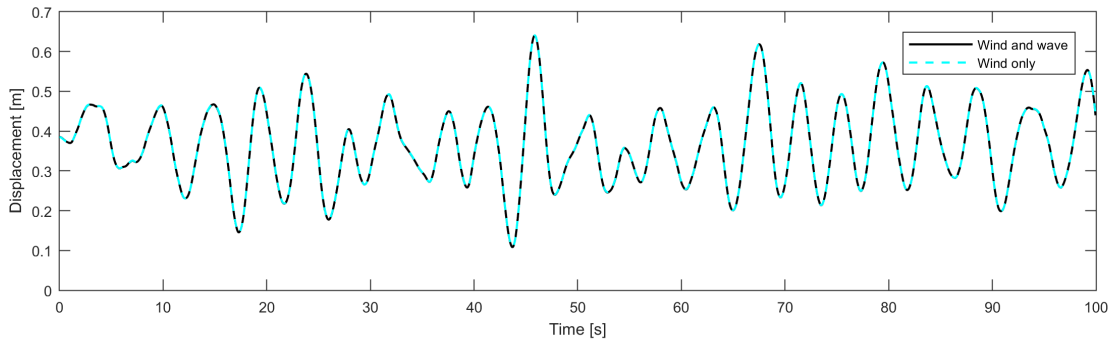


Figure 8.47: Displacement of the RNA in the YZ plane (Fore-Aft motion), resulting from the diffraction theory and the MacCamy and Fuchs equation, for a wave height of  $H_S=2.5m$  and  $T_P=22.58s$  and a  $30^\circ$  angle of attack.

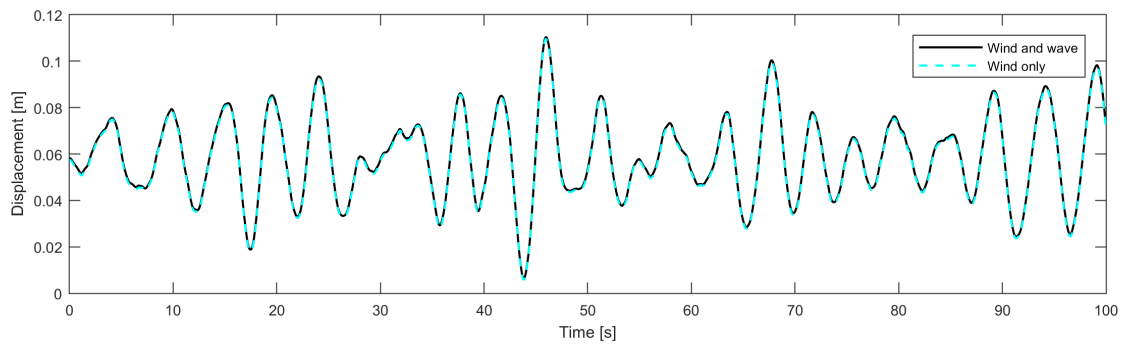


Figure 8.48: Displacement of the RNA in the XZ plane (Side-Side motion), resulting from the diffraction theory and the MacCamy and Fuchs equation, for a wave height of  $H_S=2.5m$  and  $T_P=22.58s$  and a  $30^\circ$  angle of attack.

## 8.6. Aerodynamic and ice load

### 8.6.1. Aligned

When considering only ice action, for the velocity of  $v_{ice}=0.005m/s$  the intermittent crushing regime was present. The same indentation velocity is now combined with the turbulent wind signal. The response is affected by both loads, the Fore-Aft motion is shown in Figure 8.57 and the Side-Side in Figure 8.58. The resulting response is shifted towards the positive side for the Fore-Aft motion, as a result of the force from the ice sheet. The ice load is depending on the relative velocity between the ice sheet and the structure, the aerodynamic load causes a significant displacement of the structure, in the combined analysis this is causing a higher ice load to be exerted when the relative velocity term is higher. This is a behavior that is also present in [53]. Although the saw-tooth pattern is no longer visible, peaks appear because of this combined action, this is clear in the peak near 35s.

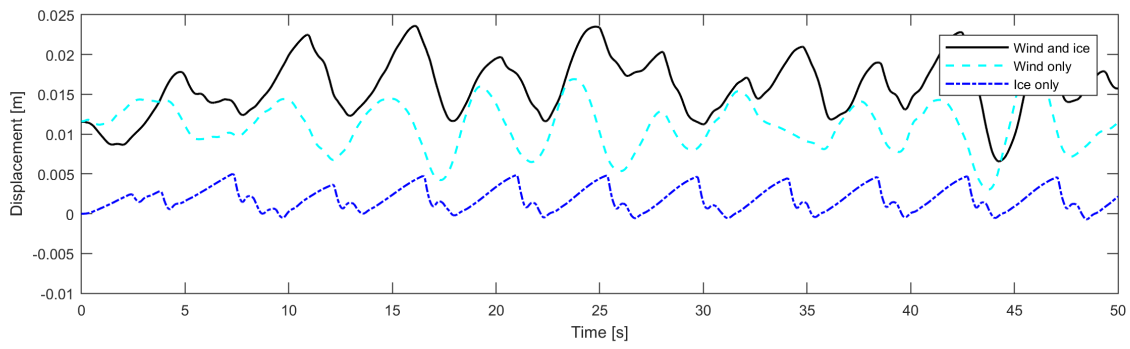


Figure 8.49: Displacement at the ice action point in the YZ plane (Fore-Aft motion), for an indentation velocity of  $v_{ice}=0.005m/s$ .

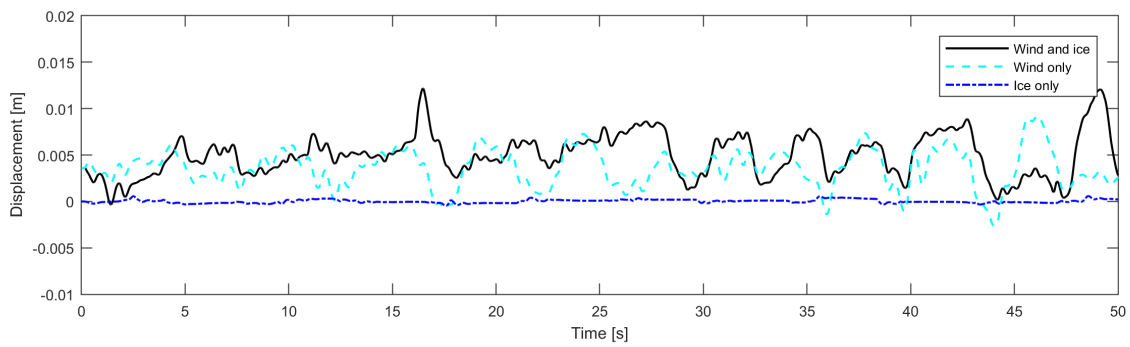


Figure 8.50: Displacement at the ice action point in the XZ plane (Side-Side motion), for an indentation velocity of  $v_{ice}=0.005m/s$ .

The amplitude spectra (Figures 8.59 and 8.60) show a peak near the first natural frequency of the structure indicating that the first bending mode is dominating the response.

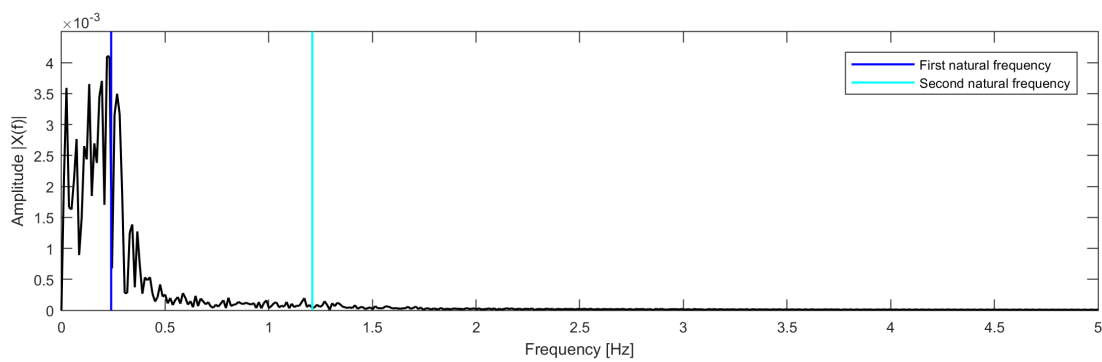


Figure 8.51: Single sided amplitude spectrum of the response of Figure 8.57.

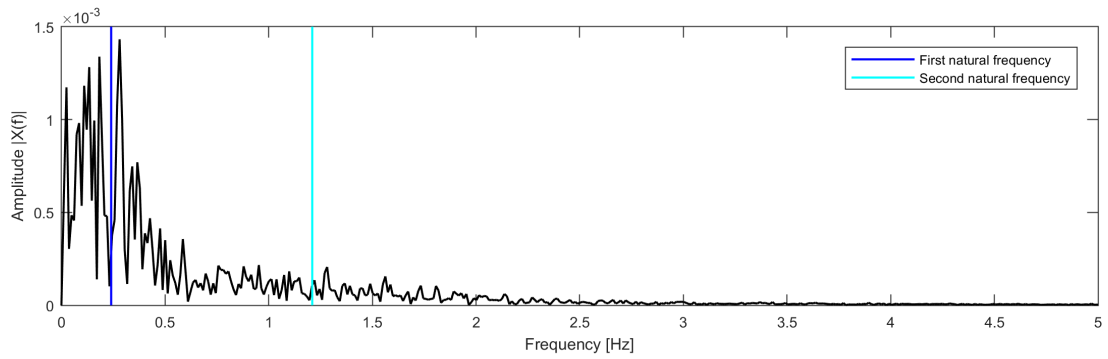


Figure 8.52: Single sided amplitude spectrum of the response of Figure 8.58.

With an indentation velocity of  $v_{ice}=0.15m/s$  the ice induced vibrations are in the random crushing regime. Although vibrations only from the ice action do not have a significant amplitude, the combined action of the loads is a lot different from the one considering only the aerodynamic load (Figures 8.53 and 8.54) due to the increase in the relative velocity.

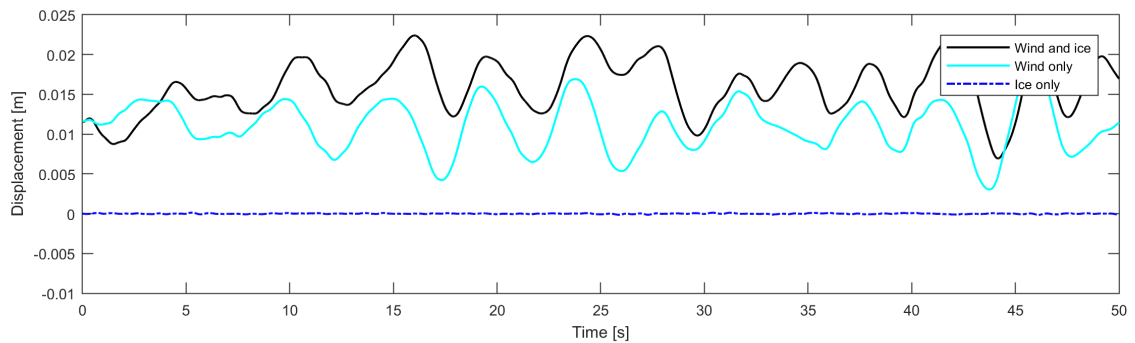


Figure 8.53: Displacement at the ice action point in the YZ plane (Fore-Aft motion), for an indentation velocity of  $v_{ice}=0.15m/s$ .

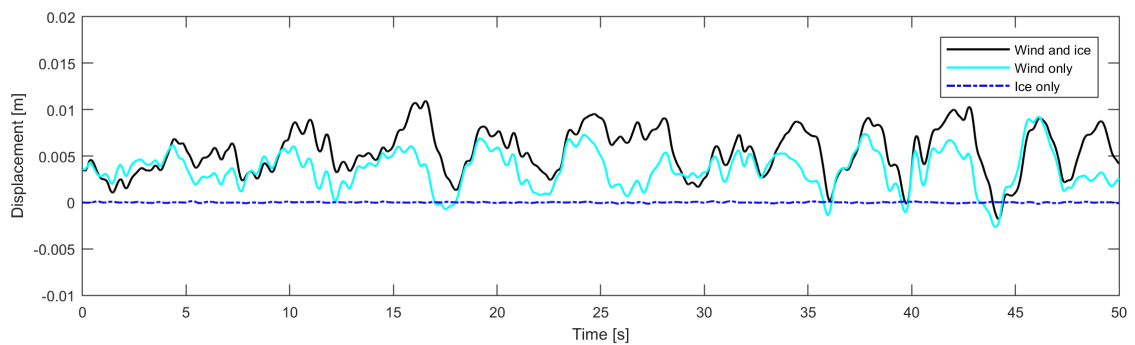


Figure 8.54: Displacement at the ice action point in the XZ plane (Side-Side motion), for an indentation velocity of  $v_{ice}=0.15m/s$ .

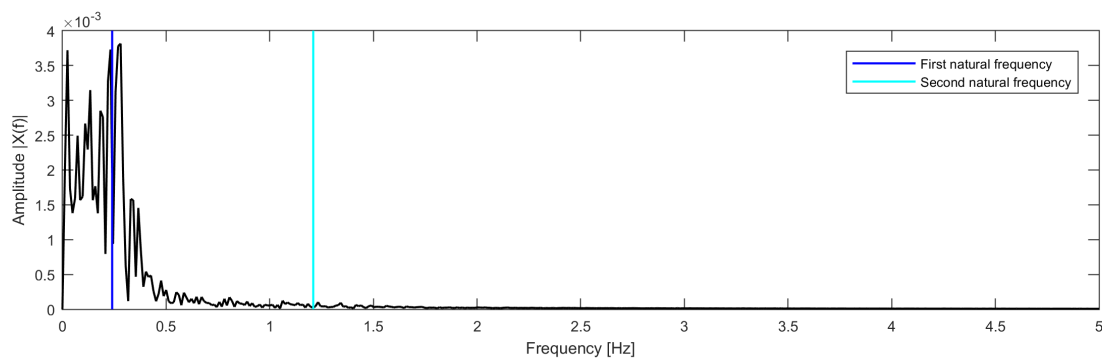


Figure 8.55: Single sided amplitude spectrum of the response of Figure 8.53.

In this case amplitude spectra (Figures 8.55 and 8.56) show a peak near the first natural frequency, with the first mode dominating the response.

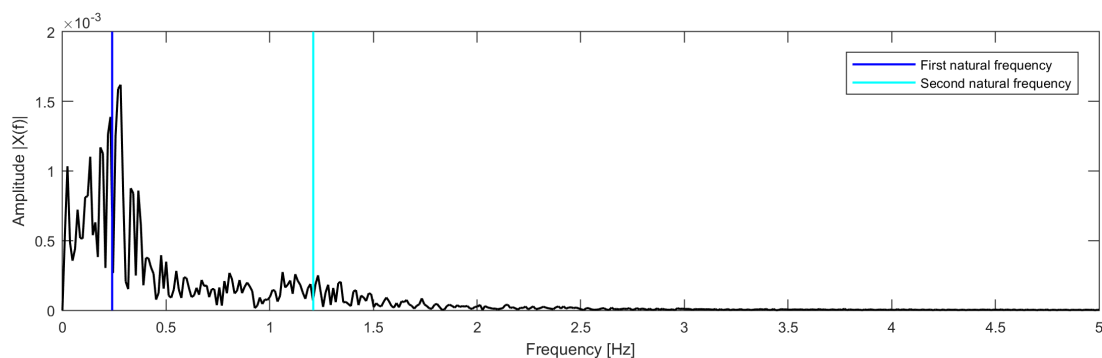


Figure 8.56: Single sided amplitude spectrum of the response of Figure 8.54.

### 8.6.2. Misaligned

The same cases are examined assuming a misalignment of  $30^\circ$ . The misalignment of the ice load causes a small decrease in most instances of the response in the Fore-Aft motion (Figure 8.58) compared to the parallel case, for an ice sheet velocity,  $v_{ice}=0.005m/s$ . This is a logical outcome as now the load that the ice exerts on the structure is distributed in two directions.

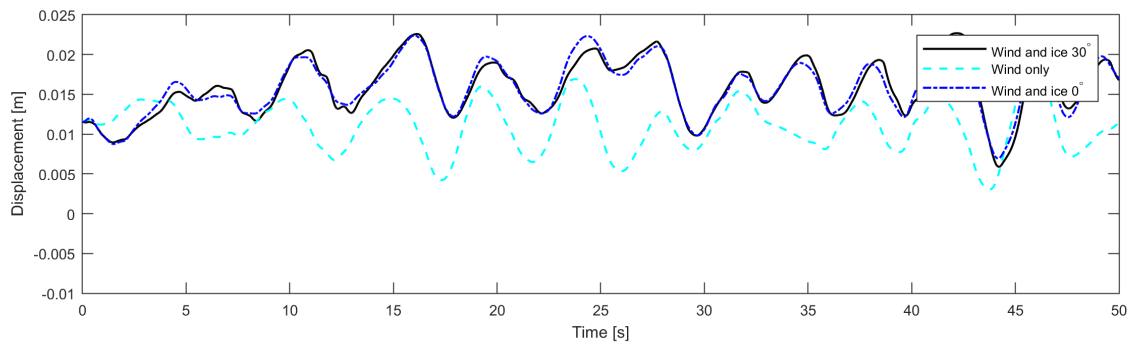


Figure 8.57: Displacement at the ice action point in the YZ plane (Fore-Aft motion), for an indentation velocity of  $v_{ice}=0.005m/s$ .

The same is observed in the Side-Side motion (Figure 8.58). Although the response does not appear to vary significantly between the aligned and misaligned cases.

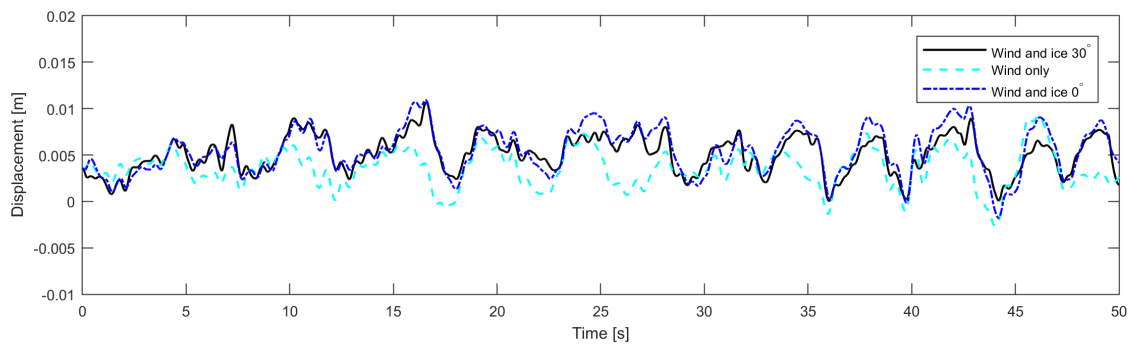


Figure 8.58: Displacement at the ice action point in the XZ plane (Side-Side motion), for an indentation velocity of  $v_{ice}=0.005m/s$ .

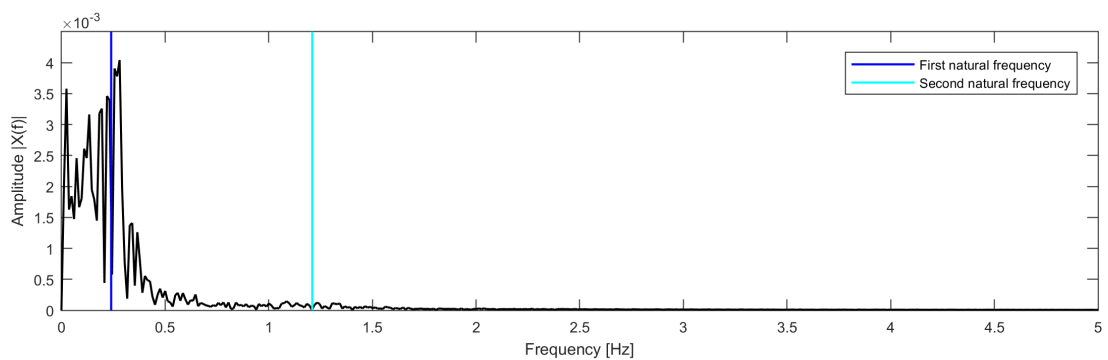


Figure 8.59: Single sided amplitude spectrum of the response of Figure 8.57.

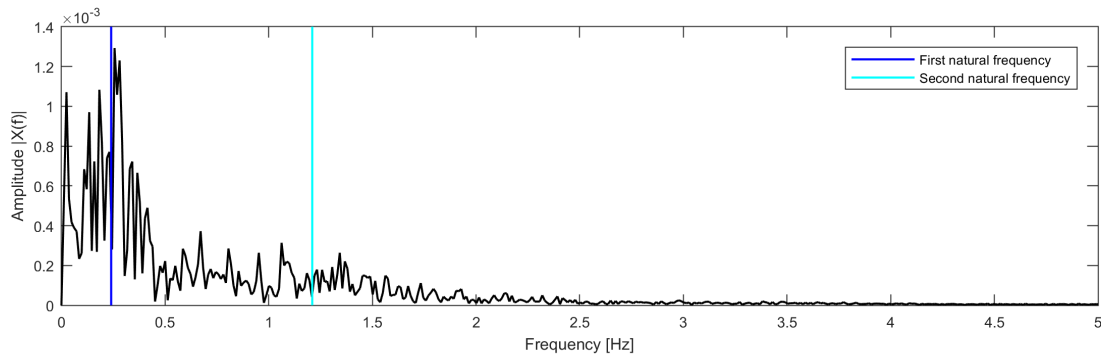


Figure 8.60: Single sided amplitude spectrum of the response of Figure 8.58.

Both spectra (Figures 8.59 and 8.60) show a peak near the first natural frequency of the structure. The results for an indentation velocity of  $v_{ice}=0.15m/s$  follow. The Fore-Aft and Side-Side motions are shown in Figures 8.61 and 8.62 respectively.

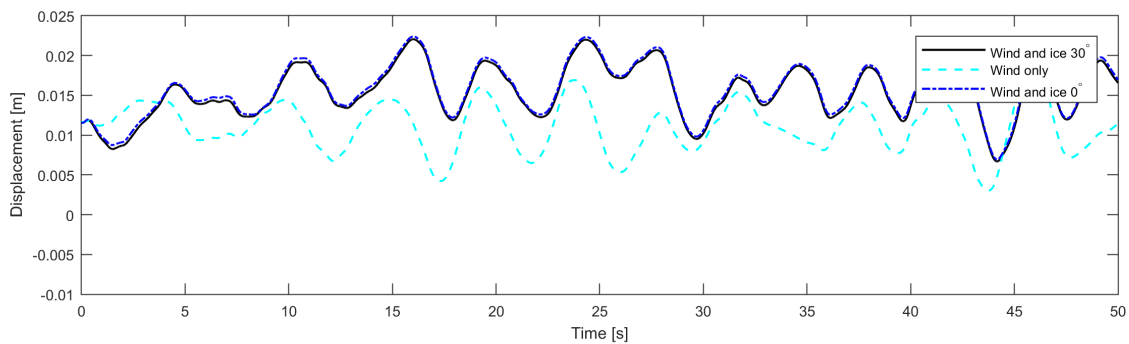


Figure 8.61: Displacement at the ice action point in the YZ plane (Fore-Aft motion), for an indentation velocity of  $v_{ice}=0.15m/s$ .

The resulting response does not change a lot between the aligned and misaligned case in both planes. However, a decrease in the Fore-Aft and increase in the Side-Side is visible due to the distribution of the load between the two directions.

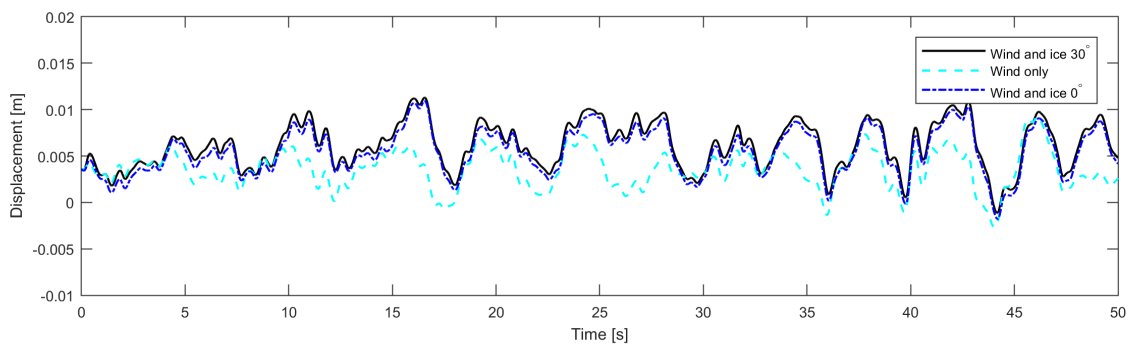


Figure 8.62: Displacement at the ice action point in the XZ plane (Side-Side motion), for an indentation velocity of  $v_{ice}=0.15m/s$ .

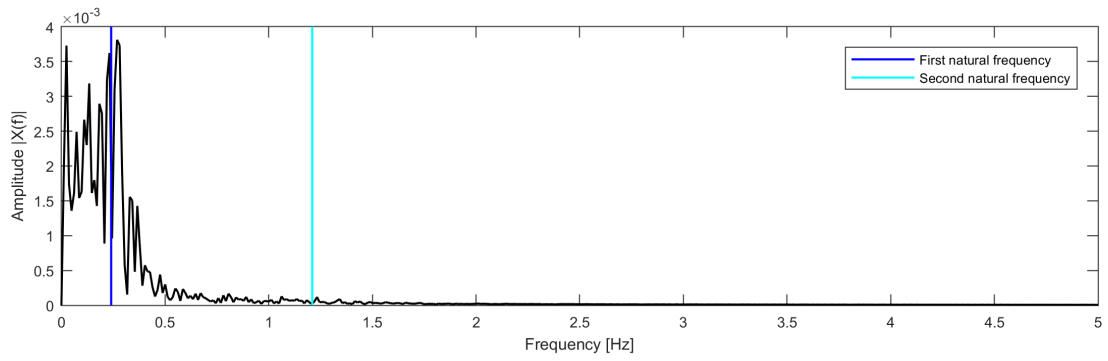


Figure 8.63: Single sided amplitude spectrum of the response of Figure 8.61.

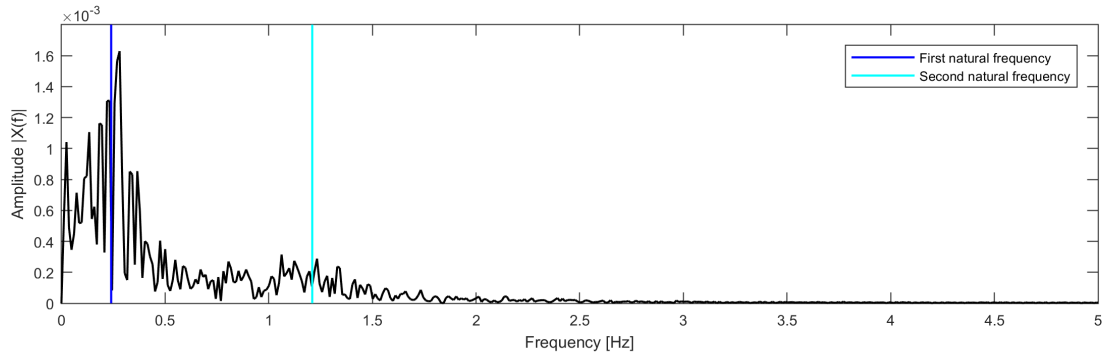


Figure 8.64: Single sided amplitude spectrum of the response of Figure 8.62.

The amplitude spectra (Figures 8.63 and 8.64) show a peak near the first natural frequency of the structure indicating that the first mode is dominating the response.

# Conclusion and recommendations

## 9.1. Concluding remarks

In the present thesis a 3D finite element model in MATLAB was created that provides as an output the response of the NREL-5MW offshore wind turbine under various loading combinations. The model is a result of the combination of already developed models from TU Delft and extensions applied to them. It can be easily adjusted to analyze a different wind turbine by providing basic dimensions. The model can be particularly useful in the case of the preliminary design of an offshore wind turbine. This study aimed to integrate different models to create one that can simulate the response of an offshore wind turbine under various types of loading. In order to proceed in the creation of the model, certain assumptions and simplifications had to be made. These assumptions are considered valid and logical. As with every assumption, however, there is a toll on the accuracy. In order to have a model that can surely produce results that can be trusted for a design, additional research is suggested. The loading combinations that can be generated with this model are the following:

- Aerodynamic load only
- Hydrodynamic load only, wave parameters are user defined and kinematics are calculated with Airy or Stokes 2<sup>nd</sup> order theory
- Ice load only
- Aerodynamic in combination with hydrodynamic load, the angle between the loads is user defined
- Aerodynamic and ice load, the angle between the loads is user defined

The model also comes with limitations, the signal that is given to the model must be above rated wind speed and reference values for the ice load must be known to proceed to the analysis.

The produced results are an outcome of analyses with high modal damping ratios (see Appendix A), for this reason, frequency lock-in could not be identified. The analyses for the ice-structure interaction were rerun for smaller damping ratios for velocities ranging from 0.006m/s (right after intermittent crushing) to 0.15m/s with a step of 0.01 however, frequency lock-in was not found in that range as well, modal damping must be further reduced for the structure to be in the frequency lock-in regime. The hydrodynamic loading results indicate very small contributions on the combined analyses, of course more analyses must be performed within the allowable limits of each theory. The aerodynamic load appears to be dominating the response of the turbine.

The amplitude spectra indicate that the selected number of modes is more than enough to describe the behavior of the structure and modal reduction can be further applied, this is of course depending also on the applied load.

This finite element model produces reasonable results, however it is not yet validated. It should be used with caution. A validation of the model is required. This can be done with experiments that might be available in literature or with a finite element analysis software package.

## 9.2. Recommendations for further work

An offshore wind turbine is subjected to cyclic loading. This repetitive loading will cause a local damage in the structure, which is generally known as fatigue damage. A fatigue assessment is necessary to monitor how these loads affect the structure and its response over the lifetime. While the structure is designed to withstand the Ultimate Limit State (ULS), it might not be sufficient to withstand fatigue damage and be able to produce energy with the same efficiency.

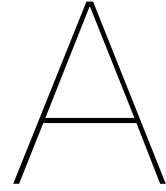
With respect to the hydrodynamic analysis, the assumption made to describe the velocity accounting for skewness and asymmetry needs to be further investigated regarding its validity, against software packages or experimental results.

The current practice to design an offshore wind support structure, often leads to an overdimensioning of the monopile. The main reason for this is the uncertainty regarding the soil. For this reason soil structure interaction needs to be carefully assessed, as cyclic loading might make the soil more loose or more dense. An additional issue regarding soil is the possible scouring around the monopile, and the scouring protection and how it affects the natural frequency. An alternative approach compared to Winkler foundation, could be the Pasternak foundation, in which the springs are not discrete but linked.

Regarding ice-structure interaction, the model currently used should be extended in order to simulate the ice sheet and its response around the whole circumference of the monopile, as it now covers half of it. Additionally, conditions must be added to check the distance of the ice elements with the monopile. In an extreme case where the lateral displacement of the monopile at the ice action node is large, the ice elements should be regenerated to surround the monopile otherwise they would remain in the displaced position and not exert any force on the structure.

The model that was used to predict the aerodynamic force comes with its limitations and assumptions. The blades are assumed to be rigid, as mentioned it is considered a valid assumption, an extension nevertheless would be to account for the flexibility of the blades and evaluate the impact of this effect. Additionally it is valid only for above rated wind speeds where pitch angle control is used. A wider range, including velocities from cut-in to cut-out will allow for a complete analysis in every operational condition of the turbine. An extension would also be the angle of attack, which in this case is low and allows for the assumption of no flow separation, as the low angle of attack assumption is not always valid [49].

It is highly recommended before taking any step towards the extension of this model, to validate it against experimental data.



# Appendix A: Modeling

## A.1. Parameters

In order to start building the finite element model in MATLAB, some necessary parameters need to be provided. The model is split into four parts, the tower, the transition piece above water, the transition piece below water and the monopile. The following dimensions need to be provided: the length, the outer diameter and the wall thickness of the tower at the top and at the bottom as the cross-section is tapered, the length the outer diameter and the wall thickness of the transition piece at the top and at the bottom, for both above and below mean water level, the length of the monopile and its wall thickness. Additionally the mass of the rotor and the nacelle has to be provided. The steel parameters that are required with the values that are used in this thesis are summarized below.

Property	Value
Density	$7850 \text{ kg/m}^3$
Poisson ratio	0.33[-]
Young's modulus	$210 \times 10^9 \text{ N/m}^2$
Shear modulus	$80 \times 10^9 \text{ N/m}^2$

Table A.1: Steel properties used for the finite element model.

The last requirement to build the model is the discretization parameters, the number of elements selected for each of the sections. Once these are defined the structural model can be built in MATLAB resulting in the necessary M, C, K matrices, the size of whom depends on the discretization that is selected. Each element has five degrees of freedom, two translational and three rotational. For  $n$  elements,  $n + 1$  nodes are created, in the way that the matrices are constructed the first  $2 \times (n + 1)$  degrees of freedom correspond to the side side motions in the XZ plane, the next  $2 \times (n + 1)$  degrees of freedom correspond to the fore aft motions in the YZ plane and the last  $n + 1$  correspond to yaw motions.

## A.2. Discretization

As the element size decreases the accuracy of the solution increases, however this has a toll on the computational time. As the element number increases the solution is expected to converge, meaning that the difference in the resulting response will decrease. As the load from the ice sheet and the maximum values of hydrodynamic load, as the water particle kinematics decrease with increasing depth, will both occur near the splash zone, the discretization in the transition piece is investigated. The optimal element number is a trade of between the accuracy of the solution and the computational time. Once the solution starts to converge the element number can be selected and considered sufficient. This effect is investigated for

a simple case, with just a hydrodynamic load resulting from a wave with the following characteristics:  $H_S=0.5m$  and  $T_p=15.96s$ . The choice of including only the hydrodynamic load is strictly to reduce the computational time. Four options are considered, with the element number of all but the transition piece remaining constant.

Discretization option	Tower elements	Above water transition piece elements	Below water transition piece elements	Monopile elements
1	15	2	2	15
2	15	3	3	15
3	15	4	4	15
4	15	5	5	15

Table A.2: Explanation of the examined discretization options.

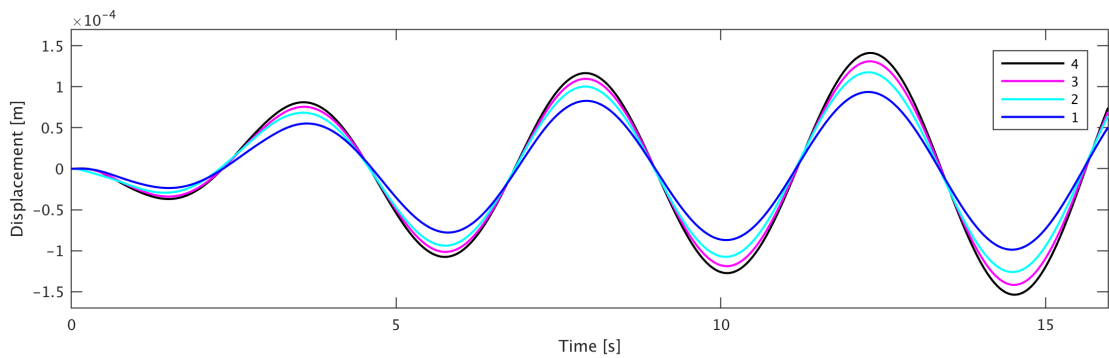


Figure A.1: Effect of discretization in the response of the RNA in the YZ plane.

It can be seen from the graph that with an increasing number of elements, the solution is converging. To support this statement, the mean difference between the consecutive discretization options was calculated.

Discretization	$\Delta x$
Between option 1 & 2	$1.1448 \times 10^{-5} m$
Between option 2 & 3	$6.3554 \times 10^{-6} m$
Between option 3 & 4	$4.6841 \times 10^{-6} m$

Table A.3: Convergence of the response of the RNA based on the discretization.

As expected, with increasing number of nodes the difference of the plots decreases, hence the solution is converging. The discretization option that is selected is option 4 resulting in total 40 elements in the structure.

### A.3. Varying surface elevation

As the surface of the water changes constantly with time, the length over which the force acts changes accordingly. This has an impact on force acting on the elements that are in every time instance located in the splash zone. For this reason the model was adjusted to account for this variation.

More specifically, the basic assumption is that the elevation of the transition piece is such that the waves only affect the transition piece and the monopile, an assumption which can

be considered valid as the design is based on providing sufficient clearance to assure this. Additionally, a wave profile stretching is needed to calculate the water particle kinematics above MSL, as mentioned in Section 4.3, Wheeler stretching is selected.

## A.4. Modal damping ratios

In Table A.4 the damping ratios that were used in the analyses, for the lowest modes are presented. Frequency lock-in in the case of ice-structure interaction is expected to be present in one of these modes. With these values frequency lock-in was not identified. In Table A.5 the ratios used in the reruns are presented. Lock-in was not identified using those either.

Mode number	XZ plane	YZ plane
1	2%	2%
2	5%	5%
3	11%	12%
4	22%	24%

Table A.4: Modal damping ratios for the lowest modes with  $\alpha_0=0.0048$  and  $\alpha_1=0.0841$ .

Mode number	XZ plane	YZ plane
1	0.5%	0.5%
2	1%	1%
3	3%	3%
4	5%	5%

Table A.5: Modal damping ratios for the lowest modes with  $\alpha_0=0.0012$  and  $\alpha_1=0.0207$ .



# Bibliography

- [1] Jonkman J. and Musial W. Offshore Code Comparison Collaboration (OC3) for IEA Task 23 Offshore Wind Technology and Deployment, journal = NREL, year = 2010,.
- [2] DNV-GL. Bladed engineering feature summary.
- [3] NREL. FAST, An aeroelastic computer-aided engineering (CAE) tool for horizontal axis wind turbines. <https://nwtc.nrel.gov/FAST>.
- [4] SIMPACK. Multi-Body Simulation Software. <http://www.simpack.com/mbs-software-product-wind.html>.
- [5] DTU Wind Energy. HAWC2. <http://www.hawc2.dk/HAWC2-info>.
- [6] McCoy T. Ice Load Project Final Technical Report. 2014.
- [7] Yu B. and Karr D. IceDyn Manual. 2015.
- [8] Jonkman J., Butterfield S., Musial W., and Scott G. Definition of a 5-MW reference wind turbine for offshore system deployment. *NREL*, 2009.
- [9] de Vries W. et al. Upwind WP4 D4.2.8 Final Report WP4.2: Support structure concepts for deep water. *TU Delft*, 2011.
- [10] The European offshore wind industry: Key trends and statistics 2016. <https://windeurope.org/wp-content/uploads/files/about-wind/statistics/WindEurope-Annual-Offshore-Statistics-2016.pdf>.
- [11] Regueiro R.A. and Duan Z. Static and Dynamic Micropolar Linear Elastic Beam Finite Element Formulation, Implementation, and Analysis. *Journal of Engineering Mechanics*, 2015.
- [12] Yokoyama T. *Parametric instability of Timoshenko beams resting on an elastic foundation*. 1988.
- [13] Chowdhury I. and Dasgupta S. P. Computation of Rayleigh damping coefficients for large systems. 2003.
- [14] Bazoune A., Khulief Y.A., and Stephen N.G. Shape functions of three-dimensional Timoshenko beam element. 2002.
- [15] Le Méhauté B. *An introduction to hydrodynamics and water waves*. Springer, Delft, 1976.
- [16] Holthuijsen L. H. *Waves in oceanic and coastal waters*. Cambridge University Press, Cambridge, 2007.
- [17] Chakrabarti S. K. *Hydrodynamics of offshore structures*. WIT Press, Southampton, 1987.
- [18] Ruessink B. G., Ramaekers G., and van Rijn L. C. On the parameterization of the free-stream non-linear wave orbital motion in nearshore morphodynamic models. *Coastal Engineering, Elsevier*, 2012.
- [19] Det Norske Veritas. Environmental conditions and environmental loads, DNV-RP-C205. 2007.
- [20] Garrison C. J., Seetharama Rao V., and Snider R. H. Wave interaction with large submerged objects. 1970.

- [21] Vugts J. H. *Handbook of Bottom Founded Offshore Structures, Part 1. General features of offshore structures and theoretical background*. Eburon Academic Publishers, Delft, 2013.
- [22] Morison J. R. and Johnson J. W. The force exerted by surface waves on piles. 1950.
- [23] Keulegan G. H. and Carpenter L. H. Forces on cylinders and plates in an oscillating fluid. 1958.
- [24] Thrasher L.W. and Aagaard P.M. Measured Wave Force Data on Offshore Platforms. *Offshore Technology Conference*, 1969.
- [25] Evans D.J. Analysis of wave force data. *Offshore Technology Conference*, 1969.
- [26] Dean R.G. and Aagaard P.M. Wave forces: data analysis and engineering calculation method. *Journal of Petroleum Technology*, 1970.
- [27] Kim Y.Y. and Hibbard H.C. Analysis of simultaneous wave force and water particle velocity measurements. *Offshore Technology Conference*, 1975.
- [28] Chakrabarti S., Wolbert A., and Tam W. Wave forces on a vertical cylinder. 1976.
- [29] Sarpkaya T. In-line and transverse forces on cylinders in oscillatory flow at high Reynolds numbers. *Offshore Technology Conference*, 1976.
- [30] Sarpkaya T. In-line and transverse forces on cylinders near a wall in oscillatory flow at high Reynolds numbers. *Offshore Technology Conference*, 1977.
- [31] Sarpkaya T. *Wave forces on offshore structures*. Cambridge University Press, Cambridge, 2010.
- [32] Spring B.H. and Monkmeier P.L. Interaction of plane waves with vertical cylinders. *Coastal Engineering Proceedings*, 1974.
- [33] Chakrabarti S.K. Comments on second-order wave effects on large diameter vertical cylinder. *Journal of Ship Research*, 1978.
- [34] Garrison C.J. Hydrodynamics of Large Objects in the Sea Part I Hydrodynamic Analysis. *Journal of Hydronautics*, 1974.
- [35] Garrison C.J. and Stacey R. Wave Loads on North Sea Gravity Platforms: A Comparison of Theory and Experiment. *Offshore Technology Conference*, 1977.
- [36] Raman H., Prabhakara Rao G.V., and Venkatanarasaiah P. Diffraction of non-linear surface waves by a circular cylinder. *Acta Mechanica*, 1975.
- [37] Yue D.K.P., Chen H.S., and Mei C.C. A hybrid element method for diffraction of water waves by three-dimensional bodies. *International Journal for Numerical Methods in Engineering*, 1975.
- [38] MacCamy R.C. and Fuchs R.A. Wave forces on piles: A diffraction theory. *Corps of Engineers*, 1954.
- [39] Wienke J., Sparboom U., and Oumeraci H. Theoretical formulae for wave slamming loads on slender circular cylinders and application for support structures of wind turbines. 2004.
- [40] Wienke J., Sparboom U., and Oumeraci H. Breaking wave impact force on a vertical and inclined slender pile-theoretical and large-scale model investigations. 2005.
- [41] INTERNATIONAL STANDARD. IEC 61400-3: Design requirements for offshore wind turbines. 2006.

- [42] Det Norske Veritas. Design of offshore wind turbine structures, DNV-OS-J101, year = 2014,.
- [43] Versteijlen W. G., Metrikine A. V., and van Dalen K. N. A method for identification of an effective Winkler foundation for large diameter offshore wind turbine support structures based on in-situ measured small-strain soil response and 3D modeling. 2016.
- [44] Corciulo S., Zanolì O., and Pisanò F. Supporting the engineering analysis of offshore wind turbines through advanced soil-structure 3D modeling. 2017.
- [45] International Organisation for Standardization. ISO/FDIS 19906: Petroleum and natural gas industries - Arctic offshore structures.
- [46] Løset S. Lecture notes in arctic offshore engineering, 2017.
- [47] Hendrikse H. *Ice induced vibrations of vertically-sided offshore structures*. PhD thesis, 2017.
- [48] van der Male P., van Dalen K. N., and Metrikine A. V. Definition of the coupling between the aerodynamic force on a wind turbine rotor and the tower top motions through force-response interaction matrices. 2017.
- [49] van den Bosch J. Definition and response validation of a simplified aero-servo-elastic wind turbine model, 2017.
- [50] Journée J. M. J. and Massie W. W. *Offshore Hydromechanics*. TU Delft, 2001.
- [51] Metrikine A.V. Lecture notes in structural dynamics, 2014.
- [52] Sehrawat N. Dynamic response of an Offshore wind turbine using linear (LIM) and non-linear (NLIM) environmental interaction models, 2016.
- [53] Shi W., Tan X., Gao Z., and Moan T. Numerical study of ice-induced loads and responses of a monopile-type offshore wind turbine in parked and operating conditions. 2015.

